Spatially-Dependent Multi-Wavelength Modelling of Pulsar Wind Nebulae

C van Rensburg

orcid.org 0002-7172-4028

Thesis accepted in fulfilment of the requirements for the degree *Doctor of Philosophy in Space Physics* at the North-West University

Promoter: Prof C Venter

Graduation May 2020

21106266

Declaration of Authorship

I, Carlo van Rensburg, declare that this thesis titled, 'Spatially-Dependent Multi-Wavelength Modelling of Pulsar Wind Nebulae' and the work presented in it are my own. I confirm that:

- This work was done wholly or mainly while in candidature for a research degree at this University.
- Where any part of this thesis has previously been submitted for a degree or any other qualification at this University or any other institution, this has been clearly stated.
- Where I have consulted the published work of others, this is always clearly attributed.
- Where I have quoted from the work of others, the source is always given. With the exception of such quotations, this thesis is entirely my own work.
- I have acknowledged all main sources of help.
- Where the thesis is based on work done by myself jointly with others, I have made clear exactly what was done by others and what I have contributed myself.

Signed: _____

Date: _____

"Even if there is only one possible unified theory, it is just a set of rules and equations. What is it that breathes fire into the equations and makes a universe for them to describe? The usual approach of science of constructing a mathematical model cannot answer the questions of why there should be a universe for the model to describe. Why does the universe go to all the bother of existing?"

Stephen Hawking, A Brief History of Time

NORTH-WEST UNIVERSITY

Abstract

Natural and Agricultural Sciences
Centre for Space Research

Doctor of Philosophy

Spatially-Dependent Multi-Wavelength Modelling of Pulsar Wind Nebulae

by Carlo van Rensburg

The next era of ground-based Cherenkov telescope development will see a great increase in both quantity and quality of γ-ray morphological data. This initiated the development of a spatio-temporal leptonic transport code to model pulsar wind nebulae. In this thesis I present the development and implementation of this code that predicts the evolution of the leptonic particle spectrum and radiation at different radii in a spherically-symmetric source. I show how the code is calibrated using the models of previous authors and then indicate how we simultaneously fit the overall broadband spectral energy distribution, the surface brightness profile and the X-ray photon index vs. radius for PWN 3C 58, PWN G21.5−0.9 and PWN G0.9+0.1. Such concurrent fitting of disparate data sets is non-trivial and we thus investigate the utility of different goodness-of-fit statistics, specifically the traditional χ^2 test statistic and a newly developed scaled-flux-normalised test statistic to obtain best-fit parameters. We find reasonable fits to the spatial and spectral data of all three sources, but note some remaining degeneracies that motivate further model development and will have to be broken by future observations.

Keywords: pulsars, pulsar wind nebulae, supernova remnants, gamma rays, non-thermal radiation mechanisms, neutron stars, X-rays, multi-wavelength astronomy, astroparticle physics, numerical methods.

Acknowledgements

The journey of acquiring this PhD has been a daunting yet fruitful experience. I would like to thank the following people for their support and understanding during this time:

- My supervisor, Prof. Christo Venter, for his friendship, expert academic guidance, patience and a great source of knowledge, I thank you.
- All my colleagues at the Centre for Space Research for the useful discussions, encouragement and friendliness.
- Mrs Petro Sieberhagen for always being ready to help with financial and administrative needs and always being my mother at the office.
- Elanie van Rooyen and Lee-Ann van Wyk for always being there in assisting me with administration and travel arrangements.
- The Centre for Space Research and the National Research Foundation for their financial support.
- My parents, Charles and Susan van Rensburg, for their financial and emotional support, guidance and willingness to never give up on me, I thank you from the bottom of my heart.
- Elizma Oosthuizen, my loving fiancee, thank you for your love and always being understanding and motivating.
- My friends and other family for always supporting me and keeping me motivated.
- Dr. Melvin Vergie for proof-reading my thesis.

Lastly, but not least, I would like to thank my Heavenly Father for being with me through this journey, carrying me when times were hard, and pushing me to heights that I have never dreamt I would reach.

Carlo van Rensburg
Centre for Space Research, North-West University
Potchefstroom Campus, Private Bag X6001
Potchefstroom, South Africa, 2520

Contents

List of Figures

List of Tables

Abbreviations

ACT	Atmospheric Cherenkov telescope
AMEGO	All-sky Medium Energy Gamma-ray Observatory
ASKAP	Australian Square Kilometre Array Pathfinder
BB	Black body
CMB	Cosmic Microwave Background
CSM	Circumstellar Material
CTA	Cherenkov Telescope Array
FGST	*Fermi* Gamma-Ray Space Telescope
FOV	Field of view
GBM	Gamma-ray Burst Monitor
GC	Galactic Centre
GLAST	Gamma-ray Large Area Space Telescope
GRB	Gamma-Ray Burst
HE	High Energy
H.E.S.S.	High-Energy Stereoscopic System
IC	Inverse Compton
IR	Infrared
ISM	Interstellar Medium
K-N	Klein-Nishina
LAT	Large Area Telescope
MAGIC	Major Atmospheric Gamma Imaging Cherenkov Telescope
MHD	Magnetohydrodynamic
MWA	Murchison Widefield Array
PMT	Photomultiplier Tubes
PSF	Point Spread Function

PWN	Pulsar Wind Nebula
RM	Rotation Measure
SA-GAMMA	South African Gamma-Ray Astronomy Programme
SB	Surface Brightness
SED	Spectral Energy Distribution
SKA	Square Kilometre Array
SN	Supernova
SNR	Supernova Remnant
SR	Synchrotron Radiation
SSC	Synchrotron Self-Compton
VERITAS	Very Energetic Radiation Imaging Telescope Array System
VHE	Very High Energy
VLA	Very Large Array
0D	zero-dimensional
1D	1-dimensional
2D	2-dimensional
3D	3-dimensional

Chapter 1

Introduction

Stars follow a life cycle similar to that of humans. They are born, reach adolescence, age and after some time their lives come to an end. Sufficiently large stars end their lives with one of the most energetic events in the Universe called a supernova (SN). These catastrophic events leave behind intriguing and beautiful objects that radiate energy across the entire electromagnetic spectrum from low-energy radio waves to the highest-energy gamma rays.

Figure 1.1 shows the most well-known supernova remnant containing the Crab Nebula[1]. This is a composite image combining observations from the Very Large Array (VLA) radio telescope, infrared observations from the *Spitzer* Space Telescope, visible light from the Hubble Space Telescope and high-energy images from the *Chandra* X-ray Observatory. In this image there are no Very High Energy (VHE, 10 GeV $\lesssim E \lesssim$ 300 TeV) gamma-ray counterpart, as the current gamma-ray telescopes do not have as good as an angular resolution as the other observatories.

We are entering one of the most exciting eras for VHE astronomy. The 2020s will see the development of the new Cherenkov Telescope Array (CTA) that will have sites in the northern (19 telescopes) and the southern (100 telescopes) hemispheres (Ong et al., 2019). This array of telescopes, with its order-of-magnitude increase in sensitivity and significant improvement in angular resolution over current ones, will discover several more (older and fainter) gamma-ray sources and reveal many more morphological details of currently known sources, e.g., SNe. One of the products of supernova explosions is pulsar wind nebulae (PWNe). Historically they have been defined based on their observational properties, having a centre-filled emission morphology, a flat spectrum at radio wavelengths, and a very broad spectrum of non-thermal emission ranging from the radio band all the way to high-energy gamma rays (Amato, 2014). Currently there are

[1] http://hubblesite.org/image/4027

FIGURE 1.1: Multiwavelength observations of the Crab Nebula. This image combines data from five different telescopes: the VLA (radio) in red; *Spitzer* Space Telescope (infrared) in yellow; Hubble Space Telescope (visible) in green; *XMM*-Newton (ultraviolet) in blue; and *Chandra* X-ray Observatory (X-ray) in purple.

224 known VHE gamma-ray sources, 35 of these being PWNe[2]. The *Fermi* Large Area Telescope (LAT) has detected 5 high-energy gamma-ray PWNe and 11 PWN candidates (Ferrara et al., 2015). The X-ray to VHE gamma-ray energy range boasts 85 PWNe or PWN candidates, 71 of which have associated pulsars (Kargaltsev et al., 2012).

In light of all these observational advances and prospects, we need similar advances in theoretical models to be able to interpret the empirical information in this era. The current modelling landscape can be divided into three main categories, each with its own advantages and shortcomings. The first of these are magneto-hydrodynamic (MHD) codes (e.g., Bucciantini, 2014, Slane, 2017, Olmi and Bucciantini, 2019) that are able to model the morphology of PWNe in great detail, but struggle to reproduce the radiation spectra. In contrast to MHD codes, spectral codes (mostly leptonic), see, e.g., Venter and de Jager (2007), Zhang et al. (2008), Gelfand et al. (2009), Tanaka and Takahara (2011), Martín et al. (2012) and Torres et al. (2014), are able to reproduce the radiation spectra in great detail but fail to model the morphology of these sources, as most of these codes model the particle spectrum within a single zone (0D). This leads us to the third type of model that is hybrid in nature, using a combination of MHD and leptonic

[2]http://tevcat2.uchicago.edu/

codes to predict both the morphology and radiation spectrum (e.g., Porth et al., 2016). Thus, there is a void in the current modelling landscape that has not been investigated substantially, which is modelling the leptonic particle spectrum as a function of position in 1D, 2D or 3D.

In addition to the observational advances and modelling uncertainties, Gelfand et al. (2015) list a few unsolved questions in this field. One such question is: What is the process responsible for converting the magnetically-dominated pulsar wind close to the embedded pulsar to a particle-dominated wind inside the PWN, i.e., how are particles accelerated in a PWN? Another unknown is the so-called positron excess. Experiments like *Fermi*-LAT, *PAMELA*, and *AMS-02* have observed an increase in the positron-electron flux ratio at energies above 10 GeV. In this regard, Hewitt and Lemoine-Goumard (2015) suggested that PWNe could be the source of this phenomenon. Gelfand (2017) adds to these questions by asking how the particles are created in the first place within the magnetospheres of neutron stars. These are but some of the questions surrounding PWNe, indicating that more research is needed in this field.

1.1 Research Goal

The main aim of this study is to develop a spatio-temporal leptonic transport emission code to model the transport and radiation of leptons in a PWN. Such a code equips us with the tools to make predictions for PWNe, not only their radiation spectra, but also allowing spatial predictions, for example surface brightness (SB) profiles and photon indices as a function of radius for some energy range. The development of new telescopes that are able to observe the morphologies of PWNe in more detail is discussed in Section 2.4. This is a primary motivation for us developing a spatio-temporal code. Figure 1.2 shows an example where the H.E.S.S. Collaboration performed a study on the Vela X PWN, measuring the photon index (left panel) as a function of radial distance from the pulsar position as well as an SB profile (right panel). These types of morphological data are becoming available in different energy bands, and can be seen in the right panel of Figure 1.2, which shows the radio and X-ray SBs as well. With a spatio-temporal code in hand, we will be well positioned to make the best use of such data.

A secondary motivation is provided by the fact that multi-dimensional combined MHD-emission codes require long computational time to run and in Section 4.1 the limitations of the different modelling strategies are mentioned. In our modelling we mitigate this problem by using a parametric approach to incorporate, e.g., the magnetic field and the

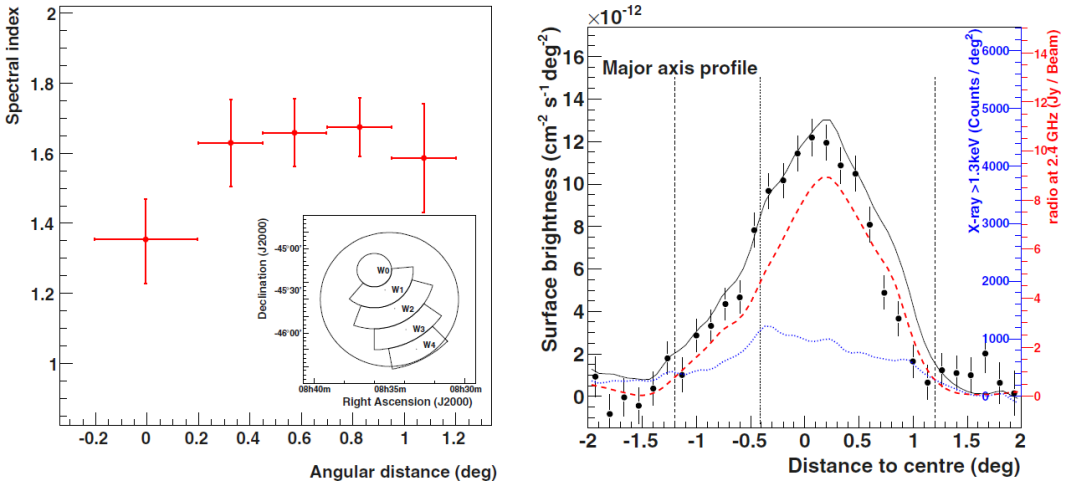

FIGURE 1.2: *Left*: The spectral index as a function of radial distance from the central pulsar position for Vela X in the H.E.S.S. energy range of 0.75 − 10.0 TeV. *Right*: SB profiles for Vela X along its major axis with the black dots indicating the VHE gamma-ray data (Abramowski et al., 2012b), the red dashed line indicating the 2.4 GHz radio surface brightness data (Duncan et al., 1995) and the blue dotted line showing the X-ray data for energies > 1.3 keV (Aschenbach, 1998) after the bright pulsar emission has been removed.

velocity profiles, from results found by MHD studies. This approach is computationally much cheaper.

This thesis relates the development and application of a spatially-dependent 1D code to model several sources in an attempt to break parameter degeneracies currently found in PWN modelling by fitting the code concurrently to various spectral and spatial data sets. This poses a new level of challenges, which we address by implementing a new type of test statistic, as the available data are heterogeneous in nature (data sets with a large difference in the number of data points, as well as a disparity in the relative magnitude of their errors). This, in conjunction with a thorough parameter study, is used to explore the parameter space to show how different parameters influence the spectral and spatial results. This model applies to young PWNe (with an age of a couple of thousand years or less) and thus suitable sources are modelled by choosing them based on their age and the availability of radial data. They are modelled by other authors and their model results are used as a comparison to our code's output.

1.2 Thesis Outline

This thesis follows the following structure:

- In **Chapter 2** the conceptual framework of this study is discussed by describing the evolutionary path that results in a PWN. This is achieved by introducing

the reader to the different types of supernovae (SNe) and those that may result in a PWN. Next, pulsars, the powerhouses of PWNe and the remnants of SN explosions, are discussed. A detailed discussion follows where PWNe are described by mentioning their characteristics, evolution as well as their multi-wavelength observational properties. A summary of the current and next-generation telescopes is given in the last part of this chapter.

- **Chapter 3** describes the transport equation that governs the motion of particles in the system as well as the radiation mechanisms responsible for the radiation from PWNe.
- At the core of this thesis is **Chapter 4** that describes the development and implementation of a spatio-temporal leptonic emission code. This code is developed to model PWNe by implementing the transport equation mentioned earlier as well predicting the radiation spectra at different positions in these sources.
- **Chapter 6** relates how the model outputs were fit to three different sources, PWN 3C 58, PWN G21.5−0.9 and PWN G0.9+0.1 by introducing and applying a new test statistic.
- A summary of the thesis and future prospects can be found in **Chapter 7**.
- Some additional information regarding fitting and mathematical results are given in the **Appendix**.

1.3 Publications that have resulted from this Thesis

The following is a list of the publications that resulted from this study either being a full journal paper or a conference proceedings article.

- "Exploiting Morphological Data from Pulsar Wind Nebulae via a Spatio-Temporal Leptonic Transport Code", van Rensburg C., Venter C., Seyffert A.S. and Harding A.K., submitted to MNRAS.
- "Spatially-dependent modelling of pulsar wind nebula G0.9+0.1", van Rensburg C., Krüger P. P. and Venter C., 2018, MNRAS, 477, 3853.
- "Simultaneous Fitting of the Spectral Energy Density, Energy-dependent Size, and X-ray Spectral Index vs. Radius of The Young Pulsar Wind Nebula PWN G0.9+0.1", van Rensburg C. and Venter C., 2019, arXiv e-prints, arXiv:1905.07222, proceedings of the 6th Annual Conference on High-Energy Astrophysics in Southern Africa (HEASA2018).

- "Simultaneous Spectral and Spatial Modelling of Young Pulsar Wind Nebulae", van Rensburg C., Venter C. and Krüger PP., arXiv:1809.10683, proceedings of the 5th Annual Conference on High-Energy Astrophysics in Southern Africa (HEASA2017).

Chapter 2

The Conceptual Framework of Pulsar Wind Nebulae

In this chapter, I sketch and discuss the necessary background of pulsar wind nebulae (PWNe). I describe the fundamentals of how they originate and how they evolve. To this effect, I discuss SN explosions as the origin of SN remnants and their formation, with a basic discussion of the compact objects these explosions leave behind. I also discuss the current generation of telescopes that observe these objects, as well as how the next generation of telescopes will improve on the current observatories.

2.1 Supernovae

"SNe play a central role in modern astrophysics" (Vink, 2012). They are the powerhouses for several astrophysical phenomena. One such well-known phenomenon involves the interstellar medium (ISM). The ISM is energised through cosmic rays accelerated during the final collapse of a star during an SN explosion. SNe accelerate cosmic rays to energies of up to $\sim 10^4$ GeV (Lagage and Cesarsky, 1983). The VHE tail of the terrestrial cosmic-ray spectrum is attributed to extragalactic sources.

Even though SN explosions are rare events, with one occurring every 40.0 ± 10.0 yr (Tammann et al., 1994), they leave behind SN remnants (SNRs) – valuable probes of physical phenomena occurring in the Universe. For example, the study of high-redshift SNRs has played a vital role in providing evidence that the expansion of the Universe is accelerating instead of decelerating (Perlmutter et al., 1998). On the smaller scale of an SN explosion, the SNR reveals information regarding the explosion itself, e.g., the spatial and velocity distribution of heavy elements in young SNRs can yield information

about irregularities in the explosion as well as details regarding the close surroundings of the SN (Vink, 2012). SNRs are also one of the few places in the Universe where one can study the physics underlying high-Mach-number collisionless shocks.

Spectroscopy is a key observational tactic used to study SNRs. It is used to classify different types of SNRs (see Figure 2.1) and helps to distinguish between thermal and non-thermal emission from these objects. Classically, SNe were classified according to whether or not they showed signs of hydrogen absorption in their spectra (Minkowski, 1941). If an SN showed no evidence of hydrogen absorption, it was classified as Type I, and if hydrogen absorption was present, then it was labelled Type II. The more modern classification scheme adds to this delineation by distinguishing between core-collapse and thermonuclear SNe. Type I SNe can either be of the thermonuclear or core-collapse class, but Type II SNe can only originate from a core-collapse event.

2.1.1 Thermonuclear Supernovae (Type Ia)

Thermonuclear SNe (Type Ia) are explosions in which matter is accreted by a white dwarf with mass close to the Chandrasekhar limit (1.38 $M_{\odot}$) from a companion star, or where a merger of two white dwarfs takes place (Schaefer and Pagnotta, 2012). One of the key findings regarding Type Ia SNe is the relation between the peak brightness during their explosion and the post-peak decline rate of the light curve. This relation implies that Type Ia SNe are of great utility for calculating distances. This is the main concept on which the finding is based that the expansion of the Universe is accelerating (Perlmutter et al., 1998). Type Ia SNe do not result in the formation of neutron stars (Vink, 2012) and are therefore not associated with PWNe. For further details, see Vink (2012).

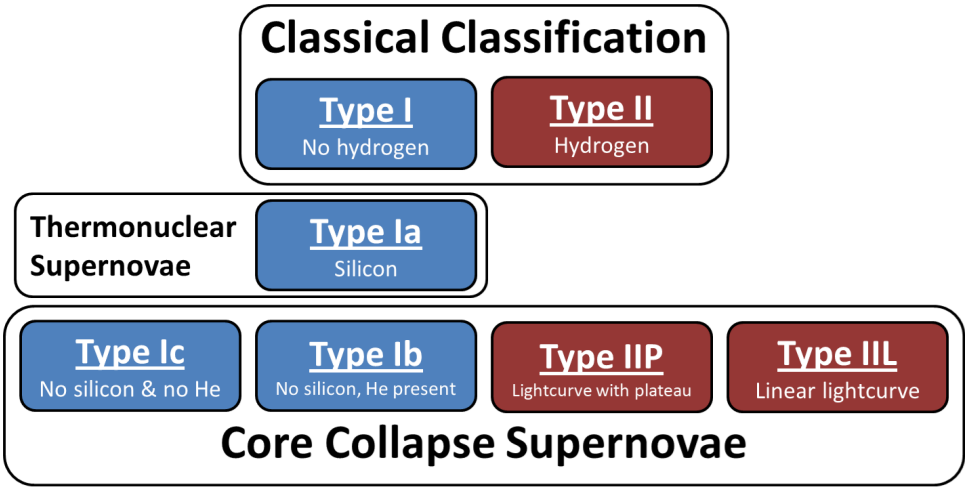

FIGURE 2.1: Classification of SNe, based on optical spectroscopy and light-curve shape (Vink, 2012).

2.1.2 Core-collapse Supernovae

The second type of SN is associated with the gravitational core collapse of a massive star (Type Ib, Ic, II). Vink (2012) describes how these are categorised by the different optical spectra they produce. Figure 2.1 shows Type Ib and Ic as sources with no evidence of hydrogen absorption in their spectra and it is understood that these sources are SN explosions where the hydrogen-rich envelope of the progenitor has been blown away as a result of the stellar wind mass loss. For Type Ic this mass loss has been so great that even the helium-rich layers have been removed and there is thus no trace of helium absorption in the spectrum.

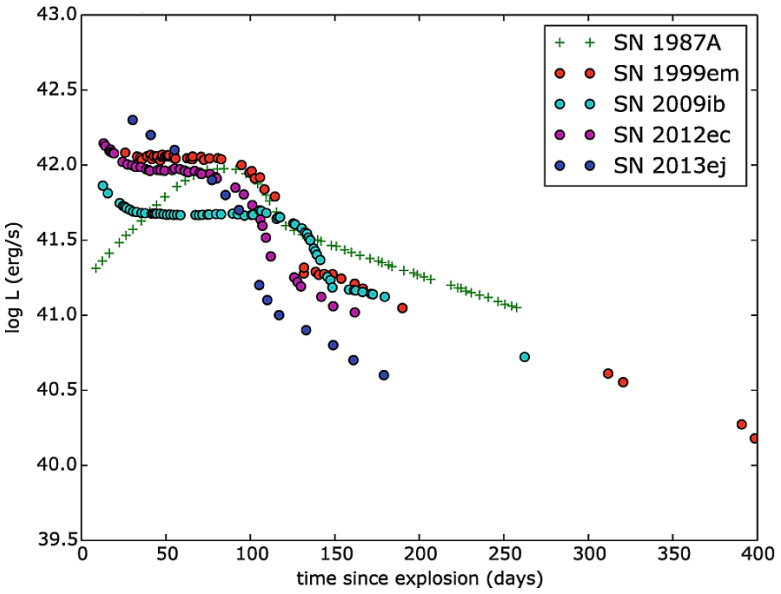

FIGURE 2.2: Bolometric light curves of Type II plateau (IIP) SNe (Zampieri, 2017).

Type II SNe are the more common type of core-collapse SNe with Type IIP being the most common subtype. Figures 2.2 and 2.3 show the bolometric light curves for Type IIP and Type IIL SNe, respectively (Zampieri, 2017). Optical studies of probable progenitor stars of Type IIP SNe found that these SNe have progenitors with initial masses of $\sim 8 - 17 M_{\odot}$ (Chevalier, 2005). These stars explode while still in their red supergiant phase, which result in them still having a vast hydrogen envelope that radiates over a longer timescale, resulting in a plateau in the light curve. Type IIL SNe have a substantially less massive hydrogen envelope, resulting in a linear light curve.

The basic mechanisms behind core-collapse SNe are similar for the different types of SNe. According to Woosley and Janka (2005) a massive star with a mass of $\gtrsim 8 M_{\odot}$ will undergo fusion of hydrogen, helium, carbon, neon, oxygen, and silicon during its lifetime. After these fusion processes have been completed, an iron-rich core is left and

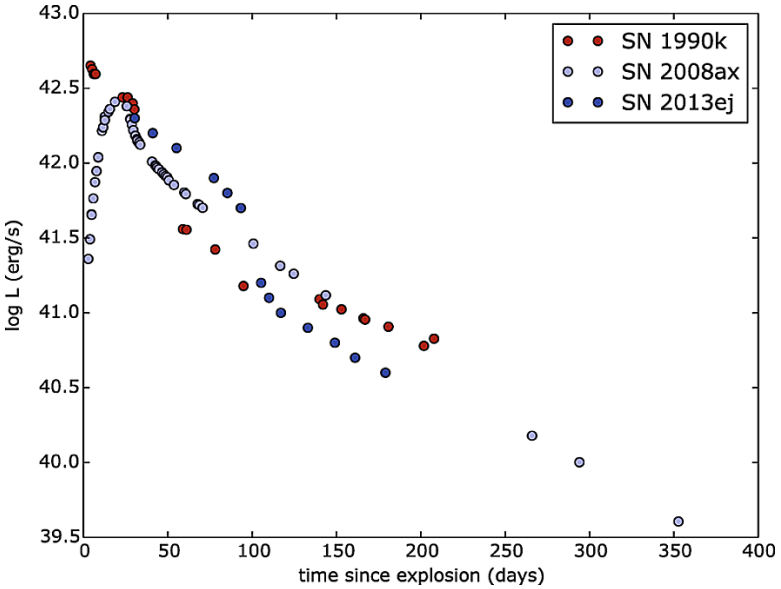

FIGURE 2.3: Bolometric light curves of Type II linear (IIL) SNe (Zampieri, 2017).

this cannot supply energy through fusion to overcome the gravitational force acting on the star, resulting in a collapse.

Once the core collapse of the star has begun, two processes dominate. First, the electrons that are responsible for the thermal pressure inside the star are pushed into the iron core. Second, the radiation photo-disintegrates a fraction of the iron core into helium. Both these processes will drain energy from the star, thereby accelerating the gravitational-collapse process. In the collapse process, a proto-neutron star is formed, where the short-range nuclear forces stop the collapse. This proto-neutron star will radiate approximately 10^{53} erg of energy, 99% of this in the form of neutrinos (Molla and Lincetto, 2019) within a few seconds, the remnant being a neutron star with a radius of approximately 10 km.

Approximately 10^{51} erg of kinetic energy is deposited into the stellar material surrounding the proto-neutron star, creating a bubble of radiation and electron-positron pairs. The explosion creates a forward shock wave that accelerates the ambient matter that collects in a thin shell behind the shock, creating a well-known shell-type SNR. According to McKee (1974) the pressure inside the shell will drop due to the adiabatic losses suffered by the ejecta, so that the pressure inside the shell will be lower than the pressure beyond the forward shock. This will result in a reverse shock being forced back to the centre of the shell. While the forward shock moves out into the ejecta, the reverse shock heats, compresses, and decelerates the ejecta. The ejecta are separated from the shocked ISM by means of the reverse shock. The time needed for this reverse shock to

propagate back to the PWN centre was derived by Ferreira and de Jager (2008a) as

$$t_{\rm rs} = 4 \times 10^3 \left(\frac{\rho_{\rm ism}}{10^{-24}{\rm g\ cm^{-3}}}\right)^{-1/3} \left(\frac{E_{\rm snr}}{10^{51}{\rm erg}}\right)^{-45/100} \left(\frac{M_{\rm ej}}{3M_\odot}\right)^{3/4} \left(\frac{\gamma_{\rm ej}}{5/3}\right)^{-3/2} {\rm yr}, \quad (2.1)$$

where $\rho_{\rm ism}$ is the density of the ISM, $E_{\rm snr}$ is the kinetic energy released in the SN explosion, and $M_{\rm ej}$ and $\gamma_{\rm ej}$ are the mass and adiabatic index of the ejecta, respectively. By inserting typical values of $E_{\rm ej} = 10^{51}$ erg, $\gamma_{\rm ej} = 1.67$, $M_{\rm ej} = 5M_\odot$, and $\rho_{\rm ism} = 10^{-24}$g cm^{-3}, we find $t_{\rm rs} \approx 6\ 000$ yr.

The morphology of the reverse shock is not necessarily spherical as shown in Figure 2.4. If the SNR is expanding into a non-homogeneous ISM or circumstellar material (CSM), the reverse shock will be offset to one direction. This, combined with the proper motion of the pulsar, usually due to a kick velocity received during the SN explosion, can cause the PWN to have a non-spherical morphology. An example can be seen in the right-hand panel of Figure 2.4 that shows the results of a hydrodynamical simulation of an SN with a density gradient in the ISM to the right and a pulsar kick velocity facing upwards (Slane, 2017).

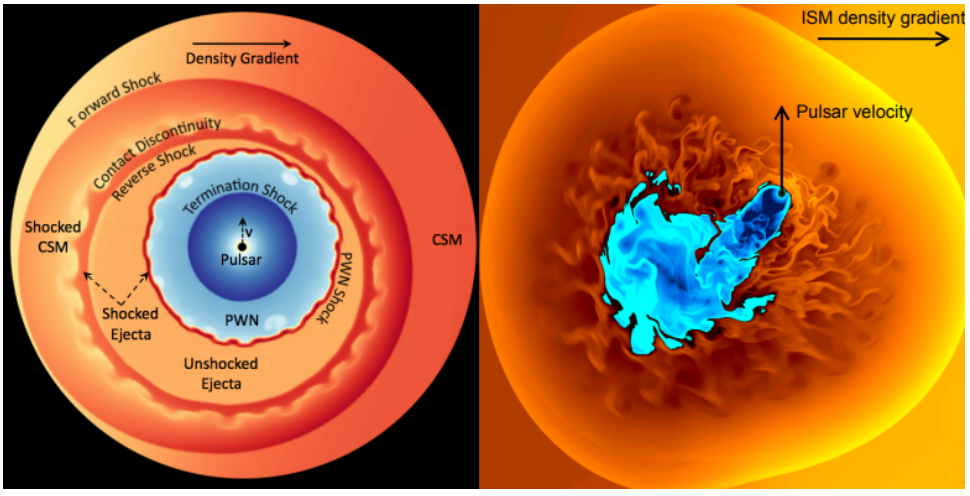

FIGURE 2.4: *Left*: Hydrodynamical simulation of a PWN expanding into an SNR. The SNR is evolving into a part of the circumstellar material (CSM) with a density gradient increasing to the right. *Right*: Hydrodynamical simulation of an evolved composite SNR (Slane, 2017).

2.2 Pulsars

In the previous Section, I mentioned how some stars die during massive SN explosions. In this Section, I will discuss pulsars as one possible end product from the aftermath of the explosion. A pulsar is the central engine that powers a PWN via its reservoir of rotational energy.

Lyne (2006) mentions that in 1934 two astronomers, Walter Baade and Fritz Zwicky, proposed the existence of a new type of star called a neutron star. Such a neutron star represents one endpoint of the stellar life cycle. They wrote:

> *...with all reserve we advance the view that an SN represents the transition of an ordinary star into a neutron star, consisting mainly of neutrons. Such a star may possess a very small radius and an extremely high density.*

It took more than 30 years after this remark before pulsars were observationally detected. The realisation that a pulsar is a rapidly-rotating neutron star finally validated this proposal. For a full discussion on the discovery of pulsars, see Lyne (2006).

Richards and Comella (1969) studied the pulsar NP 0532 and found that the period (P) of the pulsar was not constant, but instead it increased as time passed. The rate of this increase $\dot{P} = dP/dt$ can be related to the loss of rotational kinetic energy $E_{\rm rot}$ from the pulsar (Ostriker and Gunn, 1969, Lorimer and Kramer, 2005)

$$L = \left|\frac{dE_{\rm rot}}{dt}\right| = \frac{d(I\Omega^2/2)}{dt} = I\Omega\dot{\Omega} = 4\pi^2 I\dot{P}P^{-3}, \tag{2.2}$$

where $\Omega = 2\pi/P$ is the angular speed, I the moment of inertia, and L (also sometimes denoted by $\dot{E}_{\rm rot}$) the spin-down luminosity of the pulsar. It is commonly assumed that the pulsar's rotational energy is dissipated through three main effects. A small fraction $\eta_{\rm rad}$ of the spin-down luminosity is converted into pulsed emission, with a larger fraction of the spin-down luminosity being carried away from the pulsar in the form of a pulsar wind (Amato, 2003). The remaining fraction of $\dot{E}_{\rm rot}$ sustains the Poynting flux (electrical and magnetic fields) of the pulsar. The value of $\eta_{\rm rad}$ is very difficult to calculate, but Abdo et al. (2010) found observationally in the *Fermi*-LAT First Pulsar Catalogue that $\eta_{\rm rad} \approx 1\% - 10\%$, with $\eta_{\rm rad} \approx 1\%$ for the Crab pulsar. This confirmed the assumption that the largest fraction of $\dot{E}_{\rm rot}$ is therefore eventually converted into particle acceleration and gives birth to the pulsar wind that powers the PWN. To understand how the pulsar's spin-down luminosity is converted into usable energy for the PWN, it is useful to consider the wind magnetisation parameter σ that is defined as the ratio of the wind Poynting flux to the kinetic energy flux (ratio of the magnetic energy density to the particle energy density; Kennel and Coroniti 1984a). For the magnetosphere of a pulsar, $\sigma \gg 1$ due to the extremely large magnetic field close to the pulsar. The pulsar surface magnetic field can be estimated as (Belvedere et al., 2015)

$$B\sin\chi = \left(\frac{3c^3}{8\pi^2}\frac{I}{R^6}P\dot{P}\right)^{\frac{1}{2}}, \tag{2.3}$$

with R the radius of the star and χ the inclination angle between the magnetic dipole and the rotational axis of the pulsar. For typical pulsar values this evaluates to an equatorial magnetic field strength of $B \sin\chi = 3.2 \times 10^{19} \left(P\dot{P}\right)$ G. This is in strong contrast to the PWN environment where 1D models derive that $\sigma \sim 10^{-3}$, (see, e.g., Rees and Gunn, 1974, Kennel and Coroniti, 1984b, Begelman and Li, 1992). This sudden drop between the σ values of the pulsar magnetosphere and the PWN is known as the σ-problem and several explanations of how this is possible have been put forward over the years. The most common explanation is that the electromagnetic energy in the pulsar wind is converted into kinetic energy in the wind on its way from the pulsar to the termination shock (the radius from the central pulsar where the ram pressure of the wind is balanced by the pressure inside the nebula, Slane 2017), where plasma is injected into the PWN. Claims have been made that MHD acceleration mechanisms can provide the required energy conversion (see e.g., Vlahakis, 2004). This may, however, not be the case as Porth et al. (2013) argue that magnetic dissipation plays a significant role, but the length scale for this is larger than the PWN's termination shock, making this not a viable solution to the problem. Another possible solution is that the magnetic fields dissipate at the termination shock. Porth et al. (2013) note that by solving the MHD PWN problem in three dimensions allows one to find a similar termination shock radius modelled by other authors, but allowing a larger value for σ, therefore resulting in a less dramatic change in σ from the pulsar magnetosphere to the termination shock of the PWN.

A good approximation for the amount of energy injected into a PWN was given by Pacini and Salvati (1973). They noted that, while the electrodynamics involving pulsars remains controversial, the rotational energy loss rate of a pulsar may be written as

$$L(t) = L_0 \left(1 + \frac{t}{\tau_c}\right)^{-(n+1)/(n-1)}, \tag{2.4}$$

where L_0 is the luminosity at the birth of the pulsar, n is the braking index of the pulsar given by (Lorimer and Kramer, 2005)

$$n = \frac{\Omega\ddot{\Omega}}{\dot{\Omega}^2}, \tag{2.5}$$

and t is the time. For a dipolar magnetic field in vacuum, $n = 3$, as I will assume in Chapter 4.

Another variable used in the modelling of a PWN is the characteristic spin-down timescale of the pulsar, defined as (Pacini and Salvati, 1973, Venter and de Jager, 2007)

$$\tau_c = \frac{P}{(n-1)\dot{P}} = \frac{4\pi^2 I}{(n-1)P_0^2 L_0}, \tag{2.6}$$

with P_0 the birth period of the pulsar.

The above equations will enable us to model the injection of particles as described in Section 4.4.

2.3 Pulsar Wind Nebulae

In this section I will discuss the characteristics, evolution and recent observational properties of PWNe. For more details, see, e.g., the reviews by Gaensler and Slane (2006), Kargaltsev and Pavlov (2008), Amato (2014) and Bucciantini (2014) for PWN modelling, observations and theory.

PWNe are formed subsequent to SN explosions, as mentioned earlier, and the earliest recording of an SN explosion was in 1 054 AD by Chinese astronomers (Stephenson and Green, 2002). This object is known today as the Crab Nebula and is one of the most well-known PWNe. The link between the SN explosion and a pulsar energising the system came as a result of several observational attempts made in the early to middle part of the twentieth century. In an attempt to link the "guest star" observed in the Crab Nebula with the SN explosion, Mayall and Oort (1942) observed the Crab Nebula at the Leiden Observatory during the last part of 1941 and found that the star has a maximum magnitude of 16.5. Baade (1942) confirmed these observations and added that the Crab SN was of Type II. Minkowski (1942) then postulated that this 16.5 magnitude "guest star" could be the remnant of the SN explosion. It did, however, take several years before any further advancements were made, but in February of 1969 Cocke et al. (1969) reported the discovery of optical pulsations from this "guest star", with X-ray (Fritz et al., 1969) and gamma-ray (Hillier et al., 1970) pulsations also observed. By then it was also known that a radio counterpart (NP 0532) was situated in the Crab Nebula. In May of 1969 Comella et al. (1969) confirmed the period of the pulsar in a letter to Nature where they described their follow-up radio observations of NP 0532. Later, in July 1969, Gold (1969) proposed that the kinetic energy dissipated from the pulsar, as discussed in Section 2.2, was similar in magnitude to the energy presumed to be injected into the SNR at that time. After this discovery a theoretical understanding was developed where, instead of a pulsar being completely isolated and its magnetised relativistic pulsar wind expanding indefinitely, the pulsar is surrounded by the SN ejecta. This led to the onset of a whole new field of research into these sources now known as PWNe.

2.3.1 Characteristics of a PWN

According to De Jager and Djannati-Ataï (2009), a PWN has the following defining characteristics:

- Weiler and Panagia (1978) coined the phrase "plerion", derived from the Greek, which alludes to "filled bag". This refers to a filled morphology, being brightest at the centre and dimming in all directions towards the edges. This is observed in all directions at all wavelengths and is due to the constant injection of energy by the central embedded pulsar, accompanied by the cooling of particles as they diffuse through the PWN;
- PWNe show signs of a structured magnetic field as inferred from polarisation measurements in both radio (Reynolds et al., 2012) and X-ray bands (Reynolds, 2016);
- A PWN has an unusually hard radio synchrotron spectrum. If N_e is the particle number density, then the particle spectrum producing the radio emission is described by $N_e \propto E^{-p}$, with p equals to 1.0−1.6;
- Particle re-acceleration occurs at the termination shock[1] and can be described by a power law (towards higher energies) as $N_e \propto E^{-p}$, with N_e the particle number density and $p \sim 2-3$. This and the previous point imply a two-component lepton injection spectrum; more detail is given in Section 3.1.1.
- Some of the observed PWNe have a torus as well as a jet in the direction of the rotational axis of the embedded pulsar. In these cases the torus displays an underluminous region at approximately $r_{ts} = 0.03 - 0.3$ pc, with r_{ts} the radius of the termination shock.
- There is evidence of synchrotron cooling which means that the size of the X-ray PWN decreases with increasing energy.

The characteristics of a PWN can be expanded by using VHE gamma-ray observations (De Jager and Venter, 2005):

- The magnetisation parameter σ (ratio of electromagnetic to particle energy flux, Kennel and Coroniti 1984b) of the pulsar wind is less than unity, with $\sigma \approx 0.003$ for the Crab Nebula and $0.01 \leq \sigma \leq 0.1$ for the Vela PWN. This is small when compared to the magnetisation parameter inside the magnetosphere of a pulsar where $\sigma \approx 10^3$ (although, see Section 2.2).

[1] The termination shock is assumed to be the inner boundary of the PWN and is discussed in Section 2.3.2.

- The magnetic field of a PWN can be very weak due to its rapid expansion. This can cause the VHE gamma-ray producing electrons to survive for a long time. If the magnetic field drops below a few μG it can lead to a source that is undetectable at synchrotron frequencies but still detectable at TeV energies. This is a possible explanation for the number of unidentified TeV sources seen by H.E.S.S. Alternatively, "relic PWN" may form in late stages of the evolution, where the B-field has dropped with time, leading to VHE sources with no low-energy counterparts.

2.3.2 PWN Evolution

PWNe are highly time-dependent objects as their evolution is tightly linked to the evolution of the pulsar's spin-down luminosity (Gaensler and Slane, 2006), as well as the fact that the pulsar usually receives a kick velocity, plus the interaction of the reverse shock during the SN explosion with the nebula.

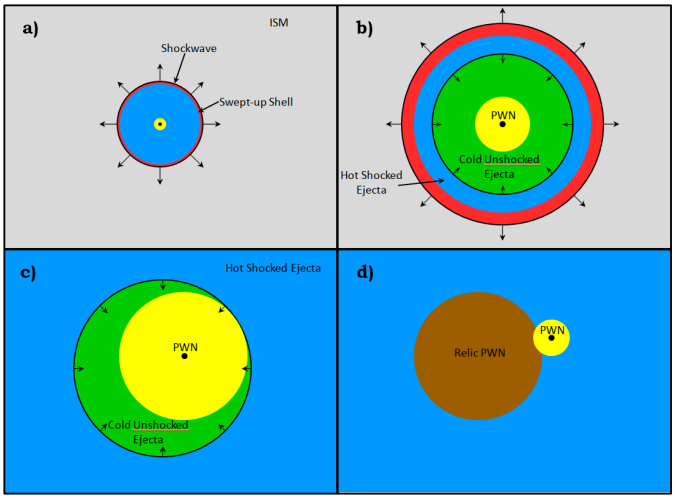

FIGURE 2.5: Schematic of the main eras in a PWN's life cycle. *Panel (a)*: Shortly after the SN explosion ($\sim$ 200 yr) the SN ejecta move outward with a PWN freely expanding into the unshocked ejecta. *Panel (b)*: At $\sim$ 1000 yr, a reverse shock forms that propagates inward towards the PWN. *Panel (c)*: The reverse shock reaches and compresses the PWN *Panel (d)*: The reverse shock dissipates and the pulsar is free to power a new PWN. (Kothes, 2017).

PWNe can be separated into two main groups. The first is "young" PWNe. These are PWNe in which there has been no interaction between the reverse shock of the SN explosion and the nebula; consider Figure 2.5 panel (a). The rest of the PWNe can be considered "old" and these usually exhibit interesting morphologies.

Panel a of Figure 2.5 shows what the SN explosion would look like after about 200 yr. Here we find a freely-expanding shell-type SNR with a spherically-symmetric PWN at the centre. As with most SN explosions, the pulsar has received some kick velocity, but

this velocity can be neglected at this early stage of the PWN's lifetime. During this phase the pulsar injects energy into the nebula, causing the PWN to expand supersonically into the slower-moving surrounding stellar ejecta (Slane, 2017). The growth of the PWN radius scales as $R_{\rm pwn} \propto t^{\beta}$, where $R_{\rm pwn}$ is the outer boundary of the PWN, t the age of the PWN, and $\beta \sim 1.1 - 1.2$ (Reynolds and Chevalier, 1984). A more recent study showed that this estimate can be refined by assuming a spherical geometry for the nebula and a radial power-law density distribution for the SN ejecta. The radius of the PWN at any given time can be approximated by (Chevalier, 2004):

$$R_{\rm PWN} = 1.87 \left(\frac{\dot{E}_{\rm rot}}{10^{38}\ {\rm erg/s}}\right)^{0.254} \left(\frac{E_0}{10^{51}\ {\rm erg}}\right)^{0.246} \left(\frac{M_0}{M_\odot}\right)^{-0.5} \left(\frac{t}{10^3\ {\rm yr}}\right) ({\rm pc})\,, \qquad (2.7)$$

with $\dot{E}_{\rm rot}$ the spin-down luminosity of the pulsar (in this case assumed to be constant), E_0 the explosion energy of the SN, M_0 the mass of the SN ejecta and $M_\odot$ a solar mass. Figure 2.6 shows an example of a young PWN (PWN G21.5−0.9) that is still in the free-expansion phase. In this figure we can clearly see the SNR with the illuminated PWN at the centre.

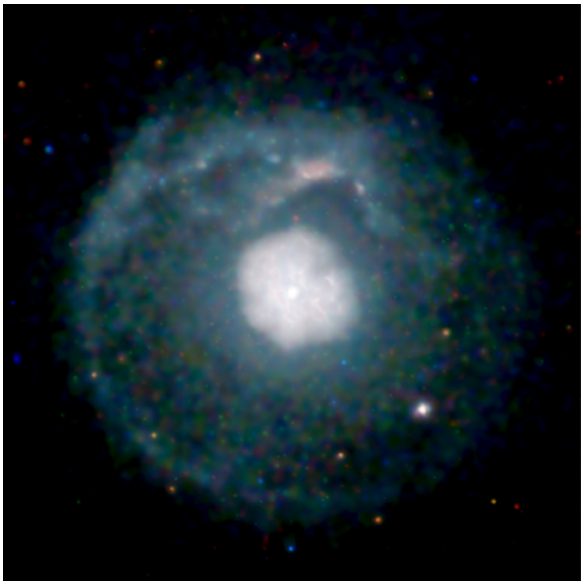

FIGURE 2.6: *Chandra* image of G21.5−0.9. Red corresponds to 0.2−1.5 keV, green to 1.5−3.0 keV, and blue to 3.0−10.0 keV. The entire remnant is shown with the plerion visible in the centre (Matheson and Safi-Harb, 2005).

The blast wave of the SN explosion sweeps up more and more interstellar material and around $800 - 2\,000$ yr (McKee and Truelove, 1995), the swept-up material forms a shell on the inside of the blast wave. This shell is highly compressed against the low pressure of the unshocked SN ejecta, and thus a reverse shock is formed that propagates towards the centre of the SNR, see Figure 2.5. Some time later, usually around a few thousand years (Kothes, 2017), the reverse shock collides with the outer boundary of the PWN.

This collision causes reverberations that induce oscillations in the PWN. This can reheat and compress the PWN, resulting in the most complex part of the PWN's evolution. These interactions between the reverse shock and the PWN can last for several thousands of years (Van der Swaluw et al., 2004). After the oscillation phase of $R_{\rm pwn}$, the PWN enters another phase of steady expansion due to the ejecta being heated by the reverse shock. This second phase of steady expansion is characterised by the subsonic expansion of $R_{\rm pwn}$. According to Reynolds and Chevalier (1984), this expansion follows a power law given by $R_{\rm pwn} \propto t^{\beta}$, with $\beta \sim 0.3 - 0.7$.

As a first approach, it is commonly assumed that the PWN and the reverse shock are spherically symmetric. This is a good starting point but we know that this is not the full reality; in fact, PWNe are much more complex. Blondin et al. (2001) performed simulations where the SNR is not expanding into a homogeneous ISM, but instead they added some inhomogeneity in the form of a pressure gradient to simulate the presence of, for example, a molecular cloud next to the SNR. As a result of the pressure inhomogeneity, the reverse shock will be asymmetric, causing the nebula to be displaced from the pulsar. This causes the morphology of the PWN to have a "bullet" shape, with the pulsar located in the tip of the "bullet". This is seen in many H.E.S.S. sources, so-called "offset-PWNe". Figure 2.7 shows such an example. Another cause for the PWN to exhibit a bullet shape can be due to the pulsar having some kick velocity with respect to the SNR, and thus it will also move away from the centre and form a bullet shape.

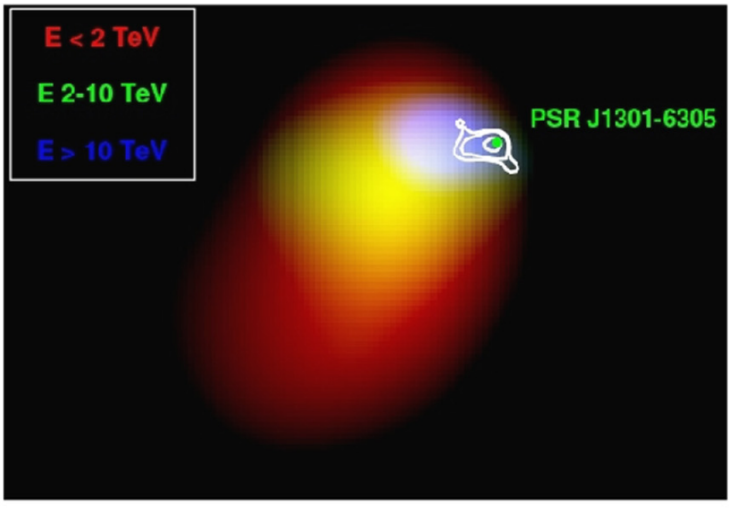

FIGURE 2.7: HESS J1303−631 showing a "bullet-shaped", asymmetric PWN. The red indicates photons below 2 TeV, yellow photons between 2 and 10 TeV, and blue photons above 10 TeV. *XMM-Newton* X-ray contours are superimposed in white (Abramowski et al., 2012a).

In the extreme case where the pulsar received a large initial kick velocity and finds itself in a very old system, this may result in intricate PWN morphologies. SNR G5.4−1.2 is a good example of this and its radio morphology can be seen in Figure 2.8. This SNR was observed by the 100-m Effelsberg Radio Telescope (Kothes, 1998) at a frequency of 10.45 GHz. In this system it is presumed that the pulsar was born in the geometric centre of the SNR with a very large kick velocity towards the western direction. As a result, the pulsar has completely left the original SNR and is now powering a new PWN. The expanding wind is not energising the SN ejecta anymore, but the ISM.

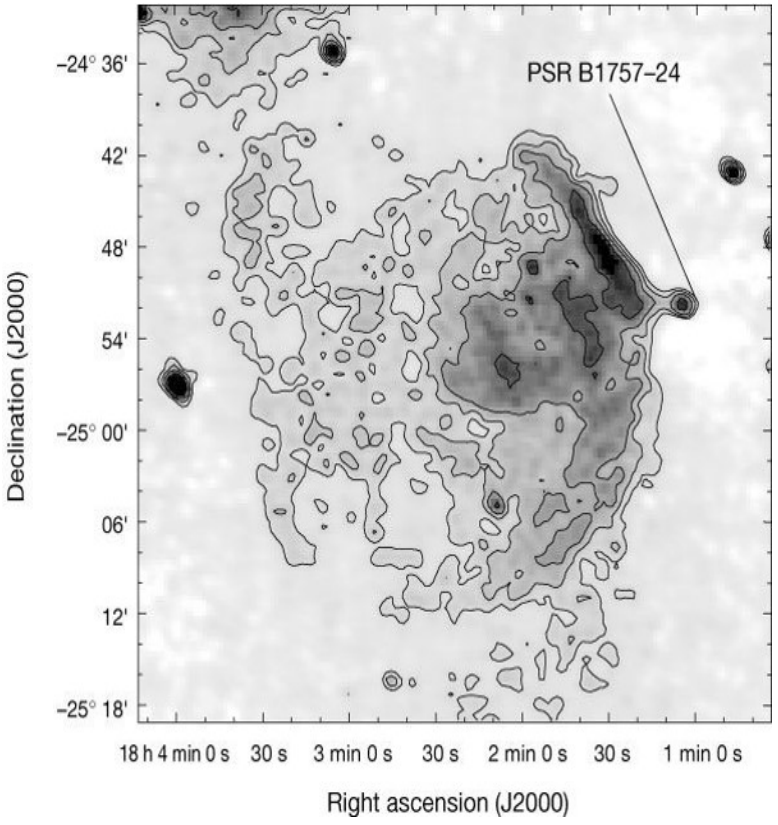

FIGURE 2.8: SNR G5.1−1.2 as observed by the 100 m Effelsberg Radio Telescope (Kothes, 1998). The location of pulsar PSR B1757−24 is shown on the right where it has left the original SNR and is powering a small surrounding PWN.

2.3.3 Multiwavelength Observational Properties of PWNe

PWNe are true multi-wavelength objects. To observe these objects we use telescopes and satellites able to observe them from the radio band all the way up to gamma-ray energies. Next I will discuss how these sources look in the different energy bands and then provide more detail regarding some of the telescopes in Section 2.4.

2.3.3.1 Radio Emission from PWNe

PWNe are bubbles filled with relativistic particles. These relativistic particles move not only through space but through the magnetic field of the nebula as well. These particles will produce linearly polarised synchrotron radiation (SR), which is typically characterised by a power law (Longair, 2011):

$$S(\nu) \sim B_{\perp}^{\frac{1}{2}(p+1)} \nu^{-\frac{1}{2}(p-1)} \sim \nu^{\alpha}, \tag{2.8}$$

where $S(\nu)$ is the flux density at some frequency ν, $\alpha = -\frac{1}{2}(p-1)$ the spectral index and $B_{\perp}$ the magnetic field perpendicular to the line of sight (Kothes, 2017). Radio PWNe typically have a flat radio continuum spectrum with indices ranging between $\alpha = -0.3$ and $\alpha = 0.0$ as found by a population study done by Green (2014) and the results can be seen in Figure 2.9. The synchrotron spectrum is also an indication of the spectrum of the underlying relativistic particles causing the SR. This particle spectrum is given by

$$N(E)dE \sim E^{-p}dE, \tag{2.9}$$

where $N(E)$ is the number of particles with energy E in an interval dE. The synchrotron spectra of PWNe show two different types of spectral breaks. The first and the more well understood is the synchrotron cooling break occurring somewhere in the spectrum between the radio and X-ray energy bands. More information can be found in Section 2.3.3.3. The second type of break that can occur is attributed to intrinsic acceleration mechanisms. This is not well understood and is therefore not further discussed in this thesis.

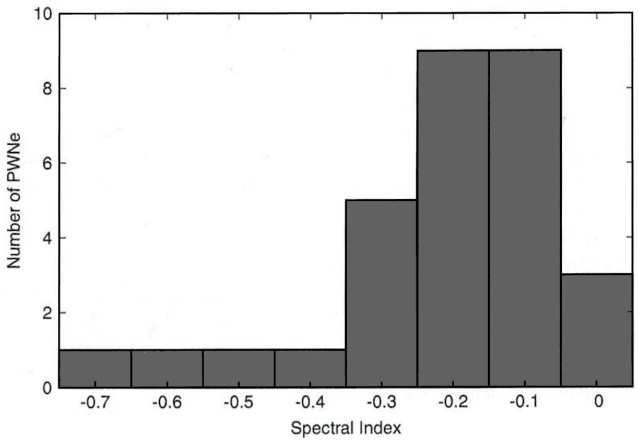

FIGURE 2.9: Number of PWNe as a function of radio spectral index α (Kothes, 2017).

Another powerful tool is radio polarimetry. It is a tool for studying the magnetic field

structure inside a PWN as the synchrotron emission is linearly polarised, with the E-vector perpendicular to the magnetic field at the point of origin. This is, however, not the only effect that influences the polarisation. Faraday rotation of the emission in the line of sight of the observer is expressed as a rotation measure (RM) with

$$\phi_{\rm obs}(\lambda) = \phi_0 + RM\lambda^2({\rm rad}). \tag{2.10}$$

Here ϕ_0 is the intrinsic polarisation angle and $\phi_{\rm obs}(\lambda)$ is the observed angle of rotation at the wavelength λ. Thus, by observing the PWN at different frequencies in the radio band, it is possible to deduce the Faraday rotation, yielding information about the magnetic field in the intervening ISM in our line of sight. This knowledge can then be used to figure out what the magnetic field is inside the PWN. This is not a simple task as the synchrotron material producing the initial polarised emission is mixed with the Faraday-rotating plasma and therefore we rely on models, e.g., Burn (1966), to investigate the magnetic field of a PWN.

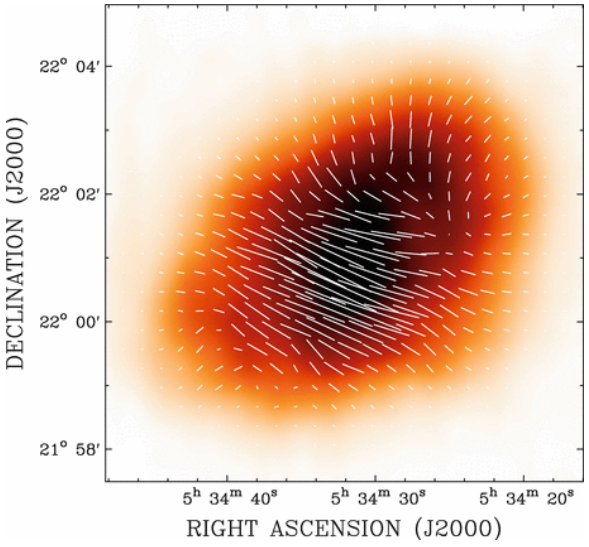

FIGURE 2.10: Radio continuum image of the Crab Nebula observed with the 100-m Effelsberg Radio Telescope with the overlayed vectors in the B-field direction (Kothes, 2017).

Typically, magnetic fields inside PWNe are assumed to be toroidal and decrease (in the absence of field compression) with radius R as $B_{\rm tor} \sim R^{-1}$. Poloidal magnetic fields are also present in some PWNe and these decrease with radius as $B_{\rm pol} \sim R^{-2}$. For example, Figure 2.10 shows the radio image of the well-known Crab Nebula with the vectors indicating the magnetic field direction projected onto the plane of the sky. In this example, the Crab Nebula shows mostly toroidal magnetic fields in the equatorial region with poloidal magnetic fields at the edges. Due to this two-component magnetic field, young PWNe usually show signs of elongation (Temim and Slane, 2017) and this may be as a result of higher pressure in the equatorial region (Kothes, 2017). In, e.g.,

PWN 3C 58, the spin axis of the pulsar is observed to be parallel to the elongation of the PWN.

2.3.3.2 Optical and Infrared (IR) Emission from PWNe

Somewhere between radio and X-ray observations a break should occur in the non-thermal synchrotron spectrum of PWNe (see Section 2.3.3.3). Therefore, it is relevant to discuss the observation of PWNe in the optical energy band.

Observations of PWNe in the mm to optical energy ranges are scarce due to the effects of extinction at optical and high source confusion at IR frequencies. Some of the brightest PWNe (Crab Nebula, PWN 3C 58, PWN G21.5-0.9 and PWN G292.0+1.8) have, however, been observed at these frequencies (Temim and Slane, 2017). Observations of the Crab Nebula have yielded information regarding the spatial variation in the spectral properties as well as time variability in the small-scale knot and wisp structures in the Nebula (Tziamtzis et al., 2009). The global spectral values for the Crab Nebula are $\alpha = 0.8$ for the optical spectrum and $\alpha = 0.5$ for the IR. The spectral index does generally steepen with distance from the central pulsar due to synchrotron cooling. Detailed analysis of differences in the spectral variation led to the interpretation that this is due to a superposition of multiple synchrotron components that may be an indication of multiple particle populations (Temim and Slane, 2017). Such multiple particle populations are most likely the reason for the great differences in PWN morphologies across different wavelengths. Bandiera et al. (2002) performed a study where they investigated the change of the morphology of the Crab Nebula when observed at radio and X-ray energies and found that the more extended nebula is dominating at radio frequencies and the inner torus is dominating in the X-ray band. This, together with other evidence gathered by the *Spitzer* telescope (Temim et al., 2006), suggests that there is a flat torus superposed on a smooth extended nebula whose index steepens as one moves away from the central pulsar.

Another aspect of PWNe that can be observed in the optical energy band is the black body thermal radiation from the gas and dust in the SN ejecta. The black body radiation is usually confined to filaments in the gas and depends on the velocity of the PWN shock that is driven into the gas in the SNR. These observations are powerful tools to determine the shock speeds in these PWNe. According to Slane (2017) one can observe slow and fast shock speeds. For slow shocks the line emission will be observed in the optical and IR energy bands, while fast shocks will emit line emission in the X-ray band. Figure 2.11 shows an example of this line emission for the shell around the PWN in SNR G54.1+0.3. The blue line is an example of the spectral line broadening observed in this sources and

is an indication of the expansion velocity of the shell. The broadening in this example relates to a shell expansion velocity of 1000 km s^{-1}.

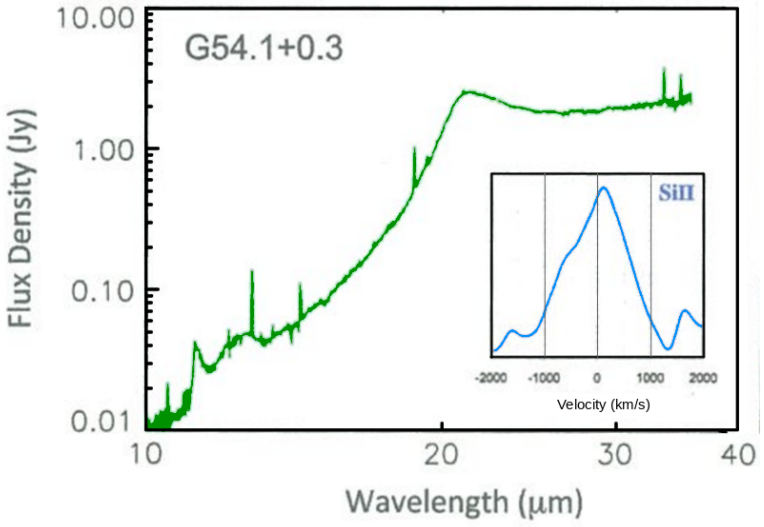

FIGURE 2.11: *Spitzer* mid-IR spectrum of the shell around the PWN inside SNR G54.1+0.3. The velocity profile of the 34.8 μm line (Si II) is shown by the blue line (Temim and Slane, 2017).

2.3.3.3 X-Ray Emission from PWNe

In the X-ray energy band, the synchrotron spectrum is characterised by the photon distribution

$$N_{\rm ph}(E) \sim E^{-\Gamma}, \tag{2.11}$$

where $N_{\rm ph}(E)$ is the number of photon radiated with an energy E. Here Γ is called the photon index and is related to α as follows: $\Gamma = 1 - \alpha$. The Γ values for typical PWNe are around 2 and increase as one moves away from the centre of the PWN due to the cooling of the relativistic particles. This is discussed more in Chapter 6.

As mentioned in Section 2.3.3.1, the synchrotron spectra of PWNe show two different types of spectral breaks. The first is known as the synchrotron cooling break. This break occurs in the spectra above energies where the synchrotron radiation energy losses become significant within the lifetime of the PWN. This effect becomes clear when one considers X-ray observations. Kargaltsev et al. (2015) showed that the synchrotron X-ray luminosity correlates well with the spin-down luminosity of the embedded pulsar (Figure 2.12). This is an indication that the radiation in this energy range is from relativistic particles with a short lifetime that is more directly related to the recent injection of particles in the system. At radio energies the emission created by lower-energy particles are not as affected by the synchrotron energy loss rate and therefore

these are a better reflection of the total (accumulated) energy content of the nebula (Kothes, 2017). This effect will cause a break somewhere in the synchrotron spectrum between radio and X-ray band. The second type of spectral break is due to intrinsic acceleration mechanisms and is not discussed any further.

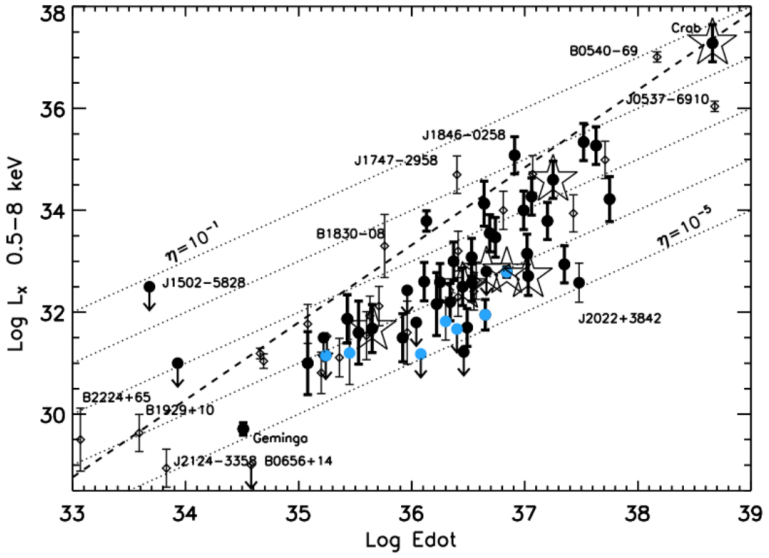

FIGURE 2.12: Correlation between the X-ray luminosity and the embedded pulsar's spin-down luminosity (Kargaltsev et al., 2015).

The development of the *Chandra* X-ray space telescope opened up a new level of understanding of PWNe with its unprecedented angular resolution and high sensitivity (Kargaltsev and Pavlov, 2008). *Chandra* has allowed us not only to detect many new PWNe, but also study their spatial and spectral structure as well as the dynamics in these systems. Kargaltsev and Pavlov (2008) noted that *Chandra* observed fifty four

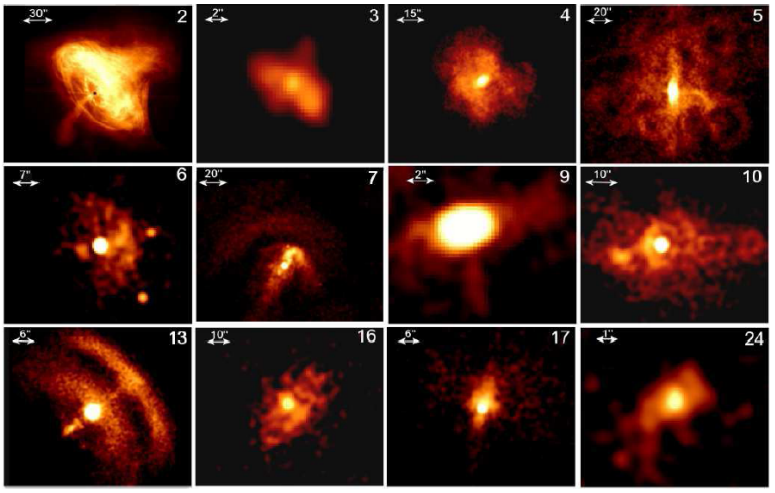

FIGURE 2.13: *Chandra* X-ray images of PWNe considered to be *torus-jet PWNe* with toroidal components (Kargaltsev and Pavlov, 2008).

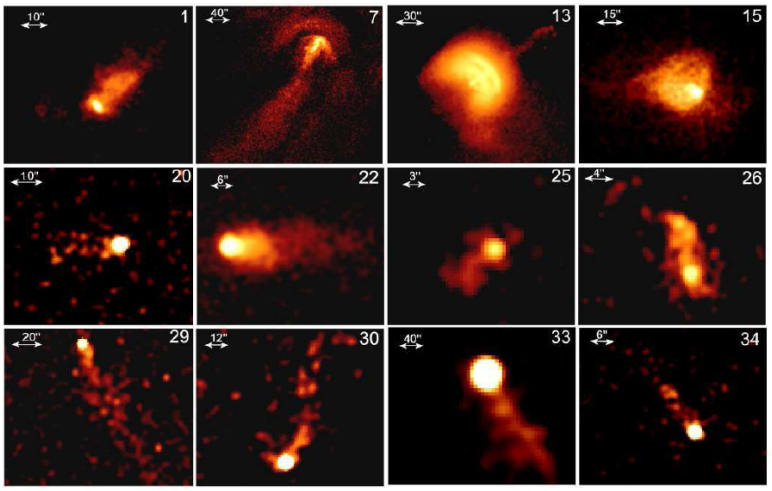

FIGURE 2.14: *Chandra* X-ray images of PWNe considered to be *bowshock-tail PWNe* where the motion of the pulsar influences the shape of the PWN (Kargaltsev and Pavlov, 2008).

PWNe with forty of them having a known pulsar associated with the nebula. The others do not show signs of a pulsar, but this could be attributed to many factors, some of which will be discussed in Section 2.4.5. This collection of PWNe shows a great diversity in morphologies. From these types of studies two main morphologies have emerged. The first of these are *torus-jet PWNe* (Figure 2.13) that show toroidal structure around the central pulsar and some show jet-like structures in the torus axis. This type of morphology is usually associated with young PWNe with panels 4 and 5 showing PWN G21.5−0.9 and PWN 3C 58, as well as the famous Crab Nebula in panel 2. The second class of PWNe are *bowshock-tail PWNe* (Figure 2.14). These are distinguished by their comet-like morphologies due to the proper motion of the pulsar. The pulsar is located at the "comet head" and this morphology is usually associated with older PWN systems. For a full list of all the PWNe shown in these figures, see Kargaltsev and Pavlov (2008).

For a larger/closer PWN source, e.g., Vela PWN, it is possible to do spatial spectroscopy due to the high resolution of X-ray telescopes. Figure 2.15 is an example where the photon index the Vela PWN is shown for different positions in the source. This allows one to determine the photon index as function of radial distance from the central pulsar and is a tool utilised in this study.

2.3.3.4 The Gamma-ray Sky and PWN Observations

It is possible to obtain a complementary picture of the sky by observing at gamma-ray energies. This is due to the fact that electrons that upscatter photons, e.g., cosmic microwave background (CMB) photons (in the Thomson limit, see Section 3.2.2) to TeV

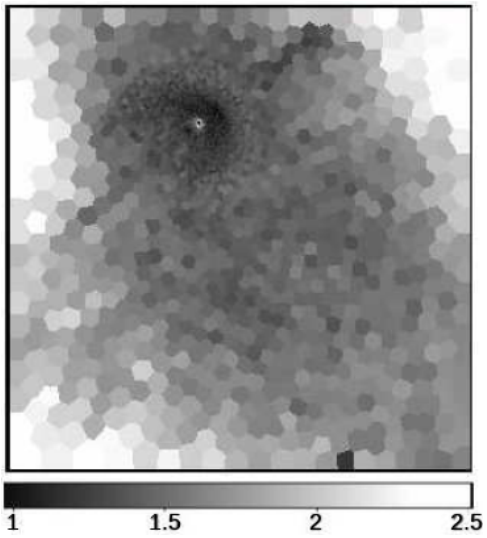

FIGURE 2.15: *Chandra* X-ray photon index map of the Vela PWN indicating synchrotron cooling as the distance from the central pulsar increases (Kargaltsev and Pavlov, 2008).

energies have a lower energy than the electrons producing synchrotron radiation in the X-ray band (Acero, 2017). This difference in energy implies a longer lifetime for the electron population that causes the gamma-ray emission compared to that of X-ray-emitting electrons. This difference makes gamma-ray observations perfect for finding old PWNe, since such nebulae can still be bright in the VHE range but very faint or even extinct in the X-ray energy band.

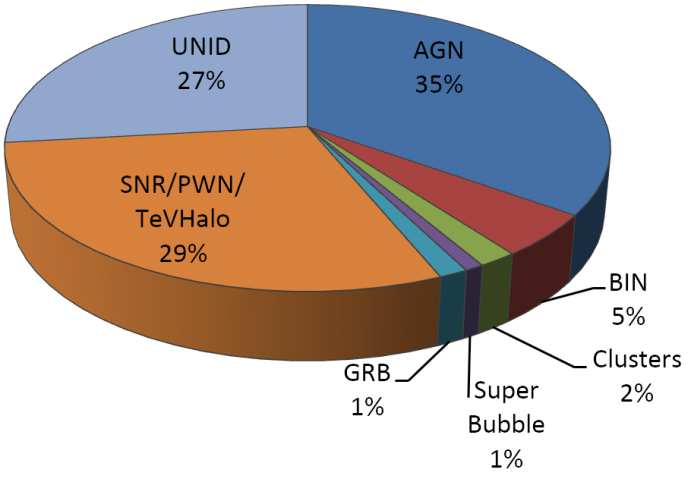

FIGURE 2.16: Different source classes as revealed by VHE telescopes. From the TeVCat[a] online catalogue.

[a]http://tevcat2.uchicago.edu/

Gamma-ray observations have yielded ~ 225 sources with $\sim 30\%$ of these being SNRs or PWNe (see Figure 2.16). There is a striking difference when one compares the number

of PWNe at TeV energies with those seen in high-energy (HE: 100 MeV−100 GeV) observations by the *Fermi*-LAT space telescope where only $\sim$ 1% of the sources are PWNe. This difference is mainly due to magnetospheric radiation of the pulsars in these systems that peak at GeV energies (Abdo et al., 2013), making it difficult to detect the faint nebular emission in the same energy band. One of the main reasons for this is due to the limited angular resolution of the *Fermi*-LAT instrument, and thus disentangling the pulsar, PWN and SNR radiation from one another is not a simple task. A method used to disentangle the different radiation components is the so-called "gating" method that is similar to the process used in the radio band mentioned later in Section 2.4.5 (see, e.g., Grondin et al., 2013, Schutte and Swanepoel, 2016). "Gating" is the process where the observed pulsed emission from the pulsar is analysed in certain phased intervals. The background radiation (the radiation from the PWN in our case) will then be observed during the "off" phase of the pulsar. Figure 2.17 shows the light curve used by Grondin et al. (2013) during their study of the Vela X PWN and they show how they use the small phase interval between the dashed lines as the "off" cycle of the pulsar to study underlying Vela X PWN.

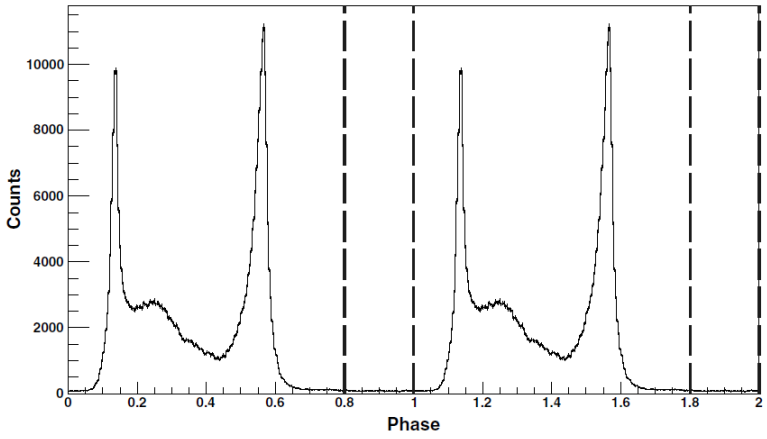

FIGURE 2.17: Gamma-ray light curve for the Vela pulsar in the 0.1−300 GeV energy range. The dashed lines delimit the "off" cycle of the pulsar that is used to analyse the emission Vela X PWN (Grondin et al., 2013).

Current gamma-ray telescopes have relatively large point spread functions (PSFs) making it difficult to observe morphologies of PWNe at TeV energies. The H.E.S.S. telescope array has, however, been able to observe extended VHE emission form Vela X as it is one of the nearest PWNe (Abramowski et al., 2012b). The VHE morphology of Vela X is determined in this study and surface brightnesses are calculated for two different axes in the source as well as the gamma-ray photon index as function of radial distance from the pulsar. In the left-hand panel of Figure 2.18 the spatially-dependent spectral index of Vela X can be seen. The regions where the indices were extracted, are also shown. The right-hand panel of the same figure shows the H.E.S.S. surface brightness of Vela X and from this the VHE morphology can be deduced. In this figure the location of the

pulsar is shown by the white star, with the H.E.S.S. PSF for this band shown in the bottom left.

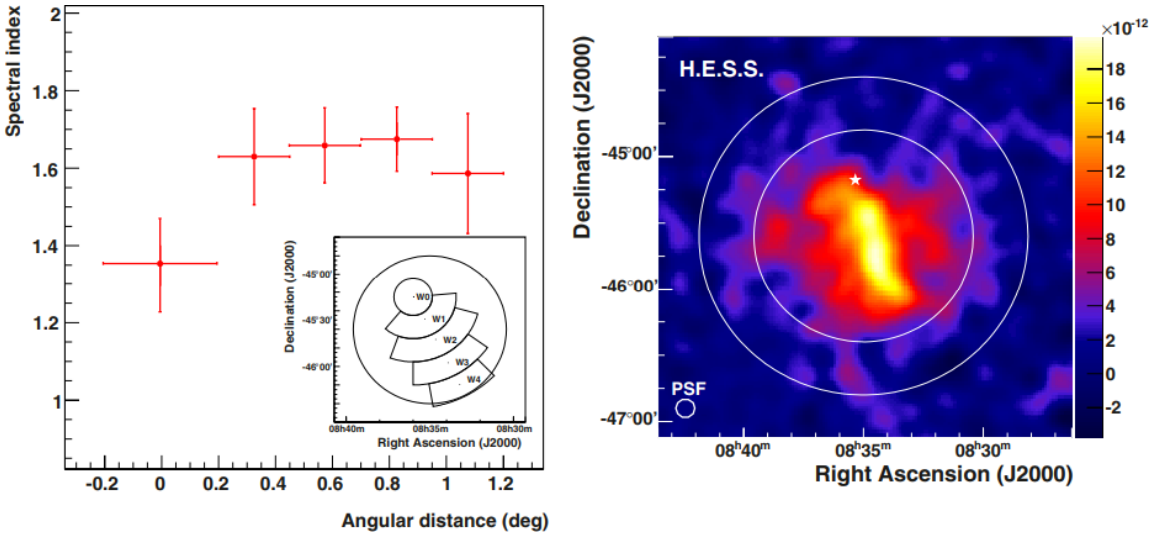

FIGURE 2.18: VHE spectral index as a function of radial distance from the central pulsar (*left*), with the zones indicated by the inset where the indices were extracted, and the gamma-ray SB (*right*) of Vela X as observed by H.E.S.S. (Abramowski et al., 2012b).

In a study involving $\sim$ 9.5 yr of *Fermi*-LAT data from Vela X, Tibaldo et al. (2018) attempted to disentangle the two spectral components of the gamma-ray emission in the 10 GeV to 2 TeV energy range to bridge the gap in the spectrum between the SR and IC components left by previous studies. The results can be seen in Figure 2.19. Here the high-energy tail of the SR component with a spectral index of $2.19 \pm 0.16^{+0.05}_{-0.22}$ may be distinguished from the low-energy tail of the IC component with a spectral index of $0.9 \pm 0.3^{+0.3}_{-0.1}$. This emphasises the utility of multiband observations.

2.4 Current and Next-Generation Observatories

In Section 2.3.3 I discussed the PWN sky as viewed in all different wavelengths. From this it is clear that PWNe are true multi-wavelength objects radiating from radio frequencies all the way up to TeV gamma-ray emission. This section is therefore dedicated to describing the current and next-generation observatories able to observe these sources. The core of this discussion will be regarding the High Energy Stereoscopic System (H.E.S.S.) telescope and the Cherenkov Telescope Array (CTA) due to my direct involvement as a member of the H.E.S.S. Collaboration as well as my contribution to the South African Gamma-Ray Astronomy Programme (SA-GAMMA). Other relevant telescopes in the lower energy bands will also be discussed at the end of this section.

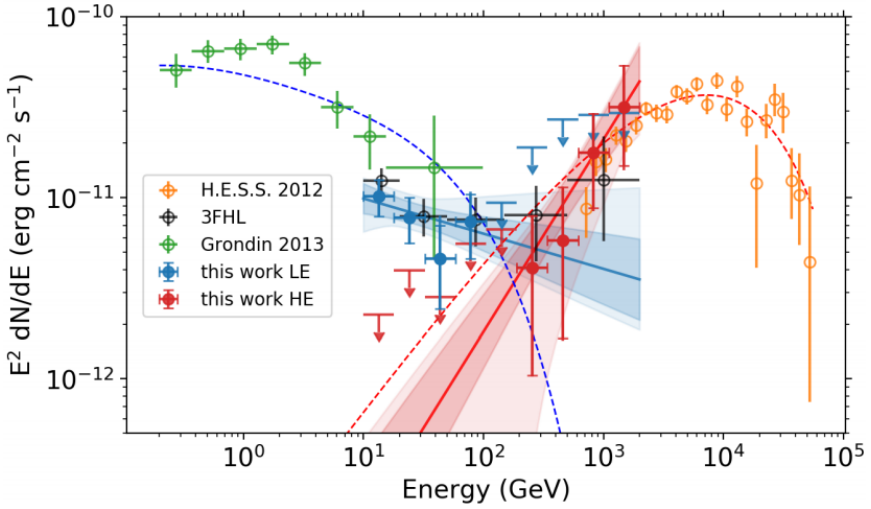

FIGURE 2.19: SED of Vela X showing the overlapping energy ranges of the *Fermi*-LAT space telescope and the H.E.S.S. telescope (Tibaldo et al., 2018).

2.4.1 Atmospheric Cherenkov Telescopes (ACTs)

There are currently three major ground-based gamma-ray telescopes in the world. These are the H.E.S.S. experiment in the Gamsberg mountain range in Namibia, the Very Energetic Radiation Imaging Telescope Array System (VERITAS) located at the basecamp of the Fred Lawrence Whipple Observatory in Southern Arizona, and the Major Atmospheric Gamma Imaging Cherenkov Telescopes (MAGIC) located near the top of the Roque de los Muchachos on the Canary Island of La Palma. The future of ACTs is the Cherenkov Telescope Array (CTA) that will have sites in both the northern and southern hemisphere (Section 2.4.1.3).

2.4.1.1 The Cherenkov Technique used by ACTs

To view gamma rays with an ACT, the Cherenkov technique is used where an incident high-energy photon interacts with particles high up in the atmosphere and generates a shower of secondary particles. Figure 2.20 is a schematic view of this process where the shower of particles reaches a maximum intensity at about 10 km and then dies off deeper into (lower down) the atmosphere. The particles move at essentially the speed of light (faster than the speed of light in the medium) in the atmosphere, emitting a faint blue light, *Cherenkov radiation*, for a couple of nanoseconds. This blue flash of light illuminates the ground around the direction of the incident particle, creating a pool of light on the ground with a diameter of $\sim$ 120 m. This is a very faint light flash, as a particle with an energy in the TeV range (10^{12} eV) will only produce about 100 photons per m^2 at ground level. If a telescope is located within the light pool it will therefore

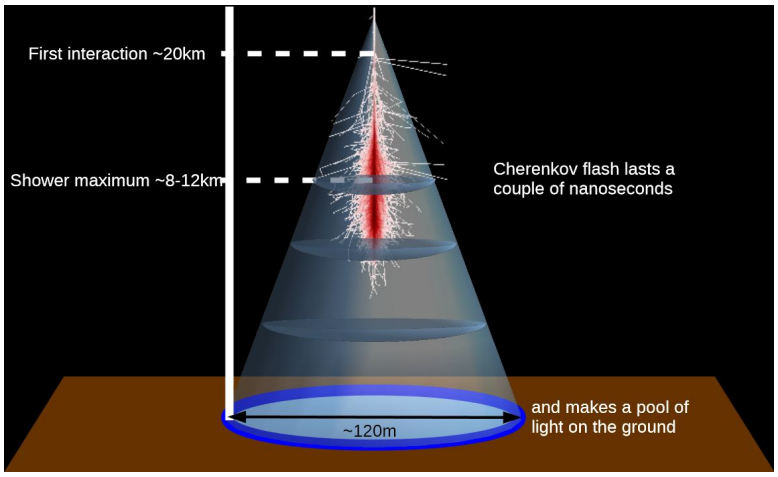

FIGURE 2.20: Schematic view of a Cherenkov flash caused by a gamma ray (www.hermanusastronomy.co.za).

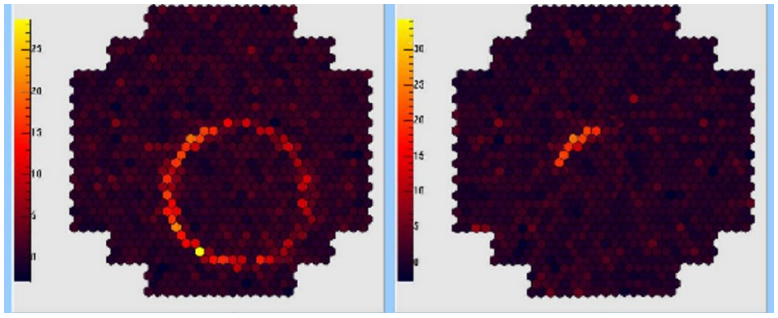

FIGURE 2.21: Different shower patterns caused by high-energy muons. From Völk and Bernlöhr (2009).

"see" the air shower indirectly. The images seen by the telescope reveal the track of the air shower, which points back to the celestial body where the gamma ray originated. The intensity of the image can be used to calculate the energy of the incident gamma ray and the shape of the shower can be used to reject showers caused by other particles, e.g., cosmic rays.

Figure 2.21 shows an example of the observed images caused by high-energy muons. The muon rings play a key part in the calibration of the photomultiplier tubes (PMTs) of the cameras of the telescopes (Chalme-Calvet et al., 2014). Gaug et al. (2019) adds that the analysis of the images produced by muons in an ACT provides a powerful and precise method to calibrate the ACT's optical throughput, monitor its optical PSF as well as yield a good method to continuously monitor the flat-fielding of the camera.

The ACT does not observe the incident gamma ray directly, but rather the Cherenkov radiation created by the air shower. This induces a difficulty in precisely determining the direction of the original gamma ray. Stereoscopic observations by multiple telescopes are therefore used to reconstruct the direction of the incident gamma ray. Figure 2.22 shows a typical gamma-ray shower as seen by the H.E.S.S. telescope array.

2.4.1.2 The H.E.S.S. Array

The H.E.S.S. experiment consists of an array of four 13-m ACTs (H.E.S.S. I) and one 28-m ACT (H.E.S.S. II) located in the Khomas Highland in Namibia. H.E.S.S. started operations in 2003 (CT1-4), with H.E.S.S. II (CT5) seeing first light at 0:43 a.m. on 26 July 2012, making it the first and currently only hybrid ACT array in the world. For full details of the array see Giebels et al. (2013), De Naurois and Mazin (2015), De Naurois (2019).

In the recent past the four 13-m telescopes have undergone maintenance where the 380 mirrors on each telescope have been recoated over a timespan of 2 years, increasing the optical efficiency. To further improve the array, with emphasis on the hybrid array performance, the cameras of the four 13-m telescopes underwent a substantial upgrade in 2015/16. This was done to lower the trigger threshold for the smaller telescope in order to trigger with the larger CT5 telescope. These upgrades, together with hardware upgrades to the IT infrastructure and the computer cluster, were meant to make the whole system failure-proof for the foreseeable future. Furthermore, De Naurois (2019) mentions that the future of the H.E.S.S. experiment is bright with key science topics ranging from deep observation (>100 h) of known sources to observations in the field of time-domain multi-wavelength/multi-messenger astronomy. The future prospects of new lower-energy facilities, e.g., NICER, MeerKAT, Australian Square Kilometre Array Pathfinder (ASKAP) and Murchison Widefield Array (MWA), also open new possibilities for synergetic studies.

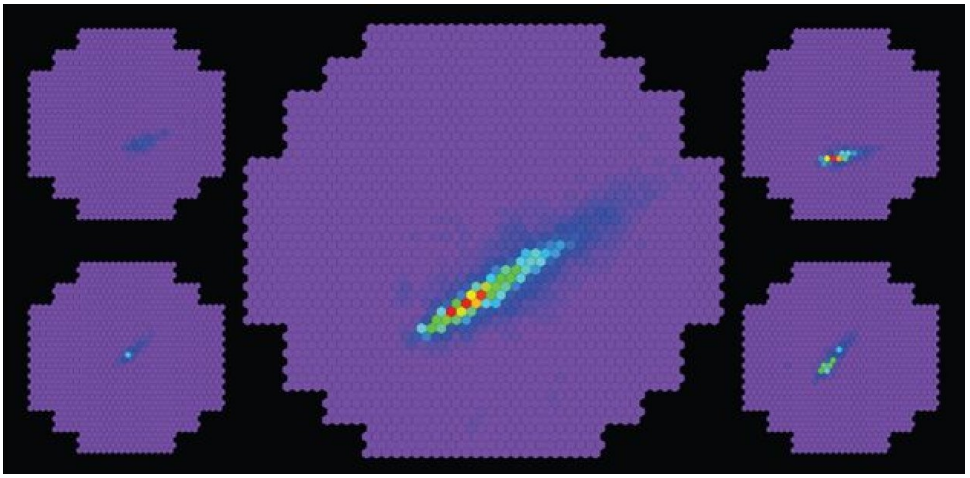

FIGURE 2.22: Typical gamma-ray shower seen by the H.E.S.S. telescope array. From Hinton and Starling (2013).

2.4.1.3 The Cherenkov Telescope Array (CTA)

Within the current scope of ACTs, no new facilities have been built in the last decade. From observations with the current pool of ACTs it is clear that we have but discovered the tip of the iceberg when it comes to VHE sources. We thus need an array of Cherenkov telescopes that will provide sharper views of the particle shower mentioned in Section 2.4.1 as well as use more modern equipment to have a wider field of view as well as a higher energy and angular resolution. This is where CTA comes into the picture. The CTA is the biggest and currently the only gamma-ray observatory planned for the next decade and beyond (Ong et al., 2019).

The CTA will consist of two different arrays of imaging ACTs. One array, the smaller of the two (CTA north), will be situated in the northern hemisphere and will be built on the island La Palma in Spain at an altitude of 2 200 m (Ong et al., 2019). CTA-North will be composed of 4 LSTs (Large-Sized Telescopes with mirror diameters of 23 m) and 15 MSTs (Medium-Sized Telescopes with mirror diameters of 9-12 m), covering an area of ~ 5 km^2. The larger array (CTA-South) will be built at an altitude of 2 100 m in the Atacama Desert of Chile. CTA-South will consist of 4 LSTs, 25 MSTs, and 70 SSTs (Small-Sized Telescopes with mirror diameters of ~ 4 m). Figure 2.23 shows the proposed layouts of both the northern site in the right-hand panel and the southern site in the left-hand panel. Since the northern site is situated on the same premises as the current MAGIC telescopes, these are also indicated by the open red circles.

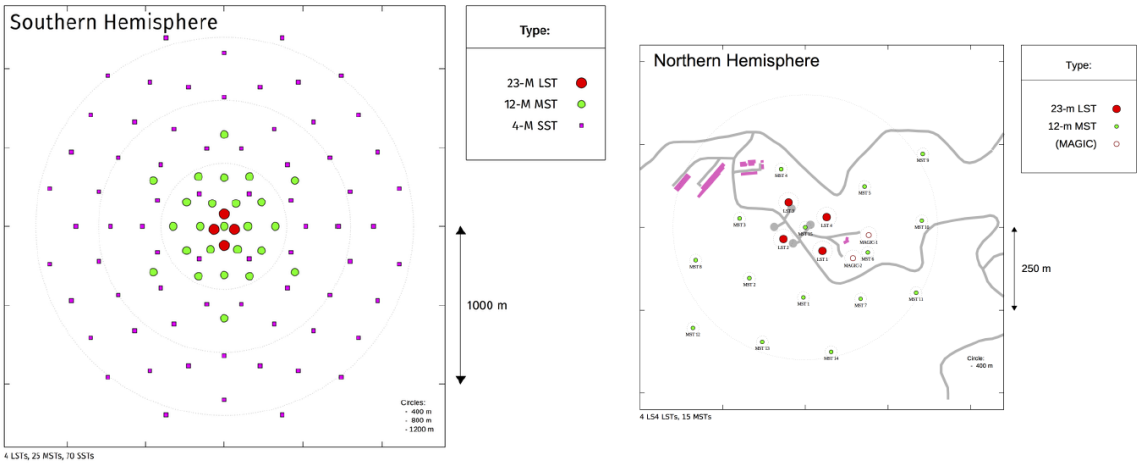

FIGURE 2.23: Proposed layouts of the CTA-South (*left*), and CTA-North (*right*) sites (Ong et al., 2019).

The current status of the project is that the site hosting agreements have been signed for both CTA-North and CTA-South and site preparations have begun on both sites. The first prototype has already been built at the CTA-North site and the current plans

are to have the first pre-production telescopes on site by 2021 for CTA-North and by 2022 for CTA-South. All construction should be completed by 2025.

The key science topics for CTA according to Acharya et al. (2019) can be divided into three main categories. The first of these are "Understanding the Origin and Role of Relativistic Cosmic Particles" that mainly focuses on the acceleration sites and mechanisms of relativistic particles. The second topic is "Probing Extreme Environments" that consists of the study of neutron stars, black holes, relativistic jets, winds and explosions. This is also the theme that I am most interested in, as this includes PWNe. The third topic is "Exploring Frontiers in Physics" and involves the study of dark matter, axion-like particles and quantum gravity.

De Oña-Wilhelmi et al. (2013) mention that the CTA project will have a factor of 5 to 10 improvement in sensitivity above 0.1 TeV compared to current ACTs. This, together with an enhanced energy and angular resolution, will be key factors for the discovery of PWNe as well as identifying unknown sources in the near future. Relevant enhancements and capabilities of the CTA include:

- Resolving current unresolved sources. This is a possibility due to the proposed $< 3'$ angular resolution of CTA.
- The improved energy range of CTA will allow us to understand cooling effects in PWNe in more detail as well as enable us to resolve internal structures in PWNe. This could help disentangle the synchrotron and adiabatic losses.
- The improved angular resolution could also help to distinguish between the radiation that originates from the PWN vs. that from compact SNR.
- The detection of PWNe will be improved since the detection sensitivity of extended sources with CTA scales as $1/d$, where d is the distance to the source. This will allow detections of sources up to 50 kpc away and also allow a homogeneous sampling of PWNe in the Galaxy.
- PWN modelling will benefit from these improved observations that will provide better estimations for magnetic field, electron population, spectral characteristics, etc.

Given the expectations listed above, the CTA experiment will be one of the most powerful tools for studying many astrophysical phenomena, including PWNe studies, for the foreseeable future.

2.4.2 The *Fermi* Gamma-Ray Space Telescope

The *Fermi* Gamma-Ray Space Telescope (FGST), formerly known as the Gamma-ray Large Area Space Telescope (GLAST), is currently one of the few observatories observing the Universe in the GeV energy band and was launched on 11 June 2008 (Atwood et al., 2009). The FGST consists of two main experiments. The first of these are the *Fermi* Large Area Telescope (LAT). The second experiment on board FGST is the Gamma-Ray Burst Monitor (GBM; Meegan et al. 2009). The GBM detects gamma rays in the energy range 8 keV−40 MeV over the entire unocculted sky. The GBM will not be discussed in more detail here. Figure 2.24 shows a schematic diagram of the FGST; for more details, see, e.g., Atwood et al. (2009), Meegan et al. (2009), Michelson et al. (2010).

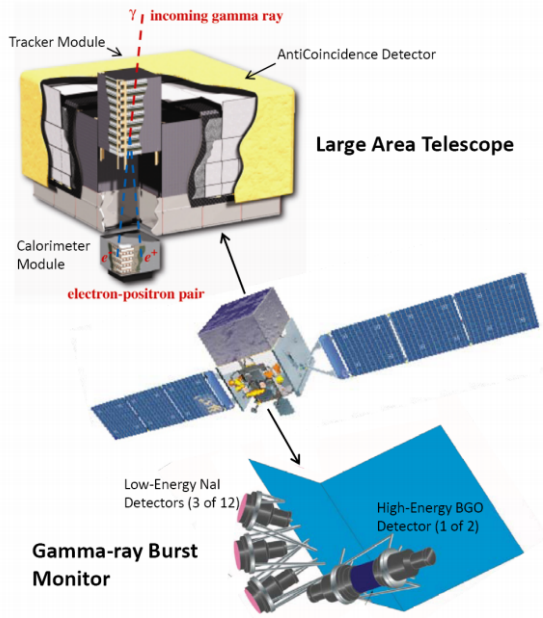

FIGURE 2.24: The *Fermi* Space Gamma-Ray Telescope showing the two experiments on board the telescope, with the LAT in the top part of the image and the GBM in the bottom part of the image (Michelson et al., 2010).

The *Fermi*-LAT telescope was designed to observe the directions, energies and arrival times of gamma rays from wide FOV, observing 20% of the unocculted sky at any time, with a large collection area (9 500 cm^2) as well as excellent single-photon angular resolution. The operational energy range for *Fermi*-LAT is 20 MeV−300 GeV. This energy range makes observing PWNe difficult due to the overwhelming radiation from the central pulsar in this energy range, as mentioned in Section 2.3.3.4.

2.4.3 All-sky Medium Energy Gamma-ray Observatory (AMEGO)

In the first part of Section 2.4 I discussed the current observatories that enable us to observe the Universe in primarily the GeV and TeV energy bands. The medium-energy gamma-ray band is, however, still a very unexplored energy range. This gap in the current observational energy range is one of the key motivations behind the development of AMEGO (McEnery et al., 2019). It will be a key project that adds to the current observatories with respect to multi-messenger astronomy, as objects or events such as neutron star mergers, SNe, PWNe and flaring active galactic nuclei all radiate a broadband spectrum.

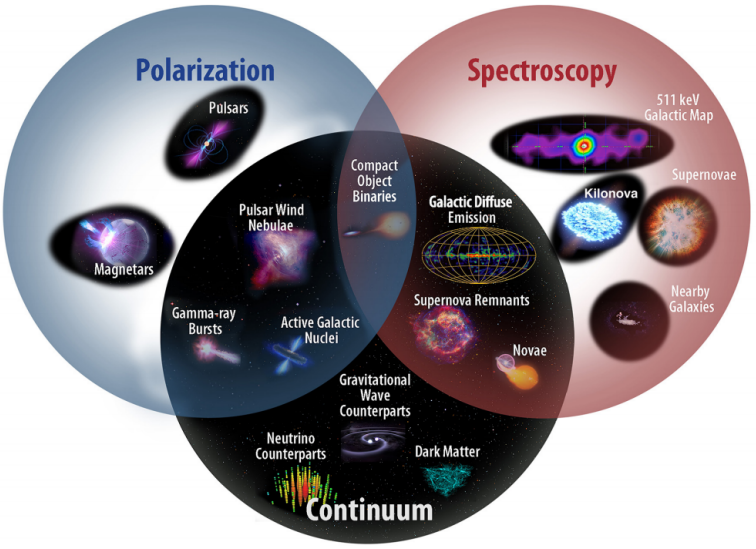

FIGURE 2.25: Schematic of the capabilities of the future AMEGO space telescope. (McEnery et al., 2019).

The AMEGO Space Telescope will be a probe-class mission that will cover the energy range from 200 keV to over 10 GeV and will have an order-of-magnitude increase in sensitivity when compared to current and past missions. The AMEGO mission will be similar in design to the *Fermi*-LAT telescope, but will be optimised to have excellent flux sensitivity, be able to observe over a larger energy range (extending down to lower energies) and have a large FOV. The FOV of AMEGO will be similar to that of *Fermi*-LAT in that 20% of the unocculted sky will be observed at any single time. Figure 2.25 shows how AMEGO will add to our current knowledge of the Universe by using three main techniques: *(1)* The wide FOV of the telescope and broad energy range will allow for improved time-domain and multi-messenger astrophysics that will allow for synergies with observations from other observatories; *(2)* AMEGO will be able to observe polarisation at these energies that will allow it to probe the magnetic field environments in jets as well as the magnetospheres and winds from compact objects (e.g., PWNe); *(3)* Nuclear line spectroscopy will be an advantage as it creates the possibility of observing

element formation in dynamic environments. For more information on the AMEGO mission, see McEnery et al. (2019).

2.4.4 X-Ray Observatories

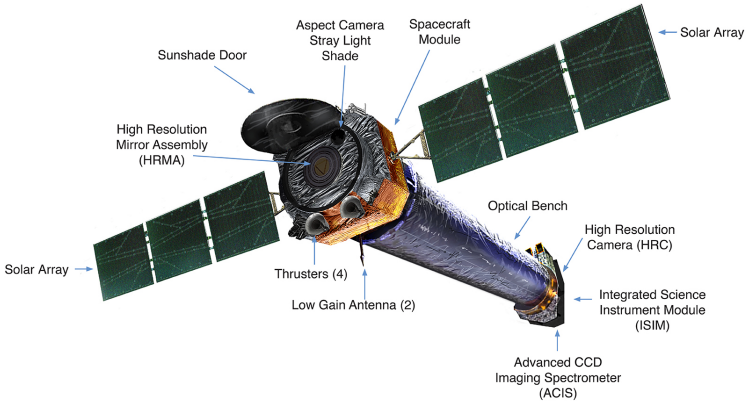

FIGURE 2.26: Artists representation of the *Chandra* X-ray space telescope and its components[a].

[a]https://www.nasa.gov/mission_pages/chandra/spacecraft/index.html

X-ray telescopes are specially designed to detect X-ray emission from sources such as exploded stars, clusters of galaxies, and matter around black holes, which allows them to be an integral part of PWNe studies. Therefore a short section here is dedicated to the *Chandra* X-ray space telescope. Other missions include *XMM*-Newton (Schartel et al., 2017) and *INTEGRAL* (Teegarden and Sturner, 1999).

The *Chandra* X-ray space telescope is the first and currently the only X-ray observatory that can achieve sub-arcsecond resolution, making this one of the most powerful instruments able to observe small sources and resolve them spatially (Zhao, 2018). The X-ray telescope focuses the X rays and allows for the analysis of the number, position, energy and time of arrival of the incident photon. This observatory also has capabilities for doing spectroscopy.

The future of X-ray observations of PWNe will move beyond spectral observations into the polarimetry regime. Bucciantini (2018) mentions that SNRs and PWNe are among the most significant sources of non-thermal X-rays in the sky, making them prime candidates for X-ray polarimetry. Currently the only statistically secure measurement of X-ray polarisation in a cosmic source is that of the Crab Nebula from over 40 years ago (Weisskopf et al., 1976). The future Imaging X-ray Polarimetry Explorer (IXPE) is set to launch in 2021 and will be the first X-ray astronomy mission dedicated to polarimetry.

Figure 2.27 shows an artist's representation of the IXPE, see O'Dell et al. (2019) for more details.

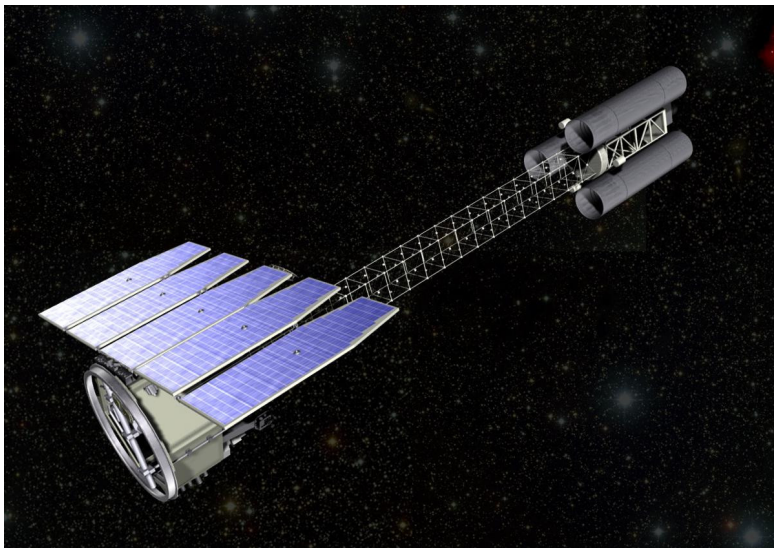

FIGURE 2.27: Artist's representation of the future Imaging X-ray Polarimetry Explorer, commonly known as the IXPE space telescope and its components[a].

[a]https://ixpe.msfc.nasa.gov/about/index.html.

Figure 2.28 illustrates the possibilities of the future IXPE space telescope to constrain the magnetic structure of the Crab Nebula. A toy model (by N. Bucciantini) is used to describe the morphology of the magnetic field with good accuracy and to predict the expected polarisation signatures. The future prospects of IXPE would represent a step forward in our knowledge of the physics of PWNe by additionally constraining the plasma dynamics inside young PWNe, verifying if the relative orientation between rotational and magnetic axes of pulsars correlates with the morphology of PWNe. The IXPE will also allow scrutiny of recent MHD models that attempt to solve the sigma problem (de Oña Wilhelmi et al., 2017).

2.4.5 The Square Kilometre Array (SKA)

It is possible to observe the Universe, including PWNe, at the lowest part of the electromagnetic spectrum in radio waves. SKA is an international effort to build the world's largest radio telescope[2], with a collecting area of over a square kilometre (one million square metres).

The SKA Project will be a giant radio telescope operating in the centimetre-metre wavelengths, with an increase in sensitivity of spectral line observations of $50 - 100$

[2]https://www.skatelescope.org/the-ska-project/

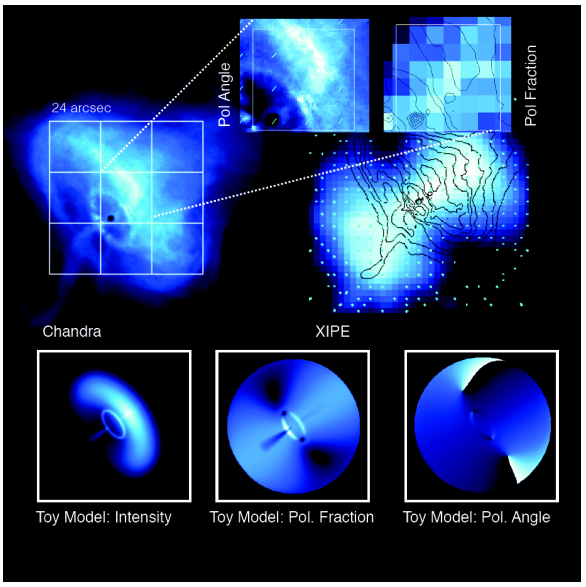

FIGURE 2.28: Crab Nebula simulations as seen by IXPE in 0.2 ksec with a toy model to mimic the *Chandra* image for a given polarisation.

times that of any present radio telescope and it will be 1000 times more sensitive for continuum observations. This instrument will have an angular resolution of up to 0.01 arcsec at a wavelength of 21 cm / 1.4 GHz (Combes, 2015). The construction of the Array will take place in phases:

- 2018 – 2021: Construction of SKA1 (10% of the full telescope).
- 2019 – 2020: Early science begins.
- 2022 – 2025: Construction of SKA2 (the completed array).
- SKA will then be operational for 50 years.

Gelfand et al. (2015) summarises the advantages that the SKA Project will have for PWN studies in great detail. I will summarise those here.

As mentioned earlier, the SKA Project will have a huge increase in sensitivity compared to current radio telescopes. This will result in the measurement of morphology, spectrum, and polarisation properties of more than a hundred PWNe. Currently we only have this type of observations for $\sim$ 10 PWNe. Another advantage of the SKA Project is that currently $\sim 40 - 50\%$ of the known PWNe have associated pulsars. This is mainly due to the beaming of the pulsars' radiation that prevents their detection, but could also be as a result of the limitations of our current observatories as well as high dispersion and scattering timescales of pulsars on the other side of the Milky Way. With SKA some of these effects can be overcome and we should be able to detect many of these pulsars that power the PWNe. Other PWN constituents that current observatories struggle to

observe are the "wisps" near the termination shock that vary on short timescales. These features are only a few arcseconds in size and with the higher frequencies and superior angular resolution of the SKA telescope, these will be within the scope of possibilities.

Currently only about 10% of young pulsars show signs of PWN activity around them. It is, however, believed that all pulsars should power some form of PWN. According to Gaensler et al. (1998) this could be hidden by the bright continuum radiation from the pulsar. They proposed that a technique called "gating" be used to observe some of these pulsars (similar to that used in Section 2.3.3.4). This technique images the region of the pulsar during its "off" cycle and therefore it should be able to observe the faint radio PWN in the pulsar's region. Due to the possibility of measuring low surface brightnesses, this is within the realm of possibilities. This possibility to measure low surface brightnesses also empowers the SKA to observe the larger-scale SNRs around the PWNe. This is not a possibility for current telescopes as they do not have the short baselines needed to observe on these angular scales, and single-dish observations do not have the required sensitivity (Gelfand et al., 2015). The last very important aspect of the SKA Project with respect to PWNe is the possibility of measuring polarised intensity and direction at multiple frequencies that will allow for mapping of the magnetic field in these PWN systems.

2.5 Summary

This chapter surveyed our current knowledge of PWNe. I discussed the origins of a PWN as the result of an SN explosion and pulsars as the powerhouses at the core of these systems. I continued by discussing the characteristics of PWNe, how they evolve and how these sources behave in different energy bands. From this we saw that PWNe are true multi-wavelength sources. The second part of this chapter was dedicated to describing the key observatories from TeV energies down to radio energies that observe and will observe PWNe in the near future.

In the next chapter the physics of the transport of particles inside a PWN will be discussed as well as how these particles radiate the broadband spectrum we observe.

Chapter 3

Particle Transport, Evolution and Radiation in Pulsar Wind Nebulae

This Chapter introduces the reader to the mathematical description of how leptons traverse the PWN as well as how these particles radiate some of their energy as a broadband electromagnetic spectrum. I will introduce the Fokker-Plack transport equation in Section 3.1, and then discuss the various physical phenomena that govern each term of this equation in sections 3.1.1 to 3.1.3. Finally, I will discuss how these particles radiate and lose energy in Section 3.2.

3.1 The Transport of Leptons in a PWN

At the core of describing the motion of the particles lies a Fokker-Planck-type transport equation that includes diffusion, convection, energy losses (radiative and adiabatic), as well as a particle source term. The transport equation used in this study has the following form (Moraal, 2013):

$$\frac{\partial f}{\partial t} = -\nabla \cdot \mathbf{S} + \frac{1}{p^2}\frac{\partial}{\partial p}\left(p^2 \langle \dot{p} \rangle_{\rm tot} f\right) + Q(\mathbf{r}, \mathbf{p}, t), \tag{3.1}$$

with f the distribution function (number of particles per six-dimensional unit phase-space volume, spanning three spatial and three momentum directions), $Q(\mathbf{r}, \mathbf{p}, t)$ the particle injection spectrum (per unit phase space volume and time), r the radial dimension, p the particle momentum, and $\langle \dot{p} \rangle_{\rm tot}$ the total rate of change of p. The term $\nabla \cdot \mathbf{S} = \nabla \cdot (\mathbf{V}f - \underline{\mathbf{K}}\nabla f)$ describes the general movement of particles in the PWN, with

$\mathbf{V}$ the bulk motion of particles, $\underline{\mathbf{K}}$ the diffusion tensor, and $\mathbf{S}$ the streaming density. However, we rewrite Eq. (3.1) in terms of energy and also transform the distribution function to a particle spectrum per unit volume $U_{\rm p}$ as is more customary in some astrophysical applications. Following Moraal (2013), we assume isotropy in momentum space and use the relation $U_{\rm p}(\mathbf{r}, p, t) = 4\pi p^2 f(\mathbf{r}, \mathbf{p}, t)$ (with the units of $U_{\rm p}$ being number of particles per three-dimensional volume per momentum interval) to convert f to a particle spectrum, and $E^2 = p^2c^2 + E_0^2$ to convert Eq. (3.1) from momentum to energy space, with $E_0 = m_{\rm e}c^2$, $m_{\rm e}$ the electron mass, and c the speed of light in vacuum. We also assume that the diffusion is only energy-dependent, $\underline{\mathbf{K}} = \kappa(E_{\rm e})$, with $E_{\rm e}$ the lepton energy. Thus Eq. (3.1) becomes

$$\begin{aligned}\frac{\partial N_{\rm e}}{\partial t} =& -\mathbf{V}\cdot(\nabla N_{\rm e}) + \kappa\nabla^2 N_{\rm e} \\ &+ \frac{1}{3}(\nabla\cdot\mathbf{V})\left(\left[\frac{\partial N_{\rm e}}{\partial \ln E_{\rm e}}\right] - 2N_{\rm e}\right) \\ &+ \frac{\partial}{\partial E}(\dot{E}_{\rm e,tot}N_{\rm e}) + Q(\mathbf{r}, E_{\rm e}, t),\end{aligned} \tag{3.2}$$

with $\dot{E}_{\rm e,tot}$ total energy loss rate, including radiation and adiabatic energy losses. The units of $N_{\rm e} \equiv U_{\rm E}(\mathbf{r}, E_{\rm e}, t)$ is the number of particles per unit energy and volume. See Van Rensburg et al. (2015) and Appendix A for more details regarding the derivation of Equation (4.5).

3.1.1 Injection of Particles

Considering the observed spectra of PWNe, one has to consider what type of spectrum is feasible to inject at the termination shock. In Section 2.3.1, I noted that a two-component lepton spectrum is required to explain the non-thermal emission from a PWN. Each of these components can be described by a power law given by $N_{\rm e} \propto E^{-p}$, with $N_{\rm e}$ the particle number density per energy interval. As mentioned, the first low-energy component responsible for the hard SR radio spectrum and the GeV IC scattering emission component has an index of $p \sim 1-1.6$, while the second high-energy component responsible for the X-ray SR and TeV IC scattering component has an index of $p \sim 2-3$.

Some PWN evolution models (see, e.g., Venter and de Jager 2007, Zhang et al. 2008) use this broken-power-law distribution of the leptons as an injection spectrum into the PWN at the termination shock. They also assume that the transition from the one component to the other is a smooth one, thus having the same intensity at the transition. In contrast, Vorster et al. (2013) assumed that the transition from one component to the next is not necessarily smooth but that the injection spectrum can be modelled by a two-component particle spectrum that has a steep cutoff for the low-energy component

in order to connect to the high-energy component, with each component characterised by a unique conversion efficiency (and thus normalisation). This causes a discontinuity in the particle spectrum but allows them to fit the steep slope of the X-ray data of many PWNe and is thus an observationally motivated injection spectrum.

One may next ponder the origin of these two components as motivated by observations vs. a single power-law spectrum. According to Axford et al. (1977), diffusive shock acceleration leads to a power-law spectrum $N_\mathrm{e} \propto E^{-p}$, with $p = 2$ the maximum value. We can therefore associate the high-energy component of the broken power law with this mechanism. It is, however, not so simple to explain the lower-energy component where $p \sim 1.0 - 1.6$, as indicated by radio measurements. Relativistic MHD shock codes by Summerlin and Baring (2012) showed that it is possible for shocks to reproduce this hard spectrum if particles are subjected to shock drift acceleration. Particle-in-cell simulations by Spitkovsky (2008) also show that acceleration of particles at the termination shock leads to a Maxwellian spectrum with a non-thermal power-law tail. These ideas provide some basis for the assumption of a broken-power-law or two-component injection spectrum.

Considering the previous discussion, I decided to follow Venter and de Jager (2007) and use a broken power law for the particle injection spectrum of the following form:

$$Q(E_\mathrm{e}, t) = \begin{cases} Q_0(t) \left(\frac{E_\mathrm{e}}{E_\mathrm{b}}\right)^{\alpha_1} & E_\mathrm{e,min} \leq E_\mathrm{e} < E_\mathrm{b} \\ Q_0(t) \left(\frac{E_\mathrm{e}}{E_\mathrm{b}}\right)^{\alpha_2} & E_\mathrm{b} < E_\mathrm{e} \leq E_\mathrm{e,max}. \end{cases} \tag{3.3}$$

Here $Q_0(t)$ is the time-dependent normalisation constant, E_b the break energy, α_1 and α_2 are the spectral indices.

3.1.2 Diffusion

According to Chen (1984), diffusion by means of Coulomb collisions has been studied for a long time. The diffusion coefficient κ was thought to have a $1/B^2$ dependence but this result could not be verified in any of the experiments done. In 1946, Bohm gave a semi-empirical formula for the diffusion coefficient in their magnetic arc experiment. Their form of the diffusion coefficient was

$$\kappa = \frac{c}{3e}\frac{E}{B} = D_B. \tag{3.4}$$

Any diffusion process following this law is therefore called Bohm diffusion. There are, however, many different forms of diffusion. Zheng (2011) studied the solutions of the momentum diffusion equation of the particle distribution in a turbulent magnetic field.

If the turbulence is given by a power spectrum of $W(k) \propto k^{-q}$, with k the wave number, the different types of diffusion that they consider is Bohm diffusion ($q = 1$), Kolmogorov diffusion ($q = 5/3$), Kreichnan diffusion ($q = 3/2$), and the hard sphere approximation ($q = 2$). In their paper they show how the diffusion coefficient changes for different forms of the turbulent magnetic field.

We currently do not have a very good idea of how turbulent the magnetic field inside the PWN is, although we have some constraints from the polarised radio spectrum. Due to this uncertainty we do not know what form of diffusion coefficient we have to use and therefore we chose Bohm diffusion as a first approximation. To assume Bohm diffusion is a fairly common practice as it describes diffusion that is perpendicular to the magnetic field. We treat the B-field as predominantly azimuthal (toroidal) as is standard practice, e.g., Kennel and Coroniti (1984a), Schöck et al. (2010), Vorster and Moraal (2014). This assumption is based on several arguments: in this case $\nabla \cdot \mathbf{B} = 0$; at typical PWN scales any dipolar field components have all but died out compared to the toroidal components (given their respective $1/r^3$ vs. $1/r$ decay); and X-ray observations show ubiquitous polar and equatorial outflows supporting an azimuthal structure winding around the pulsar in the equatorial plane. Due to this assumption regarding the magnetic field geometry we are only interested in radial diffusion perpendicular to the magnetic field, which will lead to particles moving from one zone to the next in the PWN.

3.1.3 Convection and Adiabatic Losses

Convection is mass transfer due to the bulk motion of a fluid. This bulk motion of the particles will cause them to lose energy due to the PWN expansion in the form of adiabatic cooling, and the rate at which they lose energy is given by (e.g., Zhang et al., 2008)

$$\dot{E}_{\mathrm{ad}} = \frac{1}{3}(\nabla \cdot \mathbf{V})E_{\mathrm{e}}. \tag{3.5}$$

The B-field and bulk motion are linked by Faraday's law of induction, yielding the following relationship (Kennel and Coroniti, 1984a):

$$VBr = \text{constant} = V_0 B_0 r_0. \tag{3.6}$$

It can be shown that by inserting Eq. (4.14) and Eq. (4.17) into Eq. (3.6), the following relation holds:

$$\alpha_{\mathrm{V}} + \alpha_{\mathrm{B}} = -1. \tag{3.7}$$

We added a spatial dimension to the code and this resulted in the introduction of two new parameters, $\alpha_{\rm B}$ and $\alpha_{\rm V}$. We use the relationship in Eq. (3.7) to reduce the number of free parameters in our model by one. See Section 4.6 for more on this topic.

3.2 Radiation mechanisms

It is thought that IC scattering and SR are the two main mechanisms responsible for radiation from PWNe. The spectral energy distribution (SED) consists of two components, where the low-energy component spanning the radio and X-ray wavelengths is due to SR (Section 3.2.1) and the high-energy component is due to the upscattering of photons to several TeV due to IC scattering (Section 3.2.2). Other radiation mechanisms include Synchrotron self-Compton (SSC) and Bremsstrahlung, but the estimated flux levels of these are relatively negligible for the systems that are modelled in this study and therefore not included here.

3.2.1 Synchrotron radiation

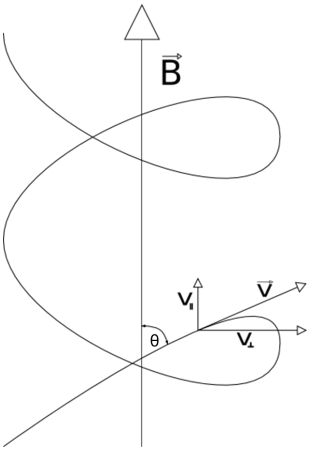

FIGURE 3.1: An electron spiralling around a magnetic field line, illustrating SR. Adapted from Rybicki and Lightman (1979)

In this section, I discuss SR which is responsible for the low-energy spectral component. SR occurs when charged particles (e.g., electrons) spiral around a magnetic field. Figure 3.1 is a schematic representation of an electron with a velocity $\vec{v}$ spiralling around a magnetic field $\vec{B}$ at a pitch angle θ. In the classical, non-relativistic case, a single particle gyrating in a magnetic field will radiate power according to the Larmor formula (Rybicki and Lightman, 1979)

$$P = \frac{2q^2a^2}{3c^3}, \tag{3.8}$$

where a is the acceleration, and q is the particle charge. If the relativistic case is considered and we assume that $dv_{\parallel}/dt = 0$, then the power radiated by an electron is given by

$$P = \frac{2q^2}{3c^3}\gamma^4 \left(\frac{qB}{\gamma m_{\rm e} c}\right)^2 v_{\perp}^2, \tag{3.9}$$

where B is the magnetic field strength, and $v_{\perp}$ the electron's speed perpendicular to the magnetic field. According to Blumenthal and Gould (1970) we can also write the SR energy loss rate as

$$\frac{dE_{\rm SR}}{dt} = -\left(\frac{2r_0^2}{3c}\right)\gamma^2 B^2 v_{\perp}^2, \tag{3.10}$$

where $v_{\perp}^2 = v^2 \sin^2\theta$, $r_0 = e^2/m_{\rm e}c^2$ is the classical electron radius, e is the electron charge, and γ is the electron's Lorentz factor.

Next we need to calculate the radiative power from SR and to do this we rewrite the electron's speed as $\beta_{\perp} c$. Then, by averaging over θ for an isotropic distribution of velocities, we obtain $\langle \beta_{\perp} \rangle = \frac{2}{3}\beta^2$. Thus, we find the total radiated power to be (Rybicki and Lightman, 1979)

$$P_{\rm tot} = \dot{E}_{\rm SR} = \frac{4}{3}\sigma_{\rm T} c \beta^2 \gamma^2 U_{\rm B} \propto E^2 B^2, \tag{3.11}$$

where $U_{\rm B} = B^2/8\pi$ is the magnetic energy density. The expression for $\dot{E}_{\rm SR}$ is similar to $\dot{E}_{\rm IC}$ (the Thomson limit) in Eq. (3.23).

We can now calculate the single-particle spectrum. This spectrum is characterised by a critical frequency near which the spectrum reaches a maximum:

$$\omega_{\rm c} = \frac{3}{2}\gamma^3 \omega_{\rm B} \sin\theta = \frac{3}{2} e \frac{B \sin\theta}{m_{\rm e} c}\gamma^2, \tag{3.12}$$

where $\omega_{\rm B}$ is the gyration frequency of rotation given by

$$\omega_{\rm B} = \frac{eB}{\gamma m_{\rm e} c}. \tag{3.13}$$

The power emitted per angular frequency by a single electron is given by

$$P(\omega) = \frac{\sqrt{3}}{2\pi}\frac{e^3 B \sin\theta}{m_{\rm e} c} F(x), \tag{3.14}$$

where

$$F(x) = x \int_x^{\infty} K_{\frac{5}{3}}(\xi) d\xi, \tag{3.15}$$

with $x \equiv \omega/\omega_c$, and $K_{\frac{5}{3}}$ a modified Bessel function of the second kind of order 5/3. The function $F(x)$ has the following asymptotic forms for small and large values for x:

$$F(x) \sim \frac{4\pi}{\sqrt{3}\Gamma(1/3)} \left(\frac{x}{2}\right)^{1/3}, \qquad x \ll 1, \tag{3.16}$$

$$F(x) \sim \left(\frac{\pi}{2}\right)^{1/2} e^{-x} x^{1/2}, \qquad x \gg 1. \tag{3.17}$$

The spectral maximum occurs at $\omega_{\max} = 0.29\omega_c$ (Longair, 2011).

If the number density $N_e(E_e)$ of electrons in an energy range $(E_e, E_e + dE_e)$, can be expressed as a power law

$$N_e(E_e)dE_e = CE_e^{-p}dE_e, \qquad E_1 < E_e < E_2, \tag{3.18}$$

one can show that the total SR power radiated by these particles is

$$P_{\rm tot}(\omega) \propto \omega^{-(p-1)/2} \propto \omega^s, \tag{3.19}$$

where s the index of the energy spectrum. Thus, the photon spectrum is then similar to IC in Eq. (3.33) and is given by

$$\frac{dN_\gamma}{dE_\gamma} \propto \omega^{-(p+1)/2}. \tag{3.20}$$

3.2.2 Inverse Compton (IC) scattering

In this section the upscattering of "soft" (low-energy) background target photons to high energies when interacting with high-energy electrons is discussed. This process is called IC scattering.

The Thomson limit is valid when

$$\gamma\varepsilon \ll m_e c^2, \tag{3.21}$$

where γ is the electron Lorentz factor, m_e is the mass of the electron, and ε is the soft-photon energy. According to Blumenthal and Gould (1970), the mean energy of the Compton-scattered photon ϵ_1 for an isotropic photon gas is given by

$$\langle\epsilon_1\rangle = \frac{4}{3}\gamma^2\langle\epsilon\rangle, \tag{3.22}$$

where $\langle\epsilon\rangle$ is the mean energy of the soft photons. The total energy loss rate of a single electron is (Rybicki and Lightman, 1979)

$$-\frac{dE_{\rm e}}{dt} = \frac{4}{3}\sigma_{\rm T} c \gamma^2 U_{\rm iso}, \tag{3.23}$$

where $\sigma_{\rm T} = 8\pi r_0^2/3 = 6.65 \times 10^{-25}{\rm cm}^2$ is the Thomson cross section, with r_0 the Thompson scattering length (also known as the classical electron radius), and $U_{\rm iso}$ is the energy density of the isotropic photon field. The general IC scattered photon spectrum per electron is (Blumenthal and Gould, 1970)

$$\frac{dN_{\gamma,\epsilon}}{dt d\epsilon_1} = \frac{\pi r_0^2 c \; n(\epsilon) d\epsilon}{2\gamma^4 \epsilon^2}\left(2\epsilon_1 \ln\frac{\epsilon_\gamma}{4\gamma^2\epsilon} + \epsilon_1 + 4\gamma^2\epsilon - \frac{\epsilon_1^2}{2\gamma^2\epsilon}\right), \tag{3.24}$$

where $n(\epsilon)$ is the photon number density associated with a blackbody distribution.

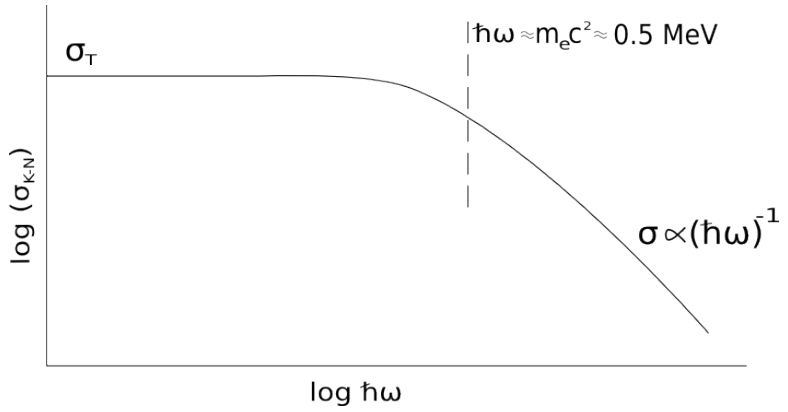

FIGURE 3.2: A schematic diagram showing the dependence of the IC cross-section on soft-photon energy. Arbitrary units are used. Adapted from Longair (2011).

The Klein-Nishina (K-N) limit is valid when

$$\gamma\varepsilon \gg m_{\rm e}c^2, \tag{3.25}$$

and the scattered photon energy now becomes

$$\epsilon_1 \sim \gamma m_{\rm e} c^2. \tag{3.26}$$

Figure 3.2 shows how the Thomson cross section transitions to the K-N cross section as the soft-photon energy increases. This K-N cross section is given by (Rybicki and Lightman, 1979)

$$\sigma = \sigma_{\rm T}\frac{3}{4}\left[\frac{1+x}{x^3}\left\{\frac{2x(1+x)}{1+2x} - \ln(1+2x)\right\} + \frac{1}{2x}\ln(1+2x) - \frac{1+3x}{(1+2x)^2}\right], \tag{3.27}$$

with $x = \gamma\hbar\omega/m_e c^2$. The single-electron energy loss rate in the extreme K-N limit for a blackbody photon distribution of temperature T is given by (Blumenthal and Gould, 1970)

$$-\frac{dE_e}{dt} = \frac{1}{6}\pi r_e^2 \frac{(m_e c\, k_B T)^2}{\hbar^3}\left[\ln\left(\frac{4\gamma\, k_B T}{m_e c^2}\right) - 1.98\right], \tag{3.28}$$

where k_B is the Boltzmann constant. The general equation for the upscattered photon spectrum per electron is given by (Jones, 1968)

$$\frac{dN_{\gamma,\epsilon}}{dt dE_\gamma} = \frac{2\pi r_0^2 m_e c^3\, n(\epsilon) d\epsilon}{\gamma\epsilon}\left[2q\ln q' + (1+2q')(1-q') + \frac{1}{2}\frac{(\Gamma_e q')^2}{1+\Gamma_e q'}(1-q')\right], \tag{3.29}$$

where $E_\gamma = \epsilon_1/\gamma m_e c^2$, Γ_e is the dimensionless parameter

$$\Gamma_e = \frac{4\gamma}{m_e c^2}, \tag{3.30}$$

and

$$q' = \frac{E_\gamma}{\Gamma_e(1-E_\gamma)}. \tag{3.31}$$

The total Compton spectrum can thus be calculated by integrating the production rate in Eq. (3.29) over the soft-photon energy ϵ and electron Lorentz factor γ:

$$\left(\frac{dN}{d\epsilon_1}\right)_{tot} = \iint N_e \left(\frac{dN_{\gamma,\epsilon}}{dt d\epsilon_1}\right) d\gamma d\epsilon, \tag{3.32}$$

with $dN_e = N_e(\gamma)d\gamma$ the differential number of electrons per γ interval. If we assume that the electron energy distribution is a power law, $N_e \propto \gamma^{-p}$, interacting with a blackbody soft-photon distribution, then it follows that (Blumenthal and Gould, 1970)

$$\left(\frac{dN}{d\epsilon_1}\right)_{tot} \propto \epsilon_1^{-(p+1)/2} \quad - \text{Thomson Limit}, \tag{3.33}$$

$$\left(\frac{dN}{d\epsilon_1}\right)_{tot} \propto \epsilon_1^{-(p+1)} \quad - \text{Extreme K-N Limit}. \tag{3.34}$$

Something to note is that the expression in Eq. (3.33) is the same as for SR shown in Eq. (3.20), but the spectrum is much softer in the extreme K-N regime.

3.3 Summary

This Chapter has been dedicated to describing the mechanisms involved in PWNe. I have discussed how the particles will move inside the PWN by relating how the particles are injected from the pulsar wind into the system, how these particles will move due

to diffusion and convection, and how these particles will radiate a broadband electromagnetic spectrum. This Chapter provided a good basis for the next one where I will discuss the implementation of our spatio-temporal PWN code.

Chapter 4

Implementation of a Spatio-Temporal Leptonic Model

In this chapter, I describe the development and implementation of a multi-zone, time-dependent code that models the transport and radiation of particles through a PWN. The code was developed as an improvement to the code of Venter and de Jager (2007). During the development I was responsible for developing and introducing a new transport equation and by using the radiation code from the globular cluster model of Kopp et al. (2013), I was able to complete the new PWN model.

I discuss the development of the code by introducing the current modelling landscape to indicate the void that existed in this landscape and then describe the development of our model. The physics discussed in Chapter 3 will be briefly referenced here, with the implementation of the code being the main focus. The majority of this chapter has been published in Van Rensburg et al. (2018).

4.1 Current Modelling Landscape for PWNe

The current modelling landscape can be summed up using three main categories, each with its own advantages and shortcomings. The first category encompasses magneto-hydrodynamic (MHD) codes (e.g., Bucciantini, 2014, Porth et al., 2014, Slane, 2017, Olmi and Bucciantini, 2019) that are able to model the morphology (e.g., particle densities, bulk flows and magnetic profiles) of PWNe in great detail, but cannot produce radiation spectra from first principles due to the fluid nature of these codes. Conversely, emission codes (mostly leptonic; see, e.g., Venter and de Jager, 2007, Zhang et al., 2008, Tanaka and Takahara, 2011, Martín et al., 2012, Martin et al., 2014, Torres

et al., 2014), are able to reproduce the radiation spectra reasonably well, but fail to model the PWN morphology as most of these codes model the source as a single sphere (0D) with parameters describing the PWN environment averaged over space. The third category encompasses hybrid models that combine either MHD or dynamical modelling results with those of an emission code to model both the morphology and radiation spectra. For example, Porth et al. (2016) use a steady-state transport code to predict the spatial emission properties of PWNe, but neglect the dynamical evolution of these sources. Also in this category are works where authors use semi-analytic expressions or numerical solutions to study the dynamical and radiation evolution of a PWNe inside its surrounding supernova remnants (see, e.g., Gelfand et al. 2009) and references therein. While the emission codes mentioned above typically model young PWNe during their free-expansion phase, Martín et al. (2016), Torres and Lin (2018), Torres et al. (2019) improve on this by considering the pressure produced by the particles and magnetic field inside the PWN, thus allowing them to model the interaction of the PWN and the supernova remnant (SNR) via the reverse shock during the reverberation phase of the PWN's evolution. Using such a model, Zhu et al. (2018) performed a population study including 18 PWNe, ranging from young to older PWNe, to discover relationships between model parameters. See Gelfand (2017) for a recent review of this class of models.

Given the characteristics of the above model categories, we therefore perceived a void in the current modelling landscape that has not been investigated substantially – self-consistent modelling of both the spatial (in 1D, 2D or 3D) and temporal (from pulsar birth to present) aspects of the PWN spectrum.

4.2 Model Geometry

We make the simplifying assumption that the geometrical structure of the PWN may be modelled as a set of concentric spheres (zones) into which particles are injected, allowed to diffuse and undergo energy losses (see Figure 4.1). The white star at the centre of Figure 4.1 is the location of the pulsar in the model. The red region in the middle of the modelling geometry is not modelled with the edge of the red sphere, at radius $r_0 = r_{\rm ts}$, defined as the termination shock where the particles are accelerated and injected into the PWN. This is treated as the inner boundary of the system.

Another assumption is that particle transport is spherically symmetric and thus the only changes in the particle spectrum will be in the radial direction (apart from changes in the particle energy with time). The model therefore consists of three dimensions in which the transport equation is solved: the spatial or radial dimension, the lepton energy dimension, and the time dimension.

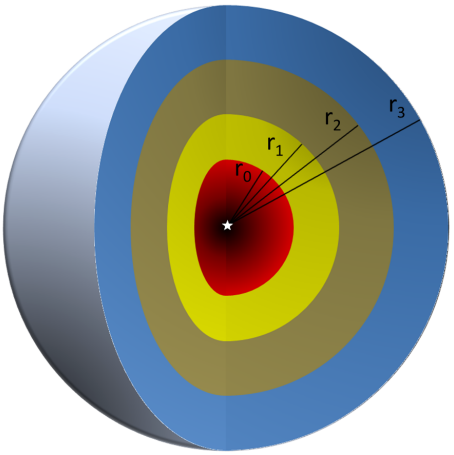

FIGURE 4.1: Three-dimensional illustration of the concentric spheres of the PWN model setup. The white star indicates the position of the pulsar at the centre of the system.

The radial dimension is divided into linear bins and is a static grid into which the PWN is allowed to expand. Therefore, there is a minimum radius r_0 at the termination shock, and a maximum radius $r_{\rm max}$ chosen to be much larger than the radius of the PWN $R_{\rm PWN}(t)$. Converse to Torres et al. (2014) who prescribe an $R_{\rm PWN}(t)$, in our model, this radius will be calculated later from the predicted morphology of the PWN. The radial bin size is calculated using

$$\Delta r = (r_{\rm max} - r_0)\,/(N-1), \tag{4.1}$$

with N the number of bins and Δr the bin size in the radial dimension. Typical values used here are $r_0 = 0.1$ pc and $r_{\rm max} = 16$ pc, and the k^{th} radius is given by $r_k = r_{\rm min} + (k-1)dr$, for $k = 1, 2, \ldots, N$.

The lepton energy dimension is divided into logarithmic bins. The way this is done is to choose a minimum ($E_{\rm min} = 1.0 \times 10^{-7}$ erg) and maximum ($E_{\rm max} = 1.0 \times 10^{4}$ erg) value for the energies, with the break in the spectrum at $E_{\rm b} \sim 0.1$ erg, and then calculate the size of every energy bin. This is given by

$$(\Delta E)_i = \delta E_i, \tag{4.2}$$

with

$$\delta = \frac{1}{M-1} \ln\left(\frac{E_{\rm max}}{E_{\rm min}}\right), \tag{4.3}$$

as discussed in Appendix A.2. We can also calculate the i^{th} energy bin using $E_i = E_{\rm min} e^{i\delta}$, for $i = 0, 1, \ldots, M-1$.

The time step is chosen to be dynamical and starts at $t = 0$, the time of birth of the PWN.

It is allowed to reach the known age of the specific PWN I modelled by incrementing the time by a step dt. The dynamical time step is calculated for each iteration of the code to optimise the run time of the code. To keep the code stable, the time step has to be much smaller than the energy-loss timescale and the diffusion timescale. Therefore, for each time iteration in the code, the energy-loss timescale and the diffusion timescale are calculated and the time step is then set to a small fraction of the smaller of these two timescales.

4.3 The Transport Equation

In Chapter 3 I solve a Fokker-Planck-type equation that includes diffusion, convection, energy losses (radiative and adiabatic), as well as a particle source term initially in the following form:

$$\frac{\partial f}{\partial t} = -\nabla \cdot \mathbf{S} + \frac{1}{p^2}\frac{\partial}{\partial p}\left(p^2 \langle \dot{p} \rangle_{\rm tot} f\right) + Q(\mathbf{r}, \mathbf{p}, t). \tag{4.4}$$

We rewrite this equation as

$$\begin{aligned}\frac{\partial N_{\rm e}}{\partial t} =& - \mathbf{V} \cdot (\nabla N_{\rm e}) + \kappa \nabla^2 N_{\rm e} \\ &+ \frac{1}{3}(\nabla \cdot \mathbf{V})\left(\left[\frac{\partial N_{\rm e}}{\partial \ln E_{\rm e}}\right] - 2N_{\rm e}\right) \\ &+ \frac{\partial}{\partial E}(\dot{E}_{\rm e,tot} N_{\rm e}) + Q(\mathbf{r}, E_{\rm e}, t).\end{aligned} \tag{4.5}$$

The full derivation of this can be seen in Appendix A.1. This equation contains, following our assumptions, all the necessary math to model the motion of the particles in the PWN in space, time and energy as mentioned in Chapter 3. Here I will discuss how each of the terms in this equation is implemented and then how the equation as a whole is solved.

4.4 The Particle Injection Spectrum

Following Venter and de Jager (2007), we use a broken power law for the particle injection spectrum as mentioned in Section 3.1.1

$$Q(E_{\rm e}, t) = \begin{cases} Q_0(t)\left(\frac{E_{\rm e}}{E_{\rm b}}\right)^{\alpha_1} & E_{\rm e,min} \leq E_{\rm e} < E_{\rm b} \\ Q_0(t)\left(\frac{E_{\rm e}}{E_{\rm b}}\right)^{\alpha_2} & E_{\rm b} < E_{\rm e} \leq E_{\rm e,max}. \end{cases} \tag{4.6}$$

Here $Q_0(t)$ is the time-dependent normalisation constant, $E_{\rm b}$ the break energy, α_1 and α_2 the spectral indices. To obtain Q_0 we use the following form for the spin-down

luminosity of the pulsar: $L(t) = L_0/\left(1 + t/\tau_0\right)^2$ assuming a braking index of $n = 3$ (e.g., Reynolds and Chevalier, 1984). The birth characteristic age is $\tau_0 = P_0/(n-1)\dot{P}_0$, t the time, L_0 the initial spin-down luminosity, and P_0 and $\dot{P}_0$ are the pulsar's initial period and time derivative of the period. From the current value of P and $\dot{P}$, we first calculate $\tau_c = P/(n-1)\dot{P}$, which is the characteristic age of the pulsar (Gaensler and Slane, 2006). Next we use $\tau_0 = \tau_c - t_{age}$, with t_{age} the age of the PWN. From this follows $L(t)$ for constant n, with t_{age} the only free parameter (see Appendix A.3). To solve for Q_0, I set

$$\epsilon L(t) = \int_{E_{min}}^{E_b} Q E_e dE_e + \int_{E_b}^{E_{max}} Q E_e dE_e, \tag{4.7}$$

with $\epsilon = 1/(1+\sigma)$ the constant conversion efficiency of the spin-down luminosity to particle power, and σ the ratio of electromagnetic to particle energy density as mentioned in Section 2.2. For the normalisation of $Q_0(t)$, see Appendix A.4.

4.5 Energy Losses

Energy losses in our model are as a result of two main processes – radiative and adiabatic energy losses. For radiative energy losses we incorporated SR and IC scattering, similar to calculations done by Kopp et al. (2013) in their globular cluster model. We neglect synchrotron self-Compton (SSC) and Bremsstrahlung as the energy losses due to the fact that these two effects are orders of magnitude smaller than SR and IC scattering for the sources considered in this study. See Section 3.2 for more on the radiation mechanisms. The SR losses are given by (Blumenthal and Gould, 1970)

$$\left(\frac{dE_e}{dt}\right)_{SR} = -\frac{\sigma_T c}{6\pi E_0^2} E_e^2 B_\perp^2, \tag{4.8}$$

with $\sigma_T = (8\pi/3) r_e^2 = 6.65 \times 10^{-25}\text{cm}^2$ the Thomson cross section, $B_\perp$ the average perpendicular PWN B-field at a certain time and radius, and $r_e = e^2/m_e c^2$ the classical electron radius. The IC scattering energy loss rate of leptons scattering blackbody (BB) photons is given by

$$\left(\frac{dE_e}{dt}\right)_{IC} = \frac{g_{IC}}{E_e^2} \sum_{l=1}^{3} \iint n_{\varepsilon,l}(r, \varepsilon, T_l) \times \frac{E_\gamma}{\varepsilon} \zeta(E_e, E_\gamma, \varepsilon) d\varepsilon dE_\gamma, \tag{4.9}$$

with $n_{\varepsilon,l}(r, \varepsilon, T_l)$ the BB photon number density of the l^{th} BB component, $g_{IC} = 2\pi e^4 c$, ε the soft-photon energy, T_l the BB temperature, E_γ the TeV upscattered photon energy,

and ζ the collision rate

$$\zeta(E_\mathrm{e}, E_\gamma, \varepsilon) = \zeta_0 \hat{\zeta}(E_\mathrm{e}, E_\gamma, \varepsilon), \tag{4.10}$$

with $\zeta_0 = 2\pi e^4 E_0 c/\varepsilon E_\mathrm{e}^2$, and $\hat{\zeta}$ given by (Jones, 1968)

$$\hat{\zeta}(E_\mathrm{e}, E_\gamma, \varepsilon) = \begin{cases} 0 & \text{if} \quad E_\gamma \leq \frac{\varepsilon E_0^2}{4E_\mathrm{e}^2}, \\ \frac{E_\gamma}{\varepsilon} - \frac{E_0^2}{4E_\mathrm{e}^2} & \text{if} \quad \frac{\varepsilon E_0^2}{4E_\mathrm{e}^2} \leq E_\gamma \leq \varepsilon, \\ f(q', g_0) & \text{if} \quad \varepsilon \leq E_\gamma \leq \frac{4\varepsilon E_\mathrm{e}^2}{E_0^2 + 4\varepsilon E_\mathrm{e}}, \\ 0 & \text{if} \quad E_\gamma \geq \frac{4\varepsilon E_\mathrm{e}^2}{E_0^2 + 4\varepsilon E_\mathrm{e}}. \end{cases} \tag{4.11}$$

Here, $f(q', g_0) = 2q' \ln q' + (1 - q')(1 + (2 + g_0)q')$, $q' = E_0^2 E_\gamma / (4\varepsilon E_\mathrm{e}(E_\mathrm{e} - E_\gamma))$, and $g_0(\varepsilon, E_\gamma) = 2\varepsilon E_\gamma / E_0^2$.

The particles in the PWN also lose energy due to adiabatic processes caused by the bulk motion of the particles in the PWN, as energy is expended to expand the PWN. The adiabatic energy loss rate is given by $\dot{E}_\mathrm{e,ad} = \frac{1}{3}(\nabla \cdot \mathbf{V}) E_\mathrm{e}$ (e.g., Zhang et al., 2008). The two radiation loss rates and the adiabatic energy loss rate can be added to find the total loss rate $\dot{E}_\mathrm{e,tot}$ used in Eq. (4.5).

4.6 Diffusion, Bulk Motion and the Magnetic Field

The particle diffusion is assumed to be Bohm-type diffusion, with the scalar diffusion coefficient κ given by

$$\kappa(E_\mathrm{e}) = \kappa_B \frac{E_\mathrm{e}}{B}, \tag{4.12}$$

with $\kappa_B = c/3e$ and e denoting the elementary charge. The true form of the diffusion coefficient is still largely unknown as mentioned in Section 3.1.2, and therefore a general parametrised form for the diffusion is used:

$$\kappa(E_\mathrm{e}) = \kappa_0 \left(\frac{E_\mathrm{e}}{E_0'} \right)^q, \tag{4.13}$$

with $E_0' = 1$ TeV (with Bohm diffusion being a special case of this general parametric form). This allowed us to change the normalisation of the diffusion coefficient using κ_0 and also the energy dependence using q, to evaluate the effects that these changes have on both the particle and emission spectra as well as the size of the PWN.

The bulk particle speed inside the PWN is parametrised as (Schöck et al., 2010)

$$V(r) = V_0 \left(\frac{r}{r_0} \right)^{\alpha_\mathrm{V}}, \tag{4.14}$$

with $\alpha_{\rm V}$ the velocity profile parameter. Here V_0 is the speed at r_0. In modelling the bulk particle motion, the adiabatic energy loss timescale was set constant as done by Torres et al. (2014) as we used their results to calibrate our model. This was done by fixing

$$\tau_{\rm ad} \equiv \frac{E_{\rm e}}{\dot{E}_{\rm ad}}, \tag{4.15}$$

where $\dot{E}_{\rm ad} = (\nabla \cdot \mathbf{V})E_{\rm e}/3$ and using the analytical form of the term $(\nabla \cdot \mathbf{V})$ that follows from Eq. (4.14):

$$(\nabla \cdot \mathbf{V}) = (\alpha_{\rm V} + 2)\left(\frac{V}{r}\right). \tag{4.16}$$

Thus we find $V_0 = r_0/\tau_{\rm ad}$ and $\alpha_{\rm V} = 1$ in this case.

I described the geometry of the B-field in Section 3.1.2 and I modelled this geometry by parametrising the B-field with

$$B(r,t) = B_{\rm age}\left(\frac{r}{r_0}\right)^{\alpha_{\rm B}}\left(\frac{t}{t_{\rm age}}\right)^{\beta_{\rm B}}, \tag{4.17}$$

where $B_{\rm age}$ is the present-day B-field at $r = r_0$ and $t = t_{\rm age}$, t the time since the PWN's birth, $t_{\rm age}$ is the PWN age, and $\alpha_{\rm B}$ and $\beta_{\rm B}$ the B-field parameters. This parametrised form of the B-field goes to infinity if $t = 0$ and therefore we limit the B-field to $B_{\rm max} = 10B_{\rm age}$. Although this is an arbitrary assumption, we found that limiting the B-field to larger values ($B_{\rm max} = 100B_{\rm age}$ and $B_{\rm max} = 1000B_{\rm age}$) has a negligible effect on the predicted SED, but significantly increases the computation time. This parametrised form of the B-field is mainly used to see what effect changes in the B-field will have on the SED and the size of the PWN. We assumed the parametric form for the B-field for mathematical expedience, assuming the PWN is young. In fact, it is explicitly stated in Torres et al. (2014) that at earlier times the B-field may be approximated using a power law in time ($B \sim t^{-1.3}$; see also Vorster et al. 2013 and references therein). One could use the numerical solution as done by Torres et al. (2014), but the question then is what the effect of uncertainty on $R_{\rm PWN}(t)$ will be on the eventual $B(t)$; i.e., this approach is also not without some assumptions. Our simple approach of using a parametrised B-field is meant to be an approximation to the output of a complex MHD code. The solution to such a code is beyond the scope of this study and is avoided for the reason that we are focusing on emission physics. In future, one may consider the combination of emission and MHD codes to obtain even more realistic results. For older PWNe, a numeric approach will be better and the effect of the reverse shock will also have to be taken into account.

The relationship between the magnetic field and the bulk motion of the particles can be derived by following Kennel and Coroniti (1984a) and assuming that the magnetic field

is toroidal and the bulk flow is purely radial. We also assume that, since the nebular plasma is a good conductor, we can apply ideal MHD equations (characterised by infinite macroscopic conductivity) to describe the PWN wind. In this case, Ohm's law becomes

$$\mathbf{E} = -\frac{\mathbf{v}}{c} \times \mathbf{B} \tag{4.18}$$

and by combining this with Faraday's law, we find (e.g., Ferreira and de Jager, 2008b)

$$\frac{\partial \mathbf{B}}{\partial t} = \nabla \times (\mathbf{v} \times \mathbf{B}). \tag{4.19}$$

To simply link the radial profiles of the magnetic field and bulk motion of the particles, we follow Schöck et al. (2010), Holler et al. (2012b), Lu et al. (2017b, 2019) and assume that the temporal change in the magnetic field is slow enough that we can set $\partial \mathbf{B}/\partial t \simeq 0$ in the above equation, even for a time-dependent prescription of B (this assumption holds exactly true for steady-state models such as those of Kennel and Coroniti 1984a, Vorster et al. 2013). We have investigated this assumption *a posteriori* for typical PWN parameters, considered Eq. (4.17), notably $\beta_{\rm B} < -1$, and found that $\partial \mathbf{B}/\partial t < \nabla \times (\mathbf{v} \times \mathbf{B})$ for large values of V_0 and $\alpha_{\rm B} > 0$ (implying larger spatial gradients) or large times t, small distances from the centre r, or small (more negative) $\beta_{\rm B}$ (implying smaller temporal gradients of the magnetic field) when $\alpha_V + \alpha_B = -1$. This conclusion is independent of $B_{\rm age}$, but becomes stronger for smaller r_0 (larger spatial gradient) and larger $t_{\rm age}$ or larger (less negative) $\beta_{\rm B}$ (smaller temporal gradient). For small values of α_B, similar to what we will be using in what follows, the spatial term dominates (to various degrees) the temporal one for most times and distances, especially later times and closer distances. Thus, we think that it is a reasonable approximation to drop the temporal term in favour of the spatial one for our current modelling. In the general case of Equation (4.19), one can show that $\alpha_V + \alpha_B + 1 \propto f(r,t)$, with f representing some multivariate function (and $f = 0$ if $\partial \mathbf{B}/\partial t = 0$), i.e., in this general case one would not be able to use our parametric prescription for $\mathbf{V}$ or $\mathbf{B}$, as the indices do not remain constant with t nor r. For a more general description (and including the magnetic field's temporal derivative in this linking equation), MHD modelling would be needed. From this follows $VBr = V_0 B_0 r_0 =$ constant, which for our parametric specifications of the magnetic field and bulk flow implies that

$$\alpha_V + \alpha_B = -1. \tag{4.20}$$

This relation is used to reduce the number of free parameters by one and to simplify our search for best-fit parameters in later sections.

4.7 Energy Conservation

The rotational energy of the pulsar is ultimately the reservoir from which is derived the energy of the pulsar wind particles and electromagnetic fields (e.g., Gelfand, 2017). We explicitly direct a fraction η of the spin-down luminosity to the particle injection spectrum as described above. We tested the consistency of our calculations by integrating the injection spectrum multiplied by particle energy $E_{\rm e}Q(E_{\rm e})$ over volume and particle energy (e.g., Sefako and de Jager, 2003), and did indeed recover η.

Secondly, we have to ensure that the fraction of spin-down power being converted into magnetic energy amounts to no more than $\eta_{\rm B} = 1 - \eta \ll 1$. Torres et al. (2014) and others explicitly ensure energy conservation by solving for the magnetic field using the following equation

$$\frac{dW_{\rm B}}{dt} = \eta_{\rm B} L - \frac{W_{\rm B}}{R_{\rm PWN}} \left(\frac{dR_{\rm PWN}}{dt} \right), \tag{4.21}$$

with the final term describing adiabatic losses, $W_{\rm B}$ being the magnetic energy

$$W_{\rm B} \equiv \frac{4\pi}{3} R_{\rm PWN}^3(t) \frac{B^2(t)}{8\pi}, \tag{4.22}$$

and assuming a PWN radius (Van der Swaluw et al., 2001)

$$R_{\rm PWN}(t) = C \left(\frac{L_0 t}{E_0} \right)^{1/5} V_{\rm ej} t \propto t^{6/5}, \tag{4.23}$$

with $C \approx 1$, $V_{\rm ej}$ the ejecta speed, L_0 the pulsar spin-down luminosity at birth, and E_0 the energy of the supernova explosion.

We used a parametric form for the magnetic field to allow us to explore a wider variety of magnetic field behaviour, given the uncertainty in PWN radius and $\eta_{\rm B}$ (considering, e.g., its time-dependence or not). However, we implicitly ensured energy conservation by letting our magnetic field approximate the one calculated as explained above (see Figure 4.2). Since our respective magnetic fields are similar, so too are our predicted SR components (see Figure 3 of Van Rensburg et al. 2018).

In order to address this point more quantitatively, we solved for $\eta_{\rm B}$ using Equation (4.21) upon substituting our parametric expression for the magnetic field (see Figure 4.3). We used Equation (4.23) to approximate the PWN radius as in the expression for $W_{\rm B}$ given in Equation 4.22. It was not clear what value to use for $R_{\rm PWN}$. This is because in our model, we assume a distant escaping boundary and let the particles flow into a static radial grid and radiate, so we may determine the time-dependent observed PWN size without having to impose it *a priori*. Any radius derived from the observed size of the PWN is necessarily dependent on photon energy; also, it is arbitrary to define a radius

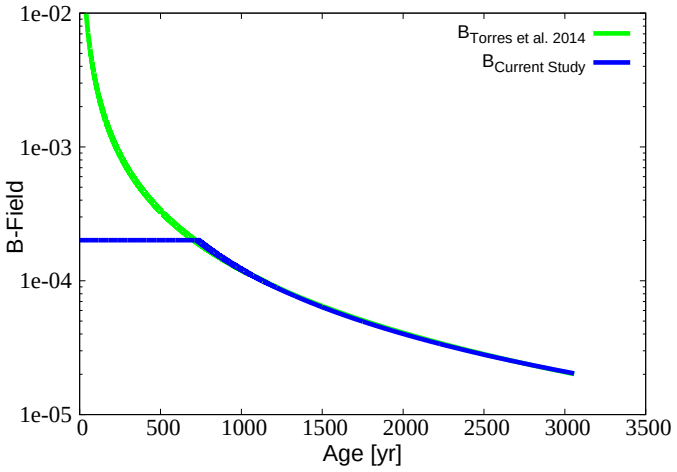

FIGURE 4.2: Comparison between the parametric form (blue line, $\alpha_{\rm B} = 0$, $\beta_B = -1.6$) and the analytical form used by Torres et al. (2014) (green line) of the magnetic field of PWN G0.9+0.1. Our magnetic field is set to a constant at early times to make the code more efficient (i.e., to limit the dynamical time step that scales as the SR loss time scale $t_{\rm SR} \propto B^{-2}$).

based on some fixed drop in the steady-state particle spectrum. We therefore opted to use the standard analytic expression for free expansion, which allowed us to directly compare our results to those of Torres et al. (2014). From Figure 4.3, we recover the correct value of $\eta_{\rm B} \approx 1\%$ for the case of G0.9+0.1 (Torres et al., 2014). Our parametric magnetic field slightly underestimates the analytic magnetic field at early times, leading to a lower value of $\eta_{\rm B}$ at those times. At an age of approximately 800 years, the parametric magnetic field follows the $\beta_B = -1.6$ profile and thus the $\eta_{\rm B}$ value is similar to that of Torres et al. (2014). The discontinuous behaviour around 800 years is a result of taking the derivative of a discontinuous magnetic field around this age. We thus found that our implied value for $\eta_{\rm B}$ is close to that of Torres et al. (2014), demonstrating energy conservation in our model (since $\eta_{\rm B} \approx 0.01$ and $\eta \approx 0.99$ for this source, so the particle energetics therefore substantially dominates).

4.8 Numerical Solution to the Transport Equation

Each of the terms in Eq. (4.5) are now specified and thus it can be solved numerically. To do this, Eq. (4.5) is discretised. I assume spherical symmetry, thus $\partial/\partial\theta = 0$ and $\partial/\partial\phi = 0$, so that $\nabla^2 N_{\rm e} = 1/r^2 \left(\partial/\partial r \left[r^2 \partial N_{\rm e}/\partial r\right]\right)$. My first approach was to discretise Eq. (4.5), by using a simple Euler method. It soon became clear that this method was numerically unstable. The DuFort-Frankel scheme was tested and found to be stable

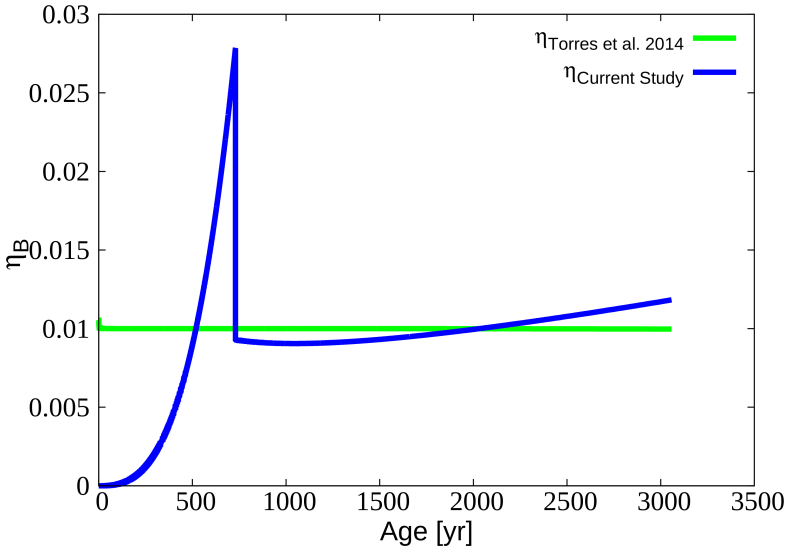

FIGURE 4.3: Comparison of calculated η_B for the parametric form (blue line) vs. the analytical form of the magnetic field used by Torres et al. (2014) (green line).

enough to discretise Eq. (4.5) giving

$$\begin{aligned}(1-z+\beta)(N_e)_{i,j+1,k} &= 2Q_{i,j,1}\triangle t \\ &+ (1+z-\beta)(N_e)_{i,j-1,k} \\ &+ (\beta+\gamma-\eta)(N_e)_{i,j,k+1} \\ &+ (\beta-\gamma+\eta)(N_e)_{i,j,k-1} \\ &- 2(\nabla\cdot\mathbf{V})_{i,j,k}\triangle t(N_e)_{i,j,k} \\ &+ \frac{2}{\{(dE_e)_{i+1,j,k}+(dE_e)_{i,j,k}\}}\times \\ &\Big\{r_a\left(dE_{e,loss}\right)_{i+1,j,k}(N_e)_{i+1,j,k} \\ &- \frac{1}{r_a}\left(dE_{e,loss}\right)_{i-1,j,k}(N_e)_{i-1,j,k}\Big\},\end{aligned} \tag{4.24}$$

with $\beta = 2\kappa\Delta t/(\Delta r)^2$, $\gamma = 2\kappa\Delta t/(r\Delta r)$, $\eta = V_k\Delta t/\Delta r$, Δr the step size of the spatial dimension, Δt the step size of the time dimension, $dE_{e,loss} = \dot{E}_{e,tot}\Delta t$, and V_k the bulk particle motion in the current radial bin. Also, $r_a = (\Delta E_e)_{i+1,j,k}/(\Delta E_e)_{i,j,k}$ with

$$z = \left(\frac{1}{(\Delta E_e)_{i+1,j,k}-(\Delta E_e)_{i,j,k}}\right)\left(\frac{1}{r_a}-r_a\right)(\dot{E}_e)_{i,j,k}. \tag{4.25}$$

Here i, j, k are the indices of energy, time, and space respectively. See Appendix A.5 for the full mathematical discretisation.

We limit the particle energy following Venter and de Jager (2007),

$$E_{\max} = \frac{e}{2}\sqrt{\frac{L(t)\sigma}{c(1+\sigma)}}. \tag{4.26}$$

This is a containment argument, limiting the Larmor radius $r_{\rm L} \lesssim 0.5 r_{\rm s}$ with $r_{\rm s}$ the shock radius. Particles with $E_{\rm e} > E_{\max}$ are assumed to have escaped from the PWN.

4.9 Boundary Conditions

The boundary conditions of our model are handled as follows. The multi-zone model divides the PWN into spherical shells to solve Eq. (4.24) numerically. The particles are injected into the innermost zone/annulus ($r_{\min} = r_0 = r_{\rm ts}$) and allowed to propagate through the different zones, with the spectral evolution being governed by Eq. (4.24). As the initial condition, all zones are assumed to be devoid of any particles, i.e., $N_{\rm e} = 0$ at $t = 0$, and a set of "ghost points" that are also devoid of particles are defined outside the boundaries in time domain, as the DuFort-Frankel scheme requires two previous time steps. For the spatial dimension, the boundary conditions are reflective at the inner boundary to avoid losing particles towards the pulsar past the termination shock and at the outer boundary $r_{\max}$ the particles are allowed to escape. To model the escape of particles at the outer boundary, the particle spectrum is set to zero there, while for the reflective inner boundary we need zero flux through the innermost radial shell. Therefore we set

$$S = -\kappa\left(\frac{(N_{\rm e})_{i,j,1} - (N_{\rm e})_{i,j,0}}{\Delta r}\right) + V_{i,j,1}\left(\frac{(N_{\rm e})_{i,j,1} + (N_{\rm e})_{i,j,0}}{2}\right) = 0, \tag{4.27}$$

leading to:

$$(N_{\rm e})_{i,j,0} = (N_{\rm e})_{i,j,1} \times \frac{\kappa/\Delta r - V_{i,j,1}/2}{\kappa/\Delta r + V_{i,j,1}/2}. \tag{4.28}$$

We solve $N_{\rm e}$ for a minimum particle energy of $E_{\min} = 10^{-7}$ erg by allowing particles with smaller energies to "escape". The maximum particles energy is limited by Eq. (4.26). The injection of particles into the PWN can also be seen as a boundary condition. We inject the particles at a certain rate and assume that the particle injection spectrum Q'' is uniformly distributed in the first zone. Thus

$$\frac{Q''}{V^1_{\rm shell}} = Q, \tag{4.29}$$

where $V^1_{\rm shell}$ is the volume of the first zone and Q the injection spectrum per unit energy, time, and volume as used in Eq. (4.24).

In Van Rensburg et al. (2014) we demonstrated convergence of the model output as one increases the mesh density, i.e., showing convergence of both the particle spectrum and SED with an increase in the number of radial, particle energy and photon energy bins.

4.10 Radiation Spectrum

The radiation spectrum is calculated following sections 3.2.1 and 3.2.2. The time-dependent photon spectrum of each zone can be calculated, using the electron spectrum $N_{\rm e}(r, E_{\rm e})$ solved for each zone from Eq. (4.5).

For IC, we have (Kopp et al., 2013)

$$\left(\frac{dN_\gamma}{dE_\gamma}\right)_{IC} = \frac{g_{IC}}{A}\sum_{l=1}^{3}\iint n_{\varepsilon,l}(r,\varepsilon,T_l) \times \frac{\mathcal{N}_{\rm e}}{\varepsilon E_{\rm e}^2}\zeta(E_{\rm e},E_\gamma,\varepsilon)d\varepsilon dE_{\rm e}, \tag{4.30}$$

where $A = 4\pi d^2$, d the distance to the source, and $\mathcal{N}_{\rm e} = N_{\rm e}V_{\rm shell}$ is the number of electrons per energy interval in a spherical shell at radius r. We consider $l = 3$ BB components of target photons, i.e., the cosmic background radiation (CMB), Galactic background infrared (IR) photons, and starlight.

For SR, we have

$$\left(\frac{dN_\gamma}{dE_\gamma}\right)_{\rm SR} = \frac{1}{A}\frac{1}{hE_\gamma}\frac{\sqrt{3}e^3B(r,t)}{E_0}\iint_0^{\pi/2}\mathcal{N}_{\rm e}(E_{\rm e},r) \times F\left(\frac{\nu}{\nu_{\rm cr}(E_{\rm e},\theta,r)}\right)\sin^2\theta d\theta dE_{\rm e}, \tag{4.31}$$

with $\nu_{\rm cr}$ the critical frequency (with pitch angle θ, which we assume to be $\pi/2$ so that $\sin^2\theta = 1$) given by

$$\nu_{\rm cr}(E_{\rm e},r) = \frac{3ec}{4\pi E_0^3}E_{\rm e}^2B_\perp(r,t), \tag{4.32}$$

and

$$F(x) = x\int_x^\infty K_{5/3}(y)dy, \tag{4.33}$$

where $K_{5/3}$ the modified Bessel function of order 5/3. The total radiation spectrum at Earth is found by calculating Eq. (4.30) and Eq. (4.31) for each spatial zone in the model and adding them.

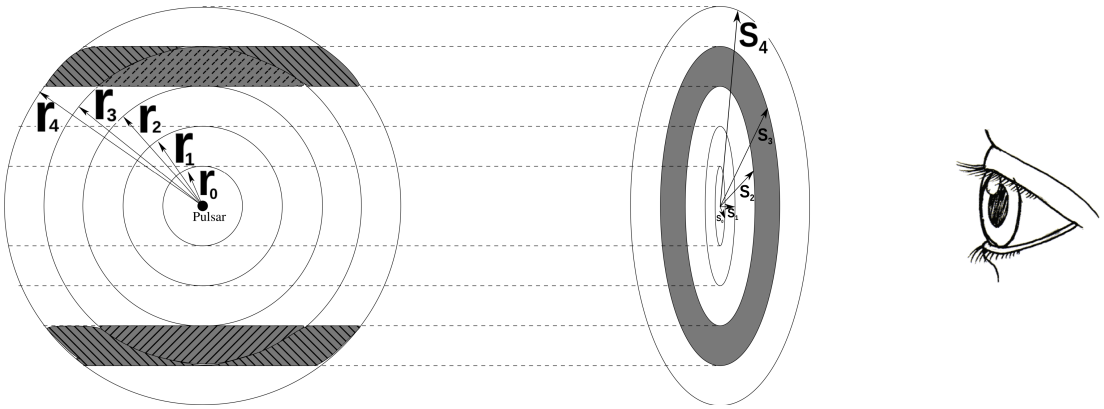

FIGURE 4.4: Schematic for the geometry of the LOS calculation.

4.11 Line-of-Sight Calculation

Next, the radiation per unit volume can be calculated by dividing the radiation spectrum by the volume of the zone where the radiation originated. This is used to perform the line-of-sight (LOS) calculation to project the radiation onto the plane of the sky in order to find the SB and flux as a function of 2D projected radius. This allows us to estimate the size of the PWN as well as to determine photon spectra as function of distance from the central pulsar.

We multiply the radiation per unit volume by the volume in a particular LOS ($V_{\rm LOS}$) as viewed from Earth (grey regions in the left-hand panel of Figure 4.4). The pulsar plus the multi-zone model of the surrounding PWN are on the left-hand side of Figure 4.4 and the right-hand side shows how "LOS cylinders" are chosen through the PWN, with the observer looking on from the right. The source is very far from Earth and cylinders instead of cones are chosen as a good first approximation. Cylinders with radii s, intersecting the spherical zones and the spherical shells with radii r, are assumed to have the same bin sizes. This results in the observer viewing the projected PWN as several 2D "annuli" with different radii, for example the shaded region in the right-hand panel of Figure 4.4. The radiation in a certain annulus can thus be calculated if the volume of the intersection ($V_{\rm LOS}$) between a particular hollow cylinder and the spheres is known. Setting $a \equiv \sqrt{r^2 - s^2}$, we find that the volume of intersection between a cylinder and sphere $V(s)$ is

$$V(s) = \frac{4\pi}{3}\left[-\left(r^2 - s^2\right)^{\frac{3}{2}} + r^3\right]. \tag{4.34}$$

The LOS volume ($V_{\rm LOS}$) can now be calculated by subtracting the correct volumes from one another. For example, the intersection volume of an annulus with radius s_k and

sphere with r_i is

$$V_{\rm LOS} = \left(V_{i,k} - V_{i,k-1}\right) - \left(V_{i-1,k} - V_{i-1,k-1}\right). \tag{4.35}$$

This expression, however, holds only when $s < r$. If s is larger or equal to r, then the intersection volume will simply be the volume of the sphere of radius r. The total radiation for the specific LOS, or annulus, can be calculated by adding the radiation density for all the segments (left-hand panel of Figure 4.4) and then multiplying it by $V_{\rm LOS}$. To find the total radiation at Earth from the PWN, the radiation from all the different LOSs (annuli) may be added.

As a test of this LOS calculation, we summed the total flux from all the spheres to find the total flux from the PWN and then also added the flux from all the cylinders after the LOS calculation. Both these calculations yielded the same flux. We can now use this projected flux to calculate the SB profiles as well as photon index profiles.

4.12 Summary

In this Chapter I have demonstrated how the particle transport, evolution and radiation in PWNe are implemented in our spatio-temporal leptonic emission code. In the next chapter a parameter study is conducted to provide insight into the nature of the code.

Chapter 5

Model Calibration and Parameter Study

The model we have developed has to be calibrated with previous authors' modelling attempts to verify its validity. This is accomplished by comparing our model outputs with that of Venter and de Jager (2007) and Torres et al. (2014). The second part of this chapter is dedicated to exploring and understanding the model behaviour in different parts of parameter space to be able to make better predictions when attempting to fit the model to specific sources in Chapter 6. This chapter is largely based on Van Rensburg et al. (2018).

5.1 Code Calibration via SED fits

PWN G0.9+0.1 will be used as a case study in our code. Here I briefly summarise some of its observational properties. Helfand and Becker (1987) observed G0.9+0.1 for 45-minute integrations at 20 cm and 6 cm, which led to the discovery of the composite nature of this bright, extended source near the Galactic Centre (GC) in the radio band. SNR G0.9+0.1 has become a well-known SNR, with an estimated age of a few thousand years. This source exhibits a flat-spectrum radio core ($\sim 2'$ across) corresponding to the PWN, and also clearly shows steeper-spectrum shell components ($\sim 8'$ diameter shell). While performing a survey of the GC, Sidoli et al. (2004) serendipitously observed SNR G0.9+0.1 using the *XMM*-Newton telescope. Their observations provided the first evidence of X-ray emission from PWN G0.9+0.1. Sidoli et al. (2004) fit an absorbed power-law spectrum that yielded a photon index of $\Gamma \sim 1.9$ and an energy flux of $F = 4.8 \times 10^{-12}$ erg cm^{-2} s^{-1} in the 2−10 keV energy band. This translates to a luminosity of $L_{\rm X} \sim 5 \times 10^{34}$ erg s^{-1} for a distance of 10 kpc. Aharonian et al. (2005) studied VHE

gamma rays from the GC with the H.E.S.S. telescope. During the observation of Sgr A*, two sources of VHE gamma rays were clearly visible, SNR G0.9+0.1 being one of these. They performed a power-law fit to the observed spectrum and found a photon index of $2.29\pm0.14_{\rm stat}$ with a photon flux of $(5.5\pm0.8_{\rm stat})\times10^{-12}$ cm^{-2} s^{-1} for energies above 200 GeV. This flux is only $\sim 2\%$ of the flux from the Crab Nebula, making PWN G0.9+0.1 one of the weakest sources detected at TeV energies to date. Some years later, the radio pulsar PSR J1747−2809 was discovered in PWN G0.9+0.1 with period $P = 52$ ms and $\dot{P} = 1.85 \times 10^{-13}$ (Camilo et al., 2009). More information on this source and the final model fits will be given in Section 6.2.3.

In the next section, I calibrate our new model against a previous more basic model (Venter and de Jager, 2007). This model only assumed a parametric form for the temporal dependence of the B-field, and did not take into account adiabatic losses at the expense of the magnetic energy and the effect thereof on the B-field's time dependence. They only incorporated SR losses and diffusion in modelling the transport of particles, treating these processes as dominant. Calibration with this older model is a first point of reference and is also done for historical reasons, since our new model incorporates many of the basic elements of the Venter and de Jager (2007) model. We also calibrated our new model against a more modern model (Torres et al., 2014). Both of these earlier works assumed one-zone models (0D).

5.1.1 Calibration against the Model of Venter and de Jager (2007)

The assumed model parameters used to calibrate our model against that of Venter and de Jager (2007) are listed in Table 5.1; n is the braking index given by $n = \Omega\ddot{\Omega}/\dot{\Omega}^2$, with $\Omega = 2\pi/P$ the angular speed and P the period of rotation of the pulsar; $\beta_{\rm VdJ}$ is the B-field parameter as in Eq. (5.2), and $B(t_{\rm age})$ is the present-day B-field. To closer align with the procedure of Venter and de Jager (2007), for the sake of calibration, we fixed the value of L_0 and birth period $P_0 = 43$ ms (Van der Swaluw and Wu, 2001), assuming no decay of the pulsar B-field, i.e., $P_0\dot{P}_0 = P\dot{P}$. In the rest of the study, however, we calculate $\tau_{\rm c}$ using P and $\dot{P}$, we assume $t_{\rm age}$, and from this follows τ_0 and L_0 (without the need to calculate P_0 and $\dot{P}_0$ explicitly, see Appendix A.3). In this first calibration with Venter and de Jager (2007), we use $B(t_{\rm age}) = 40.0$ μG, noting that their model was developed before the discovery of PSR J1747−2809 associated with PWN G0.9+0.1. The more reasonable value for the present-day B-field, 14.0 μG, is used in the calibration against the model of Torres et al. (2014) in the next section as we now know P and $\dot{P}$ for the embedded pulsar, as mentioned above. Also, η is the conversion efficiency as mentioned in Eq. (4.7), $t_{\rm age}$ is the age of the PWN, τ_0 is the characteristic spin-down timescale of the pulsar, d is the distance to the PWN, α_1 and

α_2 are the spectral indices of the injection spectrum, and L_0 the spin-down luminosity at birth. The sigma parameter is the ratio of the electromagnetic to particle energy density or luminosity ($\sigma = L_{\rm EB}/L_{\rm E}$) and is used to calculate the maximum particle energy according to the following formula (Venter and de Jager, 2007):

$$E(t) = \frac{e}{2}\sqrt{\frac{\sigma L(t)}{(1+\sigma)c}}. \tag{5.1}$$

We chose three soft-photon components modelled as black bodies (BB): the CMB with a temperature of $T_1 = 2.76$ K and an average energy density of $u_1 = 0.23$ eV/cm^3, Galactic background infrared photons as component 2, and optical starlight as component 3 (with T_i and u_i as given in Table 5.1). For these assumed model parameters we find the SED as shown in Figure 5.1. The radio data are from Helfand and Becker (1987), the X-ray data from Porquet et al. (2003) and Sidoli et al. (2004), and the gamma-ray data from Aharonian et al. (2005). The solid line represents our predicted SED while the dashed line shows the output from the model of Venter and de Jager (2007).

To compare our new model with that of Venter and de Jager (2007), we had to remove the effects of the bulk particle motion, as their model did not incorporate such motion and only considered diffusion, SR losses, and particle escape. Thus their model did not include adiabatic losses nor convection (see below). The way the effects of these processes are removed from the new model is by simply setting the bulk speed inside the PWN to zero. Venter and de Jager (2007) also modelled the B-field by parametrising it as

$$B(t) = \frac{B_0}{1 + \left(t/\tau_0\right)^{\beta_{\rm VdJ}}}. \tag{5.2}$$

Our model was adapted to also parametrise the B-field using this same time-dependent form. These two simple changes to our model allowed us to calibrate our model against theirs as seen in Figure 5.1.

Our time-dependent, multi-zone PWN model does not reproduce the results of Venter and de Jager (2007) exactly, but the respective SEDs are quite close (see bottom panel of Figure 5.1). This can be explained by the fact that the older model did not take into account IC losses in the particle transport, since it assumed SR losses to dominate. This led to particle energy losses being underestimated, leaving an excess of high-energy particles. Their IC radiation is therefore slightly higher than our new model prediction. Other differences may result from our very different treatment of the particle transport as we solved a full transport equation and Venter and de Jager (2007) solved a linearised transport equation using SR losses, diffusion and effective timescales.

TABLE 5.1: Values of model parameters as used in the calibration against the model of Venter and de Jager (2007) for PWN G0.9+0.1.

Model Parameter	Symbol	Value
Braking index	n	3
B-field parameter	β_{VdJ}	0.5
Present-day B-field	$B(t_{\mathrm{age}})$	40.0 μG
Conversion efficiency	η	0.6
Age	t_{age}	1 900 yr
Characteristic timescale	τ_0	3 681 yr
Distance	d	8.5 kpc
Q index 1	α_1	-1.0
Q index 2	α_2	-2.6
Initial spin-down power(10^{38}erg s^{-1})	L_0	0.99
Sigma parameter	σ	0.2
Soft-photon component 1	T_1 and u_1	2.76 K, 0.23 eV/cm^3
Soft-photon component 2	T_2 and u_2	35 K, 0.5 eV/cm^3
Soft-photon component 3	T_3 and u_3	4 500 K, 50 eV/cm^3

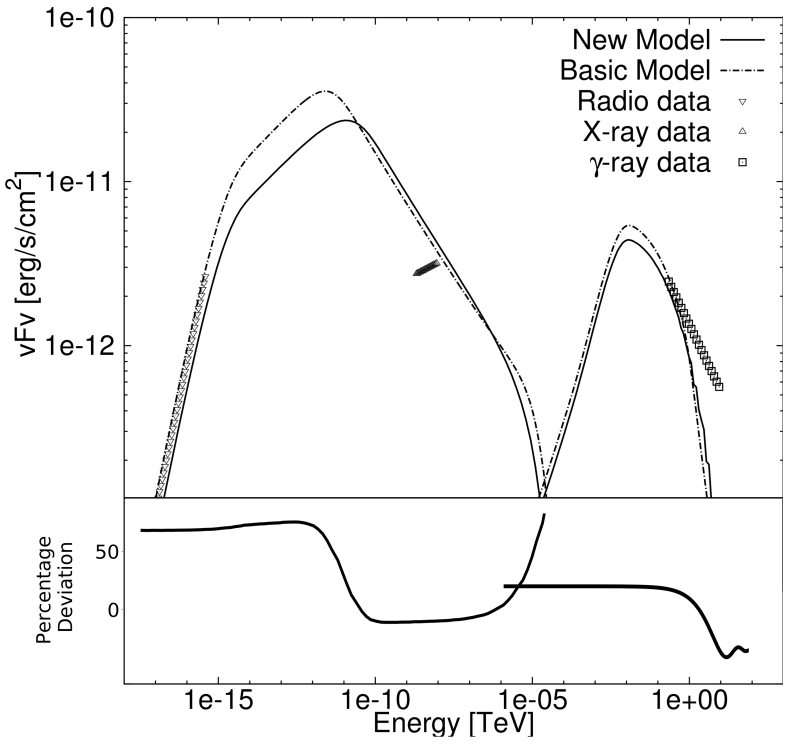

FIGURE 5.1: Calibration against the model of Venter and de Jager (2007) for PWN G0.9+0.1. The bottom panel indicates the percentage deviation between the two SEDs.

It should be noted that in Table 5.1, the two variables η and σ are independent. They are, however, in reality related by $\eta = 1/(1+\sigma)$. This inconsistency is only present in the calibration with Venter and de Jager (2007) and is correctly implemented in the rest of the modelling.

Our model fits the data reasonable well, but still has trouble in fitting the slope of the X-ray spectrum. Vorster et al. (2013) modelled PWN G21.5−0.9 where they also encountered this problem when using a broken-power-law injection spectrum that connects

smoothly at some break energy. They therefore used a two-component particle injection spectrum that does not transition smoothly (instead the low-energy component cuts off steeply in order to connect to the lower-flux, high-energy component), allowing them to fit both the radio and X-ray spectral slopes. This is something worth noting for future development of our code.

5.1.2 Calibration against the Model of Torres et al. (2014)

As a second calibration, we used results from a more recent study by Torres et al. (2014), who created a time-dependent model of young PWNe by modelling them as a single sphere (0D). We again use PWN G0.9+0.1 as the calibration source. The assumed model parameters for this second calibration are given in Table 5.2. The B-field is now modelled according to Eq. (4.17), hence the values of $\alpha_{\rm B}$ and $\beta_{\rm B}$ in Table 5.2. Some of the parameters are different from those used during the calibration with the model of Venter and de Jager (2007). One of these changes is the present-day B-field that is now set to 14 μG, versus the previous value of 40 μG. Furthermore, the discovery of pulsar PSR J1747−2809 in the PWN G0.9+0.1 yielded P and $\dot{P}$, which pin down the value of $L(t_{\rm age})$. The B-field is parametrised using $\alpha_{\rm B} = 0$ and $\beta_{\rm B} = -1.3$, which, from Eq. (4.17), indicates that the B-field is constant in the spatial dimension.

Torres et al. (2014) model the time dependence of the B-field using

$$\int_0^t (1-\eta) L(t') R_{\rm PWN}(t') dt' = W_B R_{\rm PWN}, \tag{5.3}$$

where

$$W_B = \frac{4\pi}{3} R_{\rm PWN}^3(t) \frac{B^2(t)}{8\pi}, \tag{5.4}$$

and mention that if the age of the PWN is less than the characteristic age ($t_{\rm age} < \tau_0$), then $B(t) \propto t^{-1.3}$. We therefore set the value of $\beta_{\rm B} = -1.3$. While Torres et al. (2014) solved $B(t)$ numerically, we can approximate the early-age limit of $B(t)$ using such a power law.

One thing to note here is the usage of $R_{\rm PWN}$. Torres et al. (2014) explicitly use a time-dependent PWN radius for G0.9+0.1, setting $R_{\rm PWN}(t_{\rm age}) = 2.5$ pc. However, we do not. Instead, for simplicity, we chose an escape boundary $r_{\rm max} \gg R_{\rm PWN}$, and then later calculate the observable size of the PWN by noting where the SB profile has decreased by two-thirds from the value at $r_{\rm min}$ (from an observer's point of view; this is possible since we have information about the morphology of the PWN). We assume this distant boundary for the PWN where particles escape. We restrict ourselves to modelling young PWN where free expansion of the wind should be justified. Later evolutionary phases

may be characterised by a reverse shock or reverberation phase where interaction with the ambient medium is much more important. If we would enforce particle escape at a moving boundary $R_{\rm PWN}$ rather than following our approach of escape at a distant boundary, the particle density may be somewhat lower, leading to slightly lower fluxes than predicted by our model. This approach is admittedly different from the standard one, but with a very particular motivation: If we assume a standard expression for $R_{\rm PWN}(t)$ and if the age of the PWN is much smaller than the radiation loss timescale, one would expect no evolution of PWN size with energy, contrary to what is observed in some PWNe. The energy-dependent morphology seem to be closely linked with the stage of evolution of the PWN and whether particles escape beyond $R_{\rm PWN}(t)$. If the pulsar is very slowly moving one might observe a composite supernova remnant (SNR), with nebular and shell emission visible in both radio and X-ray bands. Such young systems exhibit a high degree of spherical symmetry and it is possible that the SNR reverse shock has not yet interacted with the PWN (e.g., SNR G11.2−0.3 and G21.5−0.9) and particles may not have had time to significantly cool due to radiation losses. The PWN around PSR B1509−58 provides a counter example, exhibiting a strong anti-correlation between the radio and X-ray emission morphology. In the case of middle-aged systems that are associated with fast-moving pulsars and gamma-ray sources, one may observe complex morphologies (e.g., collimated X-ray emission vs. more diffuse surrounding radio emission in the Rabbit Nebula and G327.1−1.1; Roberts et al. 2005, Slane 2017). In older PWNe, a decreasing B-field may lead to gamma-ray emission dominating the observed radio and X-ray emission (e.g., HESS J1825−137 that reveals a morphology that becomes strikingly smaller with energy; Slane 2017), probably due to the fact that high-energy particles are the ones that preferentially cool and escape from the PWN. Hinton et al. (2011) argue that while confinement of particles in PWNe may be effective in their early evolution, the interaction with the SNR reverse shock may disrupt the PWN via, e.g., the growth of Rayleigh-Taylor instabilities, and that diffusion of particles out of the PWN becomes possible. In the case of PWN G0.9+0.1 we may be witnessing an intermediate case. While this PWN is quite young and the radio and X-ray sizes are very similar, the X-ray morphology seems to be slightly smaller (Dubner et al., 2008). This hint of morphological evolution (Figure 5.22) is consistent with the observed softening of the X-ray spectrum (indicating dominant SR losses) as one moves from the inner to outer regions of the PWN (Porquet et al., 2003).

Conversely to the other approaches, I therefore calculate the energy-dependent PWN size using the predicted surface brightness profile. However, this approach does not ignore the dynamical evolution of the PWN. While we determine $R_{\rm PWN}(t)$ from the emission properties, we do take into account the effect of evolution on the B-field profile by choosing $\beta_{\rm B} = -1.3$. Our parametric approach captures the essence of the evolution

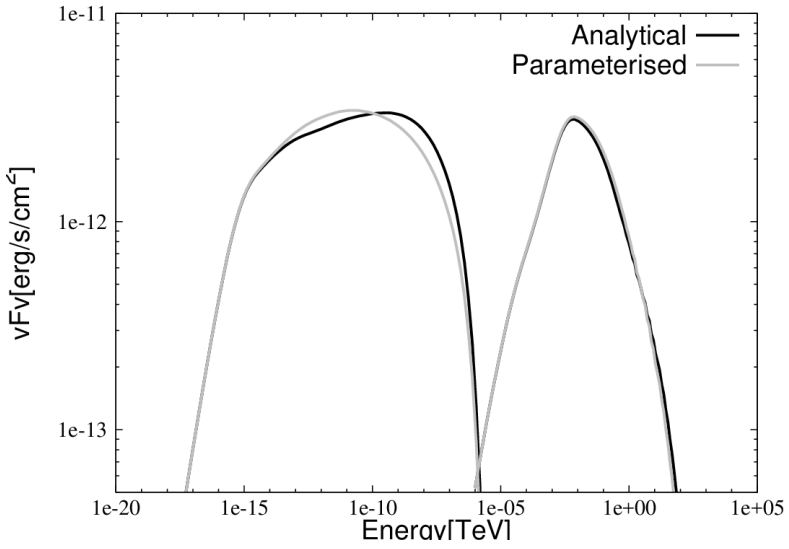

FIGURE 5.2: Comparison of the predicted SED for the parametric vs. analytical treatment of the temporal evolution of the B-field.

(e.g., as assumed by Torres et al. 2014) in a simplified way, but allows us the freedom to infer this profile, should the data require a somewhat different behaviour for the decline of the B-field with radius. As a test we performed alternative runs of our code, in which we included the formalism of Torres et al. (2014) to calculate the B-field. We found no significant difference in the predicted SED when using these two different approaches (Figure 5.2), justifying our usage of the parametric approach when modelling young PWNe. In Section 4.6 we do however mention that $\partial \mathbf{B}/\partial t = 0$ for certain assumptions and if this is not the case, then this parametric form will no longer be valid.

A second question to address is whether our parametric approach conserves energy. We have indeed tested this and if is discussed in detail in Section 4.7.

TABLE 5.2: Values of model parameters as used in the calibration against the model of Torres et al. (2014) for PWN G0.9+0.1.

Model Parameter	Symbol	Value
Braking index	n	3
B-field parameter	$\alpha_{\rm B}$	0.0
B-field parameter	$\beta_{\rm B}$	-1.3
V parameter	$\alpha_{\rm V}$	1.0
Present-day B-field	$B(t_{\rm age})$	14.0 μG
Conversion efficiency	η	0.99
Age	$t_{\rm age}$	2 000 yr
Characteristic timescale	τ_0	3 305 yr
Distance	d	8.5 kpc
Q index 1	α_1	-1.4
Q index 2	α_2	-2.7
Initial spin-down power(10^{38}erg s^{-1})	L_0	1.1
Sigma parameter	σ	0.01
Soft-photon component 1	T_1 and u_1	2.76 K, 0.23 eV/cm^3
Soft-photon component 2	T_2 and u_2	30 K, 2.5 eV/cm^3
Soft-photon component 3	T_3 and u_3	3 000 K, 25 eV/cm^3

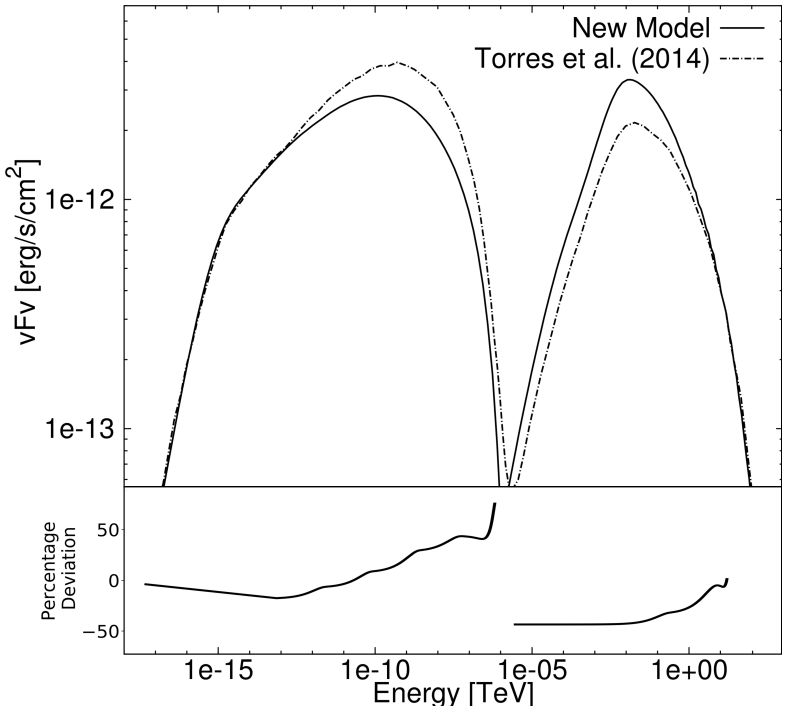

FIGURE 5.3: Calibration against the model of Torres et al. (2014) for PWN G0.9+0.1. Bottom panel indicates the percentage deviation between the two SEDs.

The bulk motion of the particles is parametrised by Eq. (4.14) using model parameters $\alpha_{\rm V}$, V_0, and $r_0 = r_{\rm min}$ and the bulk speed is parametrised by setting $\alpha_{\rm V} = 1.0$, with $V_0 = r_0/t_{\rm age}$. This is done so that our model can have the same adiabatic energy loss rate assumed by Torres et al. (2014). They have a constant adiabatic energy loss timescale and to reproduce this in our model, we have to set $\alpha_{\rm V} = 1$ (see Eq. [A.59]). This leads to a value for V_0 from the adiabatic timescale:

$$\tau_{\rm ad} = \frac{E}{\dot{E}_{\rm ad}}, \tag{5.5}$$

where $\left|\dot{E}_{\rm ad}\right| = (\nabla \cdot \mathbf{V})E_{\rm e}/3$. By using the analytical form of $(\nabla \cdot \mathbf{V})$ in Eq. (A.59) we find that $V_0 = r_0/\tau_{\rm ad}$. This is, however, not physical, if the relationship between $V(r)$ and $B(r,t)$ in Eq. (3.7) holds. From these equations it is clear that $\alpha_{\rm V} = -1$ when $\alpha_{\rm B} = 0$. The conversion efficiency (η) is very large, but there exists a degeneracy between η and L_0 and therefore this is still a preliminary value. The changes in $B(r,t)$ and $V(r)$ are the only substantial differences between the model of Torres et al. (2014) and our model. The rest of the parameters are very similar to the previous case, e.g., the indices of the injection spectrum and the soft-photon components used in the calculation of the IC spectrum.

Figure 5.3 compares our predicted SED with the model prediction of Torres et al. (2014), with their results shown by the dashed-dotted line and our model SED shown as the

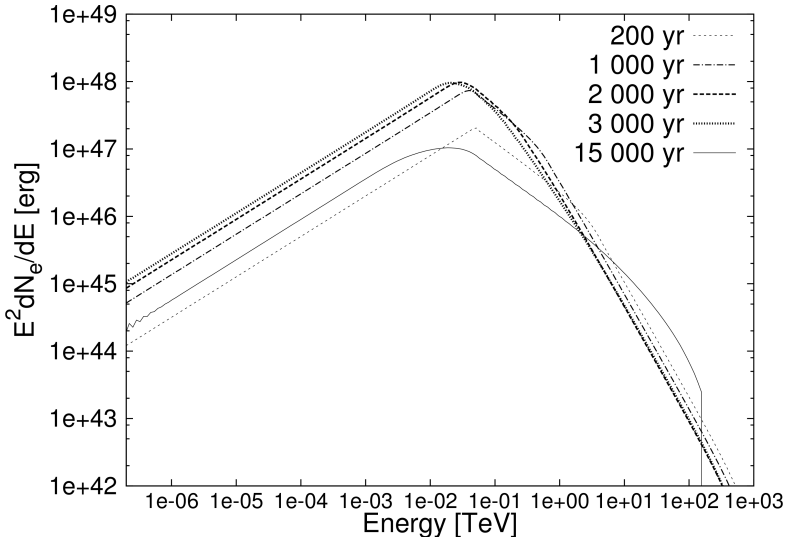

FIGURE 5.4: Time evolution of the lepton spectrum.

solid line. The differences between the two models stem from the different ways in which the transport of particles is handled. In our code we incorporated a Fokker-Planck-type transport equation and Torres et al. (2014) modelled the transport by using average timescales.

During the calibration of the code, other sources were also modelled (e.g., G21.5−0.9, G54.1+0.3, and HESS J1356−645). We found that the model yields reasonable fits for most of the chosen sources as long as they are young PWNe.

5.2 Parameter Study

The results below are highlights and updates of those presented in Van Rensburg et al. (2015) and Van Rensburg et al. (2018). We can now investigate the effects of several of the free model parameters on the predicted particle spectrum and SED. As a reference model for this section, we use the same parameters that were used in the calibration against Torres et al. (2014) for G0.9+0.1, as in Figure 5.3. The SED of the PWN is calculated at Earth for each spherical zone and these are then added to find the total flux from the PWN.

5.2.1 Time Evolution (age) of the Particle Spectrum

In Figure 5.4 the time evolution of the lepton spectrum is shown. From this figure it can be seen that when the PWN is still very young ($t_{\rm age} \sim 200$ yr) the particle spectrum closely resembles the shape of the injection spectrum apart from the spectral break at

a few TeV that develops due to radiation losses. As the PWN ages, however, it starts to fill up with particles (giving an increased $E_{\rm e}^2 dN_{\rm e}/dE_{\rm e}$) and at some stage the PWN is totally filled, at an age in the order of a few thousand years. After this the level of the particle spectrum decreases. This is due to the particles losing energy over time as a result of SR, IC, adiabatic energy losses, and escape, and also due to the fact that the embedded pulsar is spinning down, resulting in fewer particles being injected into the PWN. The effect of the spun-down pulsar can be clearly seen in Figure 5.4 by observing the spectrum at 15 000 yr. By this time the embedded pulsar has significantly spun down so that the total particle spectrum is lower than it was at $\approx$ 200 yr due to the fact that more particles are now escaping from the modelled region at $r_{\rm max}$ than being injected by the pulsar. Also note the leftward shift of both the intrinsic break energy, $E_{\rm b}$, and the spectral break at higher energies due to radiative losses. The bump at high energies for 15 000 yr is due to a pile-up of particles. This occurs due to the decreased B-field $B(t)$, resulting in an increased diffusion coefficient and also decreased SR energy losses. These losses are energy-dependent and therefore the high-energy particles will be most affected. The increased diffusion will cause the particles to resemble the injection spectrum more and more as a result of suppressed SR losses.

The particle spectrum in Figure 5.4 not only goes up and down as the PWN ages, but the whole spectrum shifts to lower energies. This can be seen by looking at where the spectrum peaks and also at the tails at high and low energies. This is because the particles lose energy through previously-mentioned mechanisms. Due to the SR energy losses, the particle spectrum will develop a high-energy break at some energy. By using $\dot{E}_{\rm SR}$ as in Eq. (4.8), we can calculate the timescale for SR losses ($\tau_{\rm SR}$) and by setting it equal to the age of the PWN ($t_{\rm age}$), one may estimate where this second break is expected in the spectrum:

$$\tau_{\rm SR} = \frac{E_{\rm e}}{\dot{E}_{\rm SR}} = t_{\rm age} \Rightarrow E_{\rm e} \propto \frac{1}{t_{\rm age}\langle B\rangle^2}. \tag{5.6}$$

Thus from Eq. (5.6) we can see that the break should move to lower energies as the PWN ages. In Eq. (5.6) we have to use the average B-field $\langle B\rangle$ over the lifetime of the PWN as the present-day B-field is too small. This is visible in Figure 5.4 where the break for 200 yr is at $\approx$ 2 TeV, for 1 000 yr at $\approx$ 0.6 TeV, for 2 000 yr at $\approx$ 0.2 TeV, and for 5 000 yr at $\approx$ 0.15 TeV. By inserting these values into Eq. (5.6) we find a reasonable value of $\langle B\rangle \sim 150$ μG. These results are similar to those found by Torres et al. (2014).

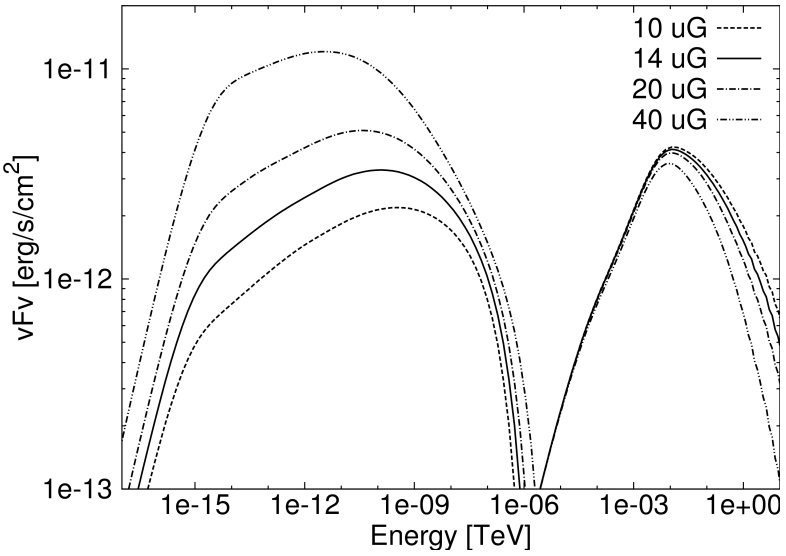

FIGURE 5.5: SED for PWN G0.9+0.1 with a change in the present-day B-field.

5.2.2 Magnetic Field and Radiation Spectra

The B-field $B(r,t)$ inside the PWN (which determines the diffusion and the SR loss rate) plays a large role in determining the shape of the SED (level and break energy of SR and IC component), and is characterised by the free parameters $B_{\rm age}$, $\alpha_{\rm B}$ and $\beta_{\rm B}$ (Table 5.2). As a default, the present-day B-field is set to 14 μG and is then changed to 10 μG, 20 μG, and to 40 μG to see what effect this will have. Here, we fix the values for $\alpha_{\rm B}$ and $\beta_{\rm B}$ to 0.0 and -1.3, respectively, as mentioned earlier, so only the value of $B_{\rm age}$ was changed (see Section 5.3.2 for a discussion on the changes in $\alpha_{\rm V}$ and $\alpha_{\rm B}$). As the B-field increases from 10 μG to 40 μG, the particle spectrum becomes softer at high energies, since $\dot{E}_{\rm SR} \propto E_{\rm e}^2 B^2$. Thus, higher-energy particles lose more energy, with the result that fewer particles at high energies are left to radiate. The high-energy tail of the IC spectrum in Figure 5.5 is therefore lower for a larger B-field. The SR power is directly proportional to the B-field strength squared and thus as the B-field increases, so does the SR component.

5.2.3 Bulk Particle Motion

The bulk particle motion (particle speed) in the PWN is modelled by Eq. (4.14) and the value for $\alpha_{\rm V} = 1$ is kept constant here, although the value of V_0 is changed to $V_0 = 0$, $2V_0$ and $V_0/2$ as can be seen in Figure 5.6 and 5.7. To compare our results with those of Torres et al. (2014) we need the same form for the bulk particle motion (see Eq. [5.5]). The adiabatic timescale that Torres et al. (2014) used for G0.9+0.1 was $\sim$ 2 000 yr, giving $V_0 = 5 \times 10^{-5}$ pc/yr for $r_0 = 0.1$ pc and $\tau_{\rm ad} = 2\,000$ yr.

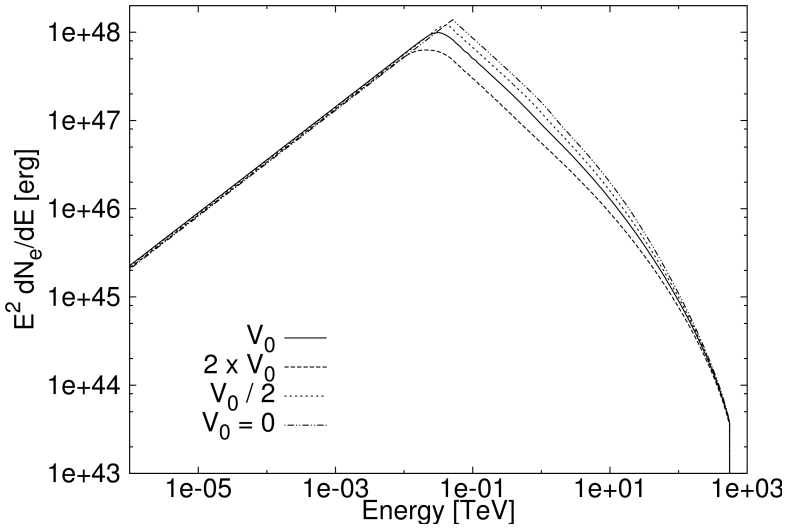

FIGURE 5.6: Particle spectrum for PWN G0.9+0.1 for a change in the bulk speed normalisation of the particles.

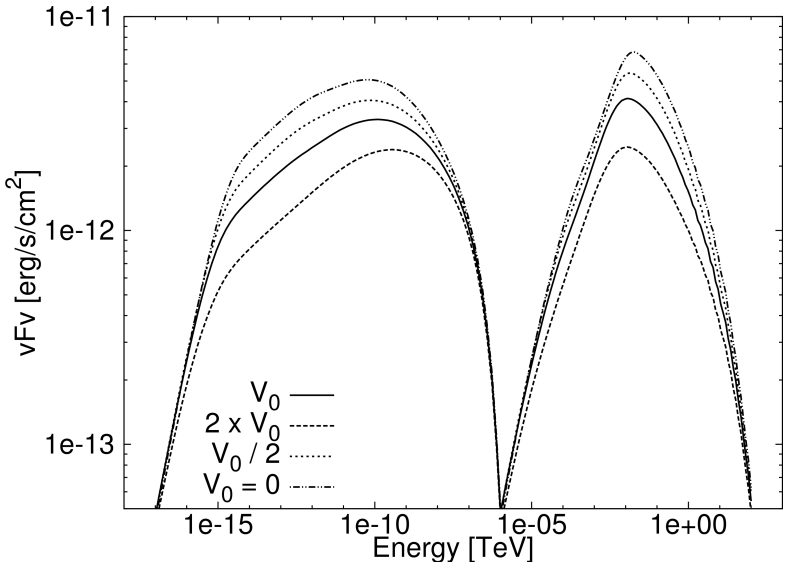

FIGURE 5.7: SED for PWN G0.9+0.1 for a change in the bulk speed normalisation of the particles.

In Figure 5.6 the particle spectrum increases as V_0 is lowered, especially at high energies. This is due to the fact that for a lower speed, the particles lose less energy due to adiabatic losses. The adiabatic energy losses also account for the leftward shift of the peak in the particle spectrum. The radiation spectrum is linked to the particle spectrum and therefore a lower particle spectrum results in a lower radiation spectrum. This effect can be seen in Figure 5.7 where the radiation decreases with an increase in the bulk speed of the particles. For high energies, SR energy losses dominate over adiabatic losses, and therefore the high-energy tail of the radiation spectrum is independent of changes in V_0 and the tails converge.

5.2.4 Injection Rate / Initial Spin-Down Rate

The particles in the PWN are injected from the embedded pulsar and the injected spectrum is normalised using the time-dependent spin-down power of the pulsar, which is given by (see Appendix A.3)

$$L(t) = L_0 \left(1 + \frac{t}{\tau_0}\right)^{-(n+1)/(n-1)} . \tag{5.7}$$

The number of injected particles is assumed to be directly proportional to this spin-down power. We can thus change L_0 to inject more or fewer particles into the PWN. If more particles are injected into the PWN, the whole particle spectrum of the PWN will increase linearly and thus also the radiation spectrum and vice versa (not shown). This change does not influence the shape of either the particle or the radiation spectrum. The same effect is seen when the value of the conversion efficiency (η) is changed [see Eq. (4.7)]. Another parameter is the characteristic spin-down timescale at birth (τ_0) given in Eq. (5.7), which characterises how fast the pulsar spins down. When this characteristic time is shorter, the pulsar spins down faster, resulting in fewer particles being injected into the PWN and thus the particle and radiation spectrum are both lower. The opposite happens when τ_0 is longer. Furthermore, the braking index n in Eq. (5.7) is usually set to 3 for rotating dipoles. If the braking index is decreased, the number of particles injected into the PWN increases due to the reduced spin-down of the pulsar (since both the index $(n+1)/(n-1)$ as well as τ_0 change). Therefore, more particles are injected for a longer period of time into the PWN. Due to this, the particle and radiation spectrum will increase with a decreased n. These effects are similar to changing the normalisation of the injection spectrum.

5.2.5 Soft-photon Fields

Table 5.2 shows the three different BB components used to model the IC scattering in the PWN. These components can be turned on and off at will, and Figure 5.8 shows the contribution of each of these components. The CMB target field produces a flat spectrum which causes the first small bump on the left-hand side of the total IC flux component. The starlight at $T = 3\ 000\ K0$, with an energy density of 25 eV/cm^3, produces the highest peak and plays the largest role in the overall IC flux. The effect of changes in the energy densities u_l and the temperatures T_l ($l = 1, 2, 3$) of the soft-photon components can be understood as follows. For a number of individual BBs, we have a

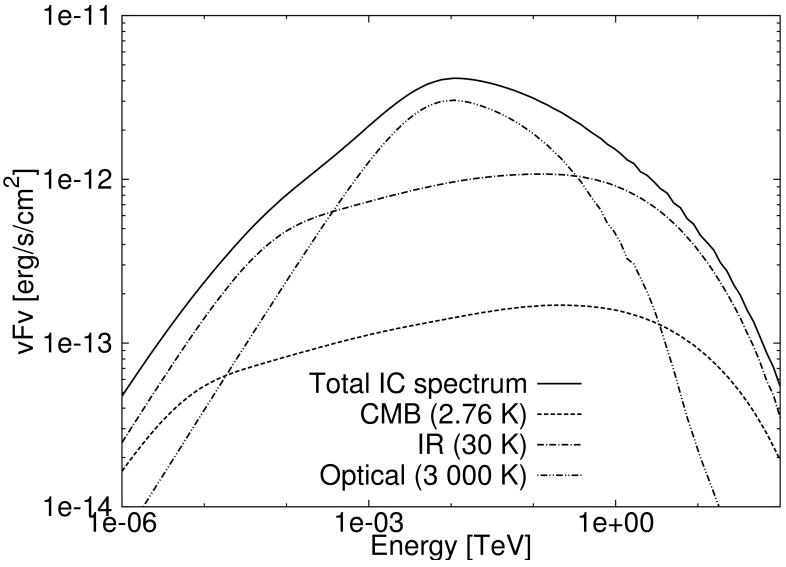

FIGURE 5.8: IC spectrum for PWN G0.9+0.1 showing the contribution of different soft-photon components in Table 5.2. The solid line is the total radiation, dashed line is the 2.76K CMB component, dashed-dotted line is the 30 K component, and the dashed-dot-dotted line shows the 3 000 K component.

spectral photon number density

$$n_\nu = \frac{8\pi\nu^2}{c^3}\frac{1}{e^{h\nu/kT_l}-1}. \tag{5.8}$$

For a given total photon energy density u_l at a particular position in the PWN, we need a number $N_{\rm BB}$ of individual black bodies at a temperature T_l to reach u_l, i.e.,

$$N_{\rm BB} = \frac{u_l}{u_{\rm BB}(T_l)}, \tag{5.9}$$

with the energy density of a single BB,

$$u_{\rm BB}(T_l) = \int u_\nu d\nu = \int h\nu n_\nu d\nu \propto T_l^4 \tag{5.10}$$

the frequency-integrated energy density of a single BB and

$$\int n_\nu d\nu \propto T_l^3. \tag{5.11}$$

Thus, the IC flux from the PWN scales as (see also Eq. (4.30), using n_ν instead of n_ε)

$$\left(\frac{dN}{dE}\right)_{\rm IC} \propto N_{\rm BB}\int n_\nu d\nu \propto \frac{u_l}{T_l}. \tag{5.12}$$

Thus, if the total energy density u_l is increased or decreased, the IC radiation will also increase or decrease linearly. However, when the temperature is increased or decreased for a constant u_l, the IC flux scales in the opposite direction. This is due to the fact

that when the temperature is increased, fewer photons are needed to reach the same energy density u_l (since the average photon energy is now larger), leading to a lower normalisation for the cumulative BB spectrum.

5.2.6 The Effect of Changing other Parameters

The effects of changing most of the major parameters have now been described, but the following are also free parameters worth noting. The free parameters α_1 and α_2 will influence the slopes and the normalisation of the particle and radiation spectrum. Lastly, the flux from the PWN at Earth scales as $1/d^2$ and the sizes of the spatial bins are also linearly dependent on d (influencing the diffusion and convection timescales for each zone), but the latter has a small effect on the emitted SED.

5.3 Spatially-dependent Results from Our PWN Model

In the previous sections, I showed the total particle spectrum and SED predicted by the code for different parameter choices. These calculations, however, were not the main aim of the code that we have developed, as we are especially interested in the spatial dependence of the radiation from the PWN. Here, I will study the effects that changing some of the parameters have on the energy-dependent size of the PWN.

5.3.1 Effects of Changes in the Diffusion Coefficient and Bulk Particle Motion on the PWN's Morphology

The diffusion coefficient contains two free parameters, which can be seen in Eq. (4.13). Here we consider the effects of changing the parameters κ_0 and q (for Bohm diffusion, $q = 1$), with E'_0 set to 1 TeV (changing E'_0 is equivalent to changing κ_0). We can now increase or decrease the value of κ_0 (assuming it is not linked with the magnitude of the B-field) and thus change the normalisation of the diffusion coefficient. We can also change q which has an influence on the energy dependence of the diffusion coefficient.

Figure 5.9 shows how the size of the PWN changes with energy for three different scenarios. (As a reminder, the size of the PWN at a specific energy is determined by observing where the SB profile at that energy has decreased by a factor two-thirds with respect to its value in the first spatial bin 2/3.) The thin solid lines indicate $5\kappa_0$, the thick solid lines indicate κ_0, and the dashed lines indicate $\kappa_0/5$. The left graphs show SR and the right graphs IC emission. For this set of scenarios the size of the PWN increases with increased energy. In the first two scenarios, diffusion dominates the

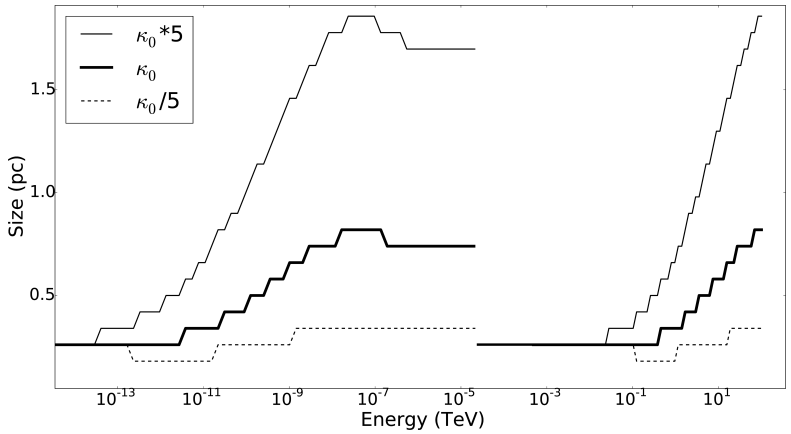

FIGURE 5.9: Size of the PWN as a function of energy when the normalisation constant of the diffusion coefficient is changed.

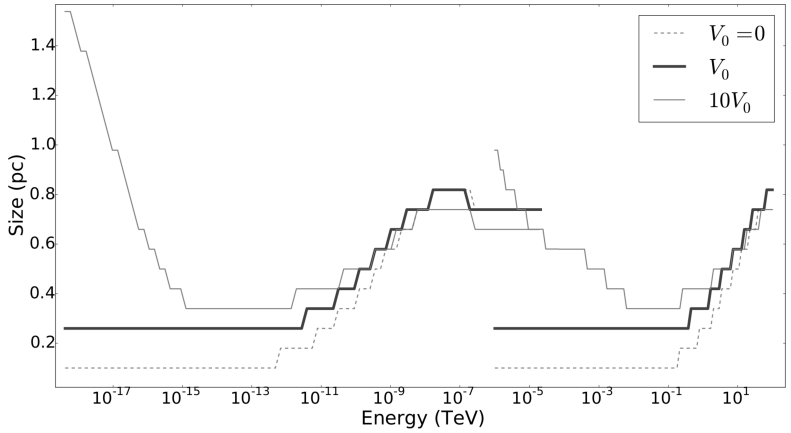

FIGURE 5.10: Size of the PWN as a function of energy for different normalisations of the bulk particle speed for the model parameters given in Table 5.2.

particle transport and causes the high-energy particles to diffuse outward faster than low-energy particles, filling up the outer zones and resulting in a larger size for the PWN at high energies. This effect is larger for high-energy particles due to the energy dependence of the diffusion coefficient ($q > 0$). For $\kappa_0/5$, we see that the effect is not as pronounced. Here the diffusion coefficient is so small that the SR energy loss rate starts to dominate diffusion. The particles therefore "burn off" or expend their energy before they can reach the outer zones. Changes to q have similar effects on the SED than changes to κ_0 but are more pronounced at higher energies.

Next we studied the effect of varying the normalisation of the bulk motion at r_0 on the energy-dependent size of the PWN by varying V_0 for two different cases: the first as seen in Figure 5.10 is for the model parameters given in Table 5.2, while the second as seen in Figure 5.11 is for the parameters given in Table 5.3. If we consider $V_0 = 0$ (Figure 5.10), indicated by the dashed line, we find that the size of the PWN is determined by the energy-dependent diffusion and therefore the size increases with increasing

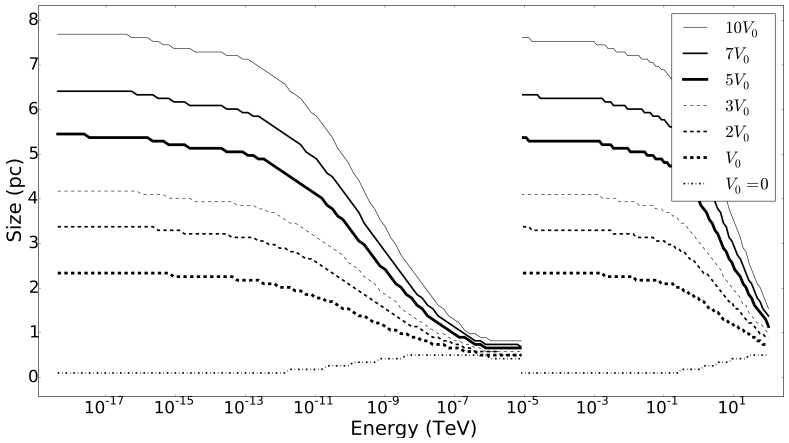

FIGURE 5.11: Size of the PWN as a function of energy for different normalisations of the bulk particle speed for the model parameters given in Table 5.3.

energy. Adding a bulk flow to the code (e.g., non-zero V_0, thick solid line) increases the size of the PWN irrespective of the energy of the particles. However, for a very large bulk flow speed (e.g., $10V_0$, thin solid line), the radio size is significantly larger than the X-ray size. This is due to the energy-dependence of the SR energy losses which dominate at higher energies, thereby reducing the lifetime of these X-ray-emitting particles and resulting in a smaller source compared to the radio. In this first case $\alpha_{\rm V} = 1$, which is non-physical as mentioned in the discussion following Eq. (5.5). The bulk flow speed becomes so large in the outer zones that particle escape becomes significant. Therefore, if the normalisation is increased beyond $10V_0$, the radio source size in fact starts to decrease.

Next we do a similar study by using the more physical set of parameters given in Table 5.3, where $\alpha_{\rm V} = -1$. Figure 5.11 shows the effect of changes to the normalisation of the bulk motion of particles by increasing it incrementally whilst keeping the magnetic field constant at all positions ($\alpha_{\rm B} = 0$). Again, if $V_0 = 0$ (dashed-dotted line, same line as in Figure 5.10), the PWN has a smaller size at lower energies than at higher energies. The size increases monotonically with V_0. At the lower energies convection dominates the radiative energy losses and therefore the particles have a very long lifetime, allowing them to diffuse to the outer zones and still able to radiate, resulting in a large source size. In contrast to this, at high energies, the SR losses dominate the convection, resulting in a very short lifetime for the high-energy particles. These particles radiate all their energy before they have time to convect to the outer zones. This leads to a relatively smaller X-ray source size.

A similar exercise can be performed to view the impact that the normalisation of the bulk motion (V_0) and diffusion coefficient (κ_0) has on the SB profile and the spectral index as a function of distance from the central pulsar. PWN G0.9+0.1 was once again

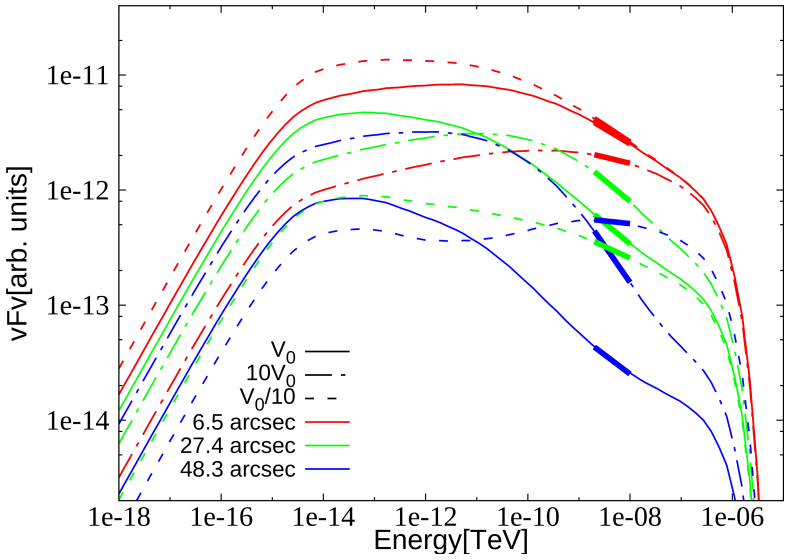

FIGURE 5.12: SR component of the SED for PWN G0.9+0.1 for three different normalisations of the bulk motion (V_0) of the particles with a power-lab fit in the $2.0-10.0$ keV energy range indicated by the thicker lines. The solid lines show the SR spectrum for V_0 with the dashed lines indicating $V_0/10$ and the dashed-dotted lines the spectrum for $10V_0$. The different colours indicate the spectrum in the first three LOS-integration radii. Note the arbitrary units here as the flux for $V_0/10$ for the farther-out zones is orders of magnitude smaller and is increased to allow comparison with fluxes of other V_0 choices.

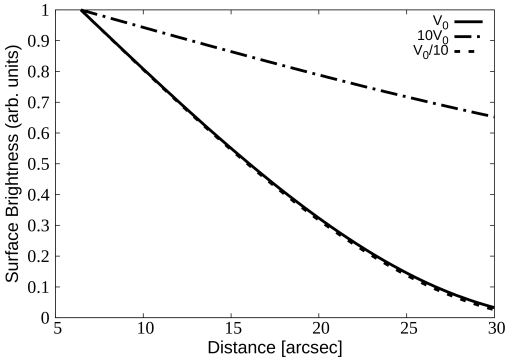

FIGURE 5.13: SB profile for PWN G0.9+0.1 for three different normalisations of the bulk motion of the particles in the $2.0-10.0$ keV energy range.

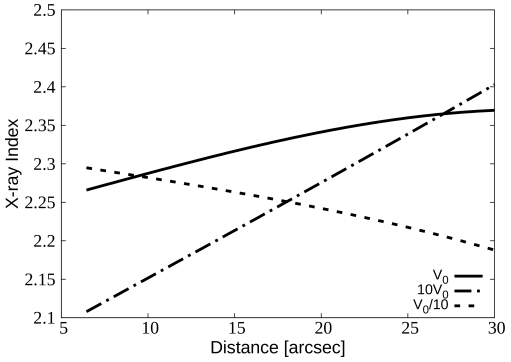

FIGURE 5.14: Spectral index for PWN G0.9+0.1 for three different normalisations of the bulk motion of the particles in the $2.0-10.0$ keV energy range.

used and the $2.0-10.0$ keV energy range was chosen to calculate the SB and spectral index profiles. Figures 5.12 and 5.15 show the SR spectrum for the two different cases mentioned above, with the thicker lines indicating a power-law fit in the $2.0-10.0$ keV energy range.

Changes to the normalisation of the bulk motion (V_0) of the particles: Figure 5.12 shows the SR spectrum when changing the normalisation of V_0. When observing the first zone (red lines), one can see that as V_0 increases (dashed-dotted line) from its default

value the spectrum reduces, implying fewer particles in the first zone and when V_0 decreases (dashed line) the spectrum increases (but softens) indicating more particles are in the first zone. The opposite is seen in the second zone (blue lines) where a larger V_0 results in an increase in the spectrum and a smaller V_0 results in large reduction in the spectrum ($V_0/10$ is increased to allow for comparison). This effect is more clearly seen in Figure 5.13 that shows how the SB profile changes as the normalisation of the bulk motion changes. For a larger normalisation (dashed-dotted line) the SB does not fall as rapidly as for a slower bulk motion. If the particles have a larger bulk motion then they are able to move to the outer zones before losing a significant amount of energy due to SR losses. This results in a larger source (flatter SB profile). If the opposite is the case ($V_0/10$), then the SR loss timescale dominates the convection timescale and therefore particles lose their energy before they have time to traverse to the outer zone, resulting in a smaller source (steeper SB profile). In this case the effect is smaller than for the $10V_0$ case due to diffusion dominating the motion of the particles for such a slow bulk motion. Understanding the X-ray photon index is more complicated. However, by comparing Figure 5.12 and Figure 5.14 closely, one can understand this behaviour. For example, a slower V_0 may seem to result in particle acceleration (flatter spectral index) if one observes Figure 5.14 in isolation, but this is not the case. In Figure 5.12 a power-law fit is indicated by the thicker lines in the $2.0 - 10.0$ keV energy range and here we can see that if V_0 is slower then the spectrum reduces in the farther-out zones, but it is not the high energy part of the spectrum that increases but the lower-energy part of the spectrum that reduces.

Changes to the normalisation of the diffusion coefficient (κ_0) of the particles: The κ_0 acts in a similar fashion as the bulk motion of the particles with the exception that the diffusion of the particles is energy-dependent and the convection of particles not. This effect can be seen in Figure 5.15 where changes to κ_0 primarily affects the high-energy part of the SR spectrum. As before (with V_0) a larger diffusion results in fewer particles in the first zone but more in the next couple of zones and the opposite is true for a smaller κ_0. The effect with a smaller κ_0 is, however, very small as the motion of the particles is dominated by convection in this case and therefore reducing κ_0 more does not have a big effect on the spectrum. Figure 5.16 emphasises this by showing how the SB profile changes as the normalisation of the diffusion coefficient changes. As mentioned, for a larger diffusion coefficient (dashed-dotted line) the particles move faster to the outer zones resulting in a larger source size. This is due to the diffusion timescale dominating the SR loss timescale. For lower diffusion normalisation (dashed line) the SR loss timescale dominates the diffusion timescale resulting in a slightly steeper SB profile. This slight change is due to the diffusion timescale being dominated by the convective timescale. Figure 5.17 shows the spectral index as function of radial distance

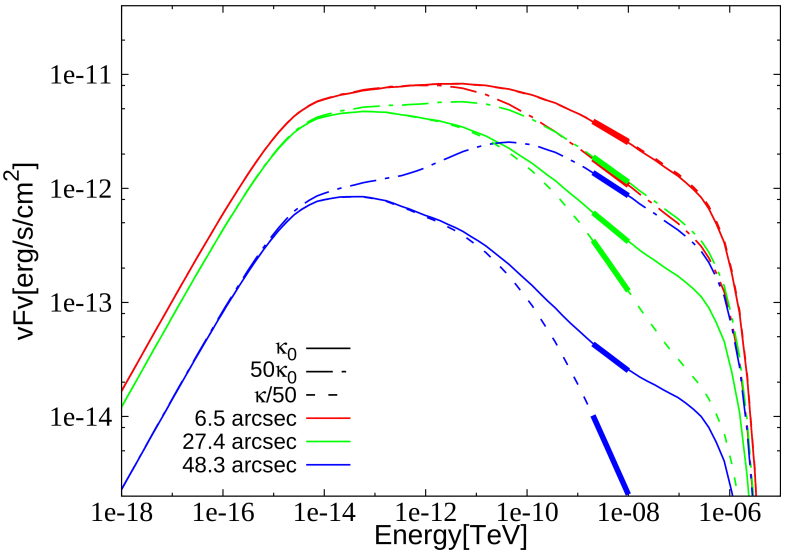

FIGURE 5.15: SR component of the SED for PWN G0.9+0.1 for three different normalisations of the diffusion coefficient (κ_0) of the particles with a power-lab fit in the $2.0 - 10.0$ keV energy range indicated by the thicker lines. The solid lines show the SR spectrum for κ_0 with the dashed lines indicating $\kappa_0/50$ and the dashed-dotted lines the spectrum for $50\kappa_0$. The different colours indicate the spectrum in the first three LOS-integration radii.

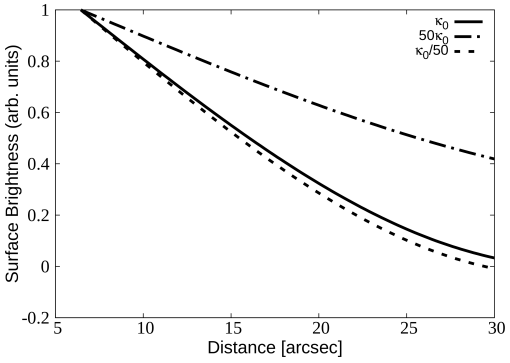

FIGURE 5.16: SB profile for PWN G0.9+0.1 for three different normalisations of the diffusion coefficient of the particles in the $2.0 - 10.0$ keV energy range.

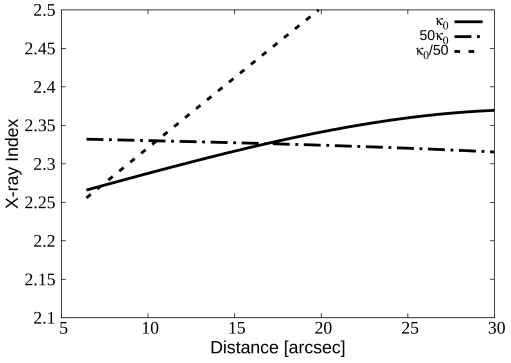

FIGURE 5.17: Spectral index for PWN G0.9+0.1 for three different normalisations of the diffusion coefficient of the particles in the $2.0 - 10.0$ keV energy range.

from the central pulsar. Here we see that for slow diffusion (dashed line) the particles responsible for the high-energy part of the SR spectrum has lost their energy due to the dominance of the SR loss timescale resulting in a great increase in the photon index as one moves farther away from the central pulsar. Faster diffusion (dashed-dotted line) primarily influences the SB profile and has a very small effect on the photon index.

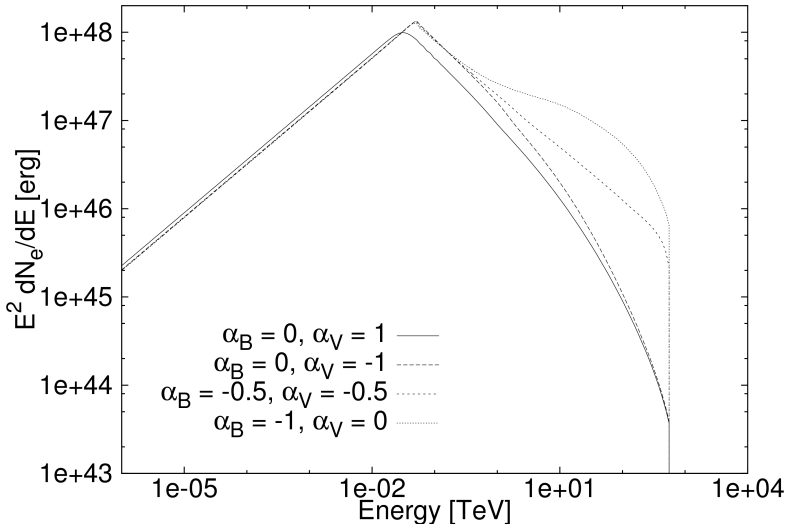

FIGURE 5.18: Particle spectrum for PWN G0.9+0.1 with a change in the parametrised B-field and bulk particle motion.

5.3.2 Different Cases of α_V and α_B

In Eq. (4.14) and Eq. (4.17), I assumed that the B-field may have a spatial and time dependence and that the bulk motion only has a spatial dependence. In this section the effects of different spatial dependencies for $B(r,t)$ and $V(r)$ are studied. Note that we have assumed the diffusion coefficient to be spatially independent throughout this work. However, since I am now considering the spatial dependence of the B-field in this paragraph, and $\kappa \propto 1/B(r,t)$, this assumption is technically violated here. The effect is small when the divergence of $\vec{\kappa}$ is small, which I assume to be the case in this section. This spatial dependence of the diffusion coefficient can be implemented in future by adding another convective term to the transport equation.

From Eq. (3.7), the following relationship is assumed to hold: $\alpha_V + \alpha_B = -1$. For this section the time dependence of the B-field is kept unchanged, with $\beta_B = -1.3$, and four different scenarios for α_B and α_V are shown. Here the first situation is the same as Torres et al. (2014), with $\alpha_B = 0$ and $\alpha_V = 1$. We also considered the following three situations: $\alpha_B = 0$ and $\alpha_V = -1$, $\alpha_B = -0.5$ and $\alpha_V = -0.5$, and $\alpha_B = -1$ and $\alpha_V = 0$. These three situations all comply with Eq. (3.7), with the B-field kept constant in the first spatial zone. The B-field was limited to a maximum value there to prevent the parametrised B-field growing infinitely large during the early epochs of the PWN's lifespan.

In Figure 5.18 the particle spectrum is shown for the four different scenarios, with the solid line showing the result for $\alpha_B = 0$ and $\alpha_V = 1$ as is effectively assumed by Torres et al. (2014). In this case the B-field is spatially constant over the entire PWN, but the bulk speed increases linearly with r. The particles move extremely fast as they

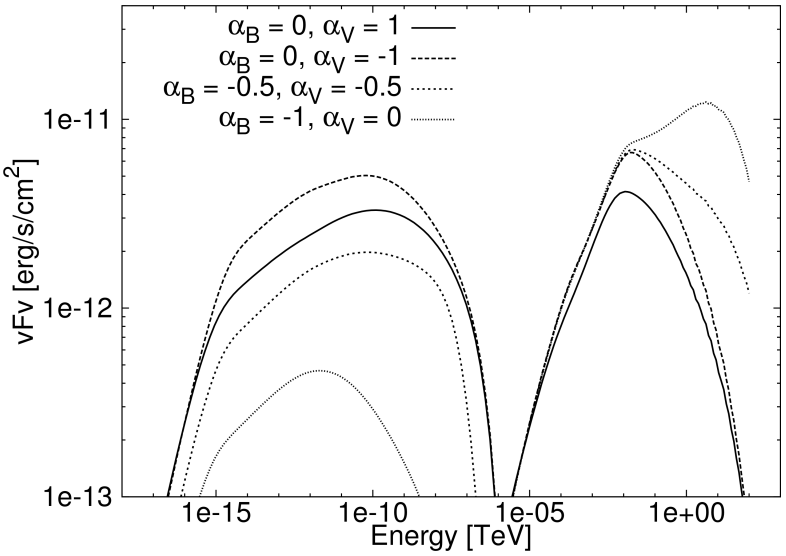

FIGURE 5.19: SED for PWN G0.9+0.1 with a change in the parametrised B-field and bulk particle motion.

propagate farther from the centre of the PWN. They therefore lose more energy due to adiabatic energy losses relative to the other cases. Thus, the solid line is lower than the other situations and the peak of the spectrum is also shifted to the left.

We can see from both figures 5.18 and 5.19 that changes to the B-field have a more profound impact on the particle spectrum and SED than changes to the radially-dependent speed. If the spatial dependence of the B-field changes from $\alpha_B = 0$ to $\alpha_B = -0.5$ and to $\alpha_B = -1$, the B-field is first constant over all space and then decreases as $r^{-0.5}$ and finally it reduces rapidly as r^{-1}. The effect of this can be seen in the particle spectrum as the number of high-energy particles increases for a decreased B-field and hence a lower SR loss rate. This effect is emphasised in the situation where $\alpha_B = -1$, resulting in a very small B-field at the outer edges of the PWN. This can also be seen in the radiation spectrum in Figure 5.19 where a decreased B-field results in reduced radiation in the SR band (since $\dot{E}_{SR} \propto B^2$), and the increased radiation in the IC band is due to more particles being present at those energies. This increase in the high-energy particles is quite large for $\alpha_B = -1$, though (possibly indicating a violation of our assumption that the divergence of $\vec{\kappa}$ is small in this case).

We note that our model currently does not take into account the fact that the cutoff energy due to particle escape (E_{max}) should also be a function of the B-field. This is because in reality $\sigma \propto B^2$ (we have assumed σ to be constant and small), and therefore $E_{max} \sim \sqrt{B^2/(1+B^2)}$, which will have the effect that if the B-field is reduced, σ and therefore E_{max} will decrease. This may cause the high-energy particles to be cut off at lower energies as the B-field decreases due to more efficient particle escape, and therefore the build-up of high-energy particles may be partially removed (we say 'partially' since

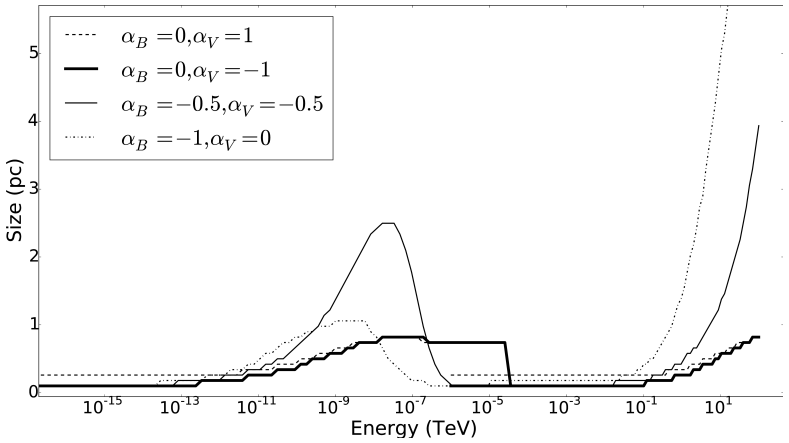

FIGURE 5.20: Size of PWN G0.9+0.1 as a function of energy for changes in α_{B} and α_{V}.

the Larmor radius of the most energetic particles in the outer zones is still smaller than the PWN size by a factor of a few, inhibiting efficient escape of particles from the PWN). The question of particle escape may also be addressed by refining our outer boundary condition in future.

From Figure 5.20 we can see that in scenario one (dashed line, $\alpha_{\mathrm{B}} = 0$ and $\alpha_{\mathrm{V}} = 1$) the PWN size for low energies is always larger than for all the other scenarios. This is due to the bulk speed being directly proportional to r in this case, resulting in the particles moving faster as they move farther out from the centre of the PWN. This will result in the outer zones filling up with particles, while not escaping. This may point to our outer boundary that was chosen to be much larger than the radius of the PWN ($r_{\mathrm{max}} \gg R_{\mathrm{PWN}}$). For scenario two (thick solid line, $\alpha_{\mathrm{B}} = 0$ and $\alpha_{\mathrm{V}} = -1$), the size of the PWN at low energies follows the same pattern as for both low-energy and high-energy photons, since the energy-dependent diffusion now dominates convection. At lower energies, we see that PWN is smaller than in scenario one, as the speed is now proportional to r^{-1}, which results in a slower bulk motion and thus fewer low-energy particles moving to the outer zones. In scenario three, (thin solid line, $\alpha_{\mathrm{B}} = -0.5$ and $\alpha_{\mathrm{V}} = -0.5$), and four (dotted line, $\alpha_{\mathrm{B}} = -1$ and $\alpha_{\mathrm{V}} = 0$) the B-field has a spatial dependence, reducing as one moves farther away from the centre of the PWN. This reduced B-field will lead to increased diffusion and decreased SR losses as mentioned in the first part of this section. For these two scenarios the dependence of the bulk motion on radius is weaker and therefore diffusion dominates the particle transport. Once again we can see the energy dependence of the diffusion, since the PWN is initially smaller and then increases for higher energies. At very high energies, the PWN size becomes very large, which is not the case for the SR component. The first is due to the pile up of high-energy particles (leading to substantially increased IC emission, Figure 5.19), while the second is due to the fact that SR is severely inhibited for the very low B-field.

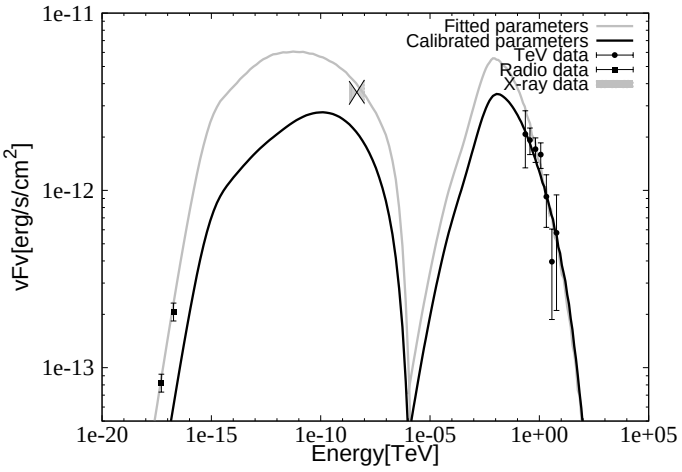

FIGURE 5.21: The black line indicates the SED for PWN G0.9+0.1 for the parameters used by Torres et al. (2014) (Table 5.2) and the grey line shows the fitted parameters as in Table 5.3. The radio (Helfand and Becker, 1987), X-ray (Porquet et al., 2003) and gamma-ray data (Aharonian et al., 2005) are also shown.

TABLE 5.3: Modified parameters for PWN G0.9+0.1 for fitting the SED as well as the energy-dependent size of the PWN.

Model Parameter	Symbol	Value	Torres et al. (2014)
Present-day B-field	$B(t_{\rm age})$	16.0 μG	14.0 μG
Age of the PWN	$t_{\rm age}$	3 227 yr	2 000 yr
Initial spin-down power (10^{38}erg s^{-1})	L_0	1.44	1.0
B-field parameter	$\alpha_{\rm B}$	0.0	0
B-field parameter	$\beta_{\rm B}$	-1.0	-1.3
V parameter	$\alpha_{\rm V}$	-1.0	1.0
Particle bulk motion	V_0	0.062 c	$1.63 \times 10^{-4} c$
Diffusion	κ_0	3.4	1.0

5.3.3 Size versus Energy fits

Figures 5.21 and 5.22 show the radiation spectrum and the size versus energy graphs for PWN G0.9+0.1 for the calibration parameters (solid black lines) as in Table 5.2 modelled by Torres et al. (2014), with the dots indicating the radio and the square the X-ray sizes. The upper limit on the predicted TeV size is 10.4 pc, i.e., we use the point spread function of the H.E.S.S. telescope (not shown). The radio data are from Helfand and Becker (1987) and Dubner et al. (2008), the X-ray data are from Porquet et al. (2003), and the TeV data from Aharonian et al. (2005). The model provides reasonable fits to the spectral radio, X-ray, and TeV data; however, it is clear that the predicted size of the PWN does not fit the data at all. After adjusting some parameters, we found a better fit and this can also be seen in Figure 5.21 and 5.22 (grey lines). Table 5.3 shows the new parameters used for this fit.

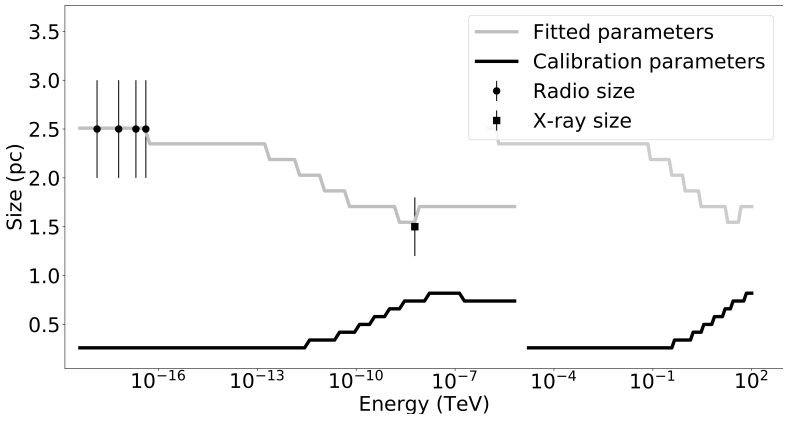

FIGURE 5.22: Size of the PWN as a function of energy for the calibration parameters in Table 5.2 (black line) and the fitted parameters in Table 5.3 (grey line). The observed radio (Dubner et al., 2008) and X-ray sizes (Porquet et al., 2003) are also indicated.

The process of finding a better fit to the both the SED of the PWN and the energy-dependent size was facilitated by our prior parameter study. The only way in which we could increase the size of the PWN at lower energies was to increase the bulk speed of the particles. Increasing the bulk speed, however, increased the adiabatic energy losses, and resulted in a lower radiation spectrum. This was then countered by increasing the age of the PWN (which effectively leads to an increase in L_0). The bulk speed of the particles had to be increased substantially to fit the data, but given the large errors on the size of the PWN in the radio band, we could still fit the data with a bulk speed as small as $0.073c$. The profile trends for the B-field as well as the bulk speed of the particles ($\alpha_{\rm B}$ and $\alpha_{\rm V}$) were also changed. To increase the size of the PWN further we also increased the normalisation of the diffusion coefficient of the particles. This is not a bad assumption as the diffusion was originally modelled to be Bohm-type diffusion, which is a very slow perpendicular diffusion with respect to the B-field. All these changes produced the grey lines in Figure 5.21 and 5.22. Here we see that we have a good fit for the radio size, which according to data, does not change with energy and the model reproduces this trend as well as the trend where the size of the PWN decreases with increasing energy. This is a common feature of PWNe. We do, however, realise that the SB profile is more fundamental than the energy-dependent size since the latter derives from the first and therefore the SB profile is used in Chapter 6 to find best fits of the model to the available data.

5.4 Summary

In this chapter I have showed that our developed model from Chapter 4 calibrates well with the results from other authors. The parameter study in the second part of this

chapter is a powerful tool as it empowers us to make logical and reasonable predictions when trying to fit the new model to three sources as will be shown in the next chapter.

Chapter 6

Results

In this Chapter I show the main results from this study by first discussing the methods used to find concurrent best fits of the model to three data sets, and then describing these best fits for three different sources (Van Rensburg et al. submitted).

6.1 Methods for Finding Best fits

The data sets (broadband SED, SB profile and X-ray photon index vs. radius) we use to constrain our spatial model are statistically heterogeneous. This causes some sets to dominate[1] others when inferring best-fit parameters, which may be due to the subsets having different numbers of data points (compare, e.g., the number of points in the SED vs. that of the spectral index profile), or to a discrepancy in respective relative errors, resulting in χ^2 values that differ substantially between subsets. Thus, we decided to investigate different fitting methods to find best fits to the respective data sets associated with each PWN we considered. In this section, three different fitting methods are discussed. We hope to break degeneracies in our model by considering different effective weightings of each data subset, while also testing a new type of statistic not previously used for PWN codes.

The first and most basic method[2] is using trial and error and knowledge (intuition) of the code's behaviour upon changing parameters, using by-eye fitting to find a best model fit. This is a viable method, but is subjective and limited to the time available and resolution of searching, given a large parameter space. The uniqueness of the resulting

[1] The χ^2 values of data sets with various different errors may vary substantially resulting in some data sets to be preferred by optimisations schemes.

[2] This is strictly not a formal fitting method, but rather, we use this as a sanity check and a basis for comparison with results from other fitting methods.

best fit, and whether it is truly optimal, are also unknown. During this procedure, the parameters are changed more or less at the same time. A test was done to find best fits following different orders of changing the free parameters. However, this did not have any effect on the final best-fit parameters, since one has to change the parameters nearly simultaneously to find any sort of best fit, even when starting with different initial parameters. We thus conclude that our by-eye fitting procedure is robust, even if it is subjective. This makes for a good starting point for all the sources we modelled and we indicate these fits using black lines below.

The next way of finding a best fit is to perform a Pearson's χ^2 test (Bevington, 1969). By calculating the test statistic

$$\chi^2 = \sum_i \left(\frac{D_i - M_i}{\epsilon_i} \right)^2 , \tag{6.1}$$

with D_i the data point, ϵ_i the error and M_i the model value corresponding to the ith bin, and minimising this value over all free model parameters, one can find a best fit by combining the χ^2 values for all the subsets (usually biased by one particular data subset), and minimising this composite quantity. Examples of this methodology are afforded by Porth et al. (2016), who used a Nelder-Mead minimisation method coupled to a χ^2 test statistic to find optimal parameters for their transport code when applying their model to three PWNe (fitting SB profiles and X-ray photon spectral index profiles). Similarly, Lu et al. (2017a) applied their model to PWN 3C 58, PWN G21.5−0.9 and PWN MSH 15−52, using a χ^2 method to first fit the SED and then predict the spatial behaviour of each source based on the best-fit parameters found using only the SED. Since we are not only fitting a single data set, we calculate the χ^2 value for each of the subsets and then minimise the sum to find the best possible fit (as shown by the red lines in the figures below). This method seems to work reasonably well.

We find, however, that the heterogeneous nature of the data subsets implies that some subsets will dominate when using a standard χ^2 test statistic. To ameliorate this, we tested a new best-fit method (A.S. Seyffert et al., in preparation) originally developed for dual-band pulsar light curve modelling, where the relative radio errors are usually much smaller than that of the γ-ray band (Bezuidenhout et al., 2017). The scaled-flux-normalised (SFN) test statistic χ^2_Φ is a modified χ^2 statistic better suited to handle multiple, statistically heterogeneous, binned data sets. The χ^2_Φ statistic attempts to eliminate the dominance of certain data subsets by effectively rescaling the goodness-of-fit measure of each subset such that it reflects how well the model reproduces large-scale trends in the data, rather than how much the model deviates from the data points in terms of the data errors (as is done by the traditional χ^2 method). This can be done by considering a particular data set to be a perturbation above some background level

$\boldsymbol{B}$ and calculating the scaled flux $\Phi^2 = \chi^2(\boldsymbol{B})$ for each data subset. The latter is essentially the normal χ^2 value for the background level. Choosing background levels is a bit problematic, but we used the following values during this initial application of the new method: 0.01 of the SED level, $\Gamma = 3.0$ for the X-ray index background value and a constant value of 0.01 for the SB background level. Fortunately, different choices in background level did not significantly affect our best-fit values. The SFN test statistic is then defined as

$$\chi^2_\Phi(\boldsymbol{M}) \equiv \frac{\Phi^2 - \chi^2(\boldsymbol{M})}{\Phi^2 - \nu}, \tag{6.2}$$

where $\boldsymbol{M}$ is a given model prediction and ν is the number of degrees of freedom associated with the fit in that data subset's domain. For a model with n_p parameters being fit to a data set with n bins, $\nu = n - n_\mathrm{p}$. Eq. (6.2) will typically yield a value between 0 and 1, with 0 meaning the fit is as good as if the background were our model (i.e., no source present) and 1 meaning that it is within 1σ from the data. Values outside this range are also possible, with $\chi^2_\Phi > 1$ indicating that the errors were over-estimated (i.e., overfitting) and $\chi^2_\Phi < 0$ indicating that the model fit was worse than a flat model at the background level. These two values are equivalent in meaning to having $\chi^2 < \nu$ and $\chi^2 > \Phi^2$ (the latter usually corresponding to $\chi^2/\nu \gg 1$). When fitting three data subsets concurrently, we calculate the average of the three SFN values and maximise this to find the best possible fit. Our results using this method are indicated by the blue lines in figures 6.2 to 6.12.

Another idea that we tested to find optimal concurrent fits was to introduce a free nuisance parameter to optimise the amplitude of the SB as in figures 6.3, 6.6 and 6.11, since only the overall SB profile shape is modelled and not the absolute SB values. However, this did not yield significantly improved fits and therefore we did not implement this in our final fitting method. Furthermore, we previously showed that our code is able to predict the size of the PWN as a function of energy (Van Rensburg and Venter, 2019). However, since the sizes are directly derived from the SB profiles for different energy bands, this size vs. photon energy output is not an independent observable. We thus decided to only fit the SB profiles and not additionally the size vs. energy, since the first are more fundamental and the second should directly derive from them.

Using the methods and types of data sets described above, we found suitable fits to the observed data of three PWNe, as discussed in the next section. In tables 6.1 to 6.3 the last three rows indicate that the optimal model parameters have been found using either the χ^2 or χ^2_Φ test statistic. The corresponding values of the same test statistic (per row), using best-fit parameters preferred by the other search methods, are shown for comparison.

6.2 Fitting of Sources

We use PWN 3C 58, PWN G21.5−0.9 and PWN G0.9+0.1 as case studies. This choice of sources is due to the availability of radial data in the X-ray regime as well as existing modelling efforts by independent authors with which to compare our results with (e.g., Slane et al., 2004, Matheson and Safi-Harb, 2005, Holler et al., 2012a). For a more direct comparison we note that Lu et al. (2017c) predict the SED and X-ray photon index vs. radius for PWN 3C 58 and PWN G21.5−0.9, but not the SB profile; they did, however, predict all three of these observables for PWN MSH 15−52 (Lu et al., 2017a). We found reasonable fits to the available spatial and spectral data. Figures 6.2 to 6.4 show the results for PWN 3C 58, while figures 6.5 to 6.7 do the same for PWN G21.5−0.9 and figures 6.10 to 6.12 for PWN G0.9+0.1.

In order to make our investigation tractable in terms of computational facilities and available time, we freed the following five model parameters: the current-day magnetic field strength ($B_{\rm age}$), the bulk flow normalisation of particles (V_0), the age of the system ($t_{\rm age}$), the magnitude of the diffusion coefficient (κ_0) and the radial profile of the magnetic field ($\alpha_{\rm B}$). These parameters have the most significant influence on the radial properties of the PWN. As noted in Chapter 4, the magnetic field's radial profile and the bulk motion of the particles' radial profile are coupled ($\alpha_B + \alpha_V = -1$). The bulk-flow normalisation is therefore an independent parameter, but the bulk-flow profile is dependent on the choice of magnetic field profile. Below, we discuss each of the modelled sources individually as each of them posed their own unique challenges. In each of these fitting attempts we only specify the best-fit values of the free parameters and not the errors or error contours on these parameters. This is because a full Markov-Chain Monte Carlo (MCMC) approach (based on maximising the likelihood) requires substantial, even prohibitive computational resources. However, we did perform an MCMC procedure for a very crude (but still reasonable) spatial and energy resolution to study this issue in some more detail, and considered two cases. For the first case, we invoked very large ranges in the flat priors for our free parameters, finding several local maxima and very broad contours, but with one global maximum being preferred. This illustrates that one generally cannot simply quote linear (asymmetric) errors on free parameters in the tables below, since the contours are disconnected and encompass several maxima. In the second case, we zoomed into the parameter space by bracketing the priors around the best-fit parameters, finding that while the local maxima contours seem reasonable, in some cases physical limits have to be imposed such as a non-zero diffusion coefficient or bulk speed that does not exceed the speed of light. This illustrates the difficulty in estimating reasonable parameter errors, but also point to the fact that ideal (physically

acceptable) fits that can concurrently reproduce all available data may not exist within the current model's parameter space.

6.2.1 PWN 3C 58

Weiler and Seielstad (1971) discovered PWN 3C 58 and originally classified it as an SNR, but later radio observations by Weiler and Panagia (1978) showed a bright, centre-filled morphology as well as a flat radio spectrum leading to its reclassification as a PWN. Several decades later an associated pulsar, PSR J0205+6449, was discovered by Murray et al. (2002), having a rotational period of 65 ms and a spin-down luminosity of 2.7×10^{37}erg s^{-1}. Subsequent X-ray observations (Slane et al., 2004) have shown filaments and knots that closely resemble those seen in the Crab Nebula and therefore PWN 3C 58 is characterised as being "Crab-like". Roberts et al. (1993) derived a distance of 3.2 kpc which we will use throughout this paper, while Tanaka and Takahara (2013) suggest a closer distance of 2.0 kpc. The X-ray SB and radial photon index vs. radius were taken from Slane et al. (2004) as shown in figures 6.3 and 6.4. Abdo et al. (2013) observed PWN 3C 58 with *Fermi-LAT* and detected a spectrum extending past 100 GeV, having a power-law spectral index of $\Gamma = 1.61 \pm 0.21$ with a flux of $(1.75 \pm 0.68) \times 10^{-11}$erg cm^{-2}s^{-1}. VHE data for PWN 3C 58 were obtained from Aleksić et al. (2014). During their observations with MAGIC in the energy range between 400 GeV to 10 TeV they observed a flux of $(2.0 \pm 0.4_{\mathrm{stat}} \pm 0.6_{\mathrm{sys}}) \times 10^{-13}$cm^{-1}s^{-1}TeV^{-1} which is one of the lowest PWN flux measured to date. The spectrum is well described by a power-law function with $\Gamma = 2.4 \pm 0.2_{\mathrm{stat}} \pm 0.2_{\mathrm{sys}}$. For more information regarding 3C 58 also see Li et al. (2018).

Figure 6.1 shows the timescales of different processes in the PWN model. This is only shown for PWN 3C 58 to assist in the discussion, but is similar for the different modelled sources. Here $\alpha_{\mathrm{B}} = 0$, implying a constant magnetic field vs. radius. This is an assumption made throughout the paper and is discussed in the next paragraph. From Figure 6.1 we can clearly see that the escape timescale (τ_{esc}) is the shortest for all radii and all time for lower particle energies ($E_{\mathrm{e}} < 1$ erg), indicating that such particles will generally leave the current zone in the model before losing a substantial amount of energy due to radiation losses. For energies $E_{\mathrm{e}} > 1$ erg the SR energy-loss timescale (τ_{SR}) starts to dominate. These two effects influence the radial predictions from the code most significantly. The associated model quantities are the magnetic field (directly influencing τ_{SR}) and the normalised bulk flow of particles (determining the time spent in each zone by the particles, thus τ_{esc}).

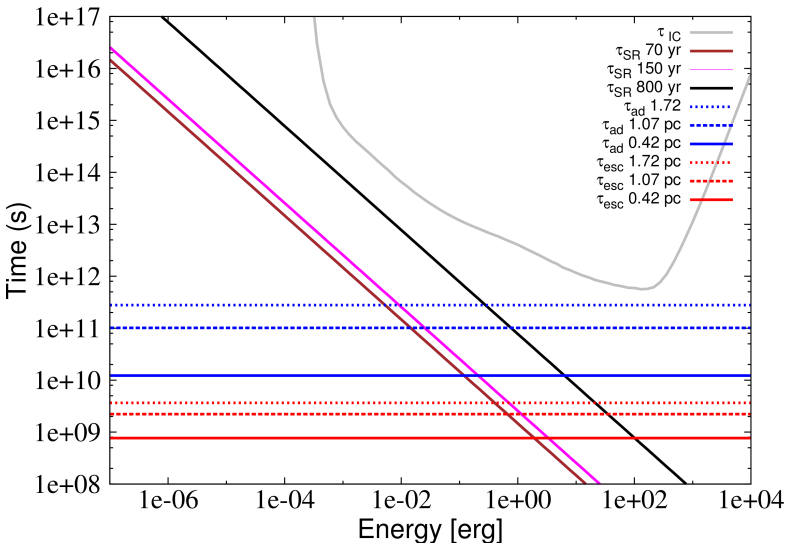

FIGURE 6.1: Timescales of the key processes in the model for PWN 3C 58 for different snapshots in time and at different radii. Here $\tau_{\rm IC}$ is the IC energy loss time, $\tau_{\rm SR}$ the SR loss time and is given for three different ages of the PWN, $\tau_{\rm ad}$ is the adiabatic loss time given for three different positions in the PWN and $\tau_{\rm esc}$ is the time for a particle to escape the current zone (spherical shell) in the PWN via bulk flow, also given for three different positions. Here $\tau_{\rm IC}$ is the IC energy loss time scale (independent of t and r).

From figures 6.2 to 6.4, we note that for 3C 58 we find reasonable fits to all three the data subsets simultaneously and that all three fitting methods give similar results. Our best-fit parameters are similar to those found by Torres et al. (2013). Table 6.1 shows that the different methods gave similar best-fit parameter values, with the SFN method giving a smaller present-day magnetic field value, thus requiring an older age for the system to still be able to fit the SED. The age range found by all fitting methods is much lower than the pulsar characteristic age of $\tau_{\rm c} = 5\,380$ yr, perhaps pointing to a braking index $n > 3$ and a birth period close to the current period ($P_0 \approx P$). Interestingly, these preferred ages are much closer to the one argued for by Kothes (2013) of 830 yr that is linked to the historical SN explosion in 1 181 A.D. The radial magnetic field profile parameter $\alpha_{\rm B}$ was initially chosen to be free, but all of the optimisation schemes yielded $\alpha_{\rm B} \sim 0$ and we therefore set $\alpha_{\rm B} = 0$. This implies a constant magnetic field vs. radius and a velocity profile that goes like $V(r) \sim 1/r$. This finding justifies the assumption made in 0D models that the magnetic field is constant throughout the PWN, and to some extent explains their success in modelling the SEDs of several sources (Gelfand et al., 2009). The fits indicate a large bulk flow of particles as well as a normalisation (κ_0) for the diffusion coefficient that exceeds the Bohm diffusion coefficient by two orders of magnitude. These values are, however, still viable except for a bulk velocity of 3.5×10^{10} cm s^{-1} found as the best fit by the χ^2 method, which exceeds the speed of light. The combined χ^2 values for all three methods are large, indicating a formally bad fit or an underestimation of errors (in the absence of published errors for the SB profile we

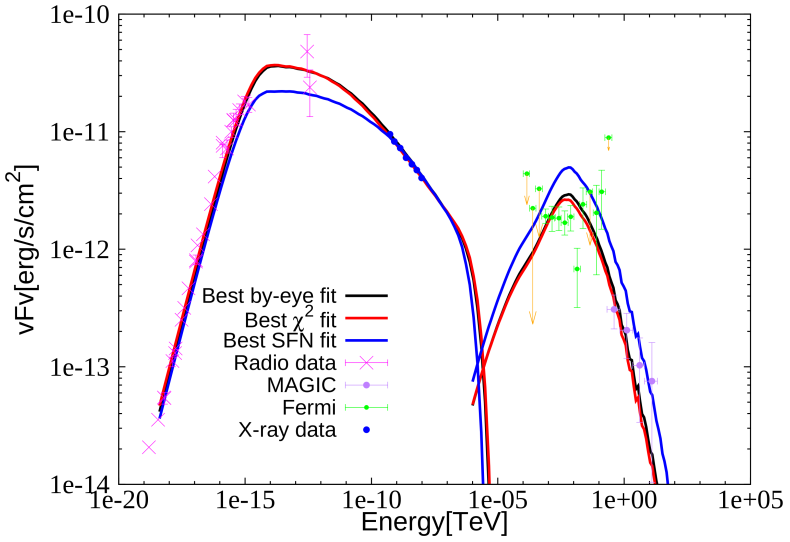

FIGURE 6.2: Broadband SED for PWN 3C 58, with radio data from *WMAP* (Weiland et al., 2011), infrared data from *IRAS* (Green, 1994, Slane et al., 2008), X-ray data from *ASCA* (Torii et al., 2000), GeV data from *Fermi*-LAT (Abdo et al., 2013) and TeV data from MAGIC (Aleksić et al., 2014).

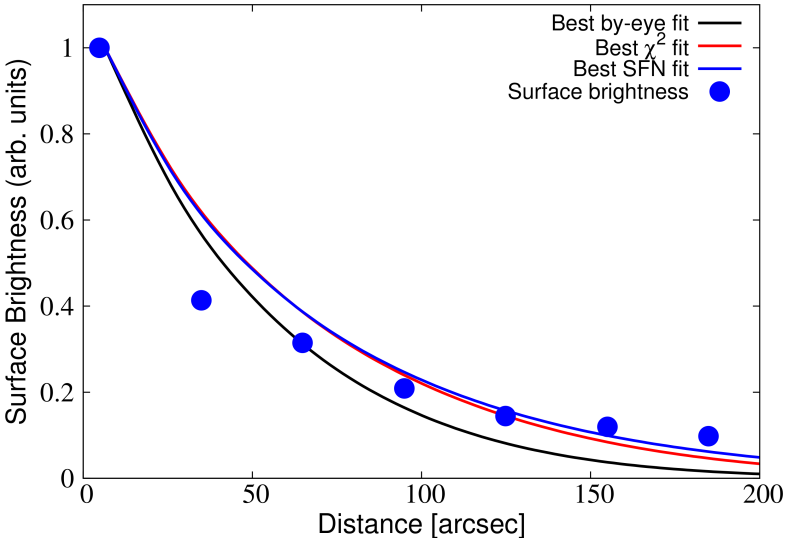

FIGURE 6.3: SB profile for PWN 3C 58. The data points are from Slane et al. (2004) for the energy range $0.5 - 4$ keV and the lines indicate our model best fits, with fitting methods indicated in the legend.

assume a 10% relative error). On the other hand, the χ^2_Φ values are close to 1.0 with the maximal value of 0.94 characterising the best fit. The χ^2_Φ values being so close to 1.0 reflects the fact that this method uses units of scaled flux rather than errors, and that it balances the contributions of the different subsets.

Generally, for this source and G21.5−0.9, Porth et al. (2016) find similar values for the magnetic field, but smaller values for the bulk flow and higher values for the spatial diffusion coefficient. Our inferred values also seem similar to those of Lu et al. (2017c). We attribute differences to the different model implementations.

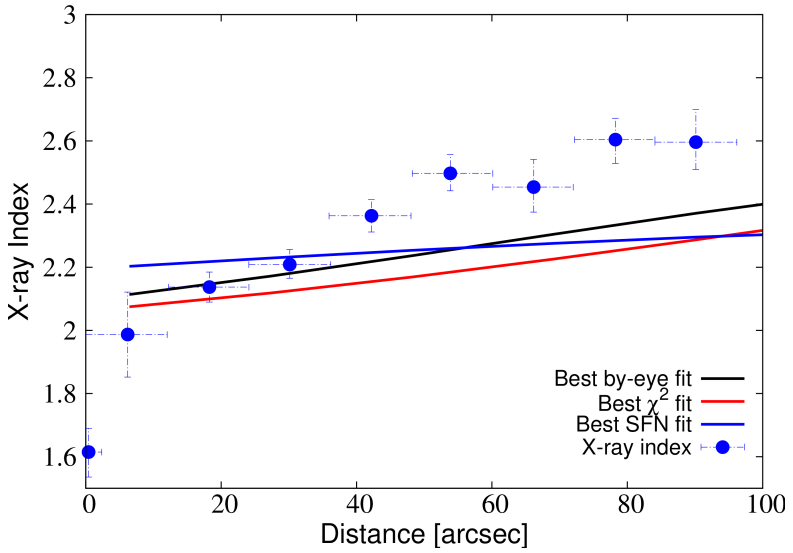

FIGURE 6.4: X-ray photon index for PWN 3C 58 vs. radius. The data points are from Slane et al. (2004) and the lines indicate our model best fits.

Fixed parameters			
Period (P) (s)			0.065
Time derivative of period ($\dot{P}$) (s s^{-1})			1.5×10^{-13}
Spin-down luminosity ($L_{\rm age}$) (erg/s)			2.7×10^{37}
Braking index (n)			3
Distance to the source (kpc)			3.2
Index of the injected spectrum (α_1)			1.31
Index of the injected spectrum (α_2)			2.92
Break energy ($\gamma_{\rm b}$)			9×10^4
Conversion efficiency (η)			0.2
Magnetic field time dependence ($\beta_{\rm B}$)			-1.0
Soft-photon components:		T (K)	u (eV/cm^3)
Cosmic microwave background (CMB)		2.76	0.23
Infrared		30.0	2.5
Optical		3000.0	25.0
Fitted parameters			
	By-eye	χ^2	χ^2_Φ
Radial parameter of the magnetic field ($\alpha_{\rm B}$)	0.0	0.0	0.0
Present-day magnetic field (μG)	65.7	70.7	39.1
Bulk flow normalisation (10^{10} cm s^{-1})	1.8	3.5	1.0
Age (kyr)	1.121	1.152	1.589
Diffusion coefficient normalisation (κ_0)	80.9	133.1	74.0
χ^2/ν	697/46	380/46	830/46
	(15.2)	(8.3)	(18.0)
χ^2_Φ	0.88	0.93	0.94

TABLE 6.1: Best-fit parameters for PWN 3C 58, with T the temperature and u the energy density assumed for each soft-photon blackbody component.

6.2.2 PWN G21.5−0.9

PSR J1833−1034 is one of the youngest pulsars in the Galaxy with an estimated age of 870 yr (Bietenholz and Bartel, 2008). This pulsar powers PWN G21.5−0.9 that has a nearly spherical shape in the radio and X-ray bands. Camilo et al. (2006) found the pulsar period of 61.8 ms with a period derivative of 2.02 $\times$ 10^{-13} s s^{-1}. The distance to PWN G21.5−0.9 is estimated as 4.7±0.4 kpc (Camilo et al., 2006, Tian and Leahy, 2008). VHE γ-rays in the 1−10 TeV energy range have been detected by the H.E.S.S. experiment during their Galactic Plane Survey and they found a flux of

$2.6 \times 10^{33}(d/4.9\text{kpc})^2\text{erg s}^{-1}$ and a power-law spectral index of $\Gamma = 2.42 \pm 0.19$ (Abdalla et al., 2018a).

In contrast to PWN 3C 58, PWN G21.5−0.9 did not give similar best fits for the three different fitting methods. In this source a form of degeneracy in the model becomes evident. From Figure 6.5 we see that all the methods give reasonable fits to the overall SED with the χ^2 and the SFN methods not being able to fit the infrared data as well as the by-eye method. This can be attributed to the large errors on the infrared data that cause the χ^2 and the SFN methods to assign a very small weight to these points. The by-eye method yielded a good fit to the SED as well as the X-ray spectral index profile, but was unable to find a simultaneous good fit to the SB profile. This resulted in the very large χ^2 value for the by-eye method, as well as the very small χ^2_Φ value in Table 6.2 ($\chi^2_\Phi \ll 1$ is equivalent to $\chi^2/\nu \gg 1$, indicating an extremely bad fit). This failure to find a good SB profile is due to the fact that the by-eye method favours a bulk speed normalisation that is a few orders of magnitude larger than that preferred by the other methods. This leads to the SB profile not decreasing as rapidly as the data indicate. The X-ray index profile, however, is particularly well fitted using this method. The degeneracy of the model becomes clear when one considers Figure 6.6 that shows that both the χ^2 and SFN methods give similar good results in fitting the SB profile, but both being unable to fit the X-ray steepening as seen in the data (Figure 6.7). This is, however, a better overall fit with the combined χ^2 value being much smaller than that of the by-eye method, as well as the χ^2_Φ value being closer to 1.0. The X-ray steepening has historically been attributed to a cooling effect[3]. The best fits for χ^2 and SFN, however, indicate the opposite trend, which might be interpreted as some sort of acceleration that is occurring in the system. This is, however, not the case here. We plot the SR spectrum for the first 11 radial bins and for two different parameter sets as found using the by-eye (Figure 6.8) and SFN (Figure 6.9) methods. The spectral index plotted in Figure 6.7 is derived from the slopes of the thicker lines in the $2 - 10$ keV energy range as shown in Figure 6.8 and Figure 6.9. The expected cooling effect can be clearly seen in Figure 6.8, but in Figure 6.9 the entire spectrum decreases rapidly as one moves away from the centre. This is due to the fact that in this case, the bulk flow of the particles is very slow and thus confines the particles to the inner parts of the PWN. The particles radiate most of their energy there before being able to move to the outer reaches of the PWN, leading to a rapid decrease in particle density with radius. This explains the hardening of the X-ray photon index with radius. In summary, we note that for this source we can either fit the SED and SB profile or the SED and X-ray spectral index profile, but not

[3]The SR energy loss rate is proportional to E_e^2. Thus, higher-energy particles lose energy more rapidly as they move farther away from the central part of the PWN. This results in spectral steepening with distance, causing the X-ray photon index to increase with radius. If SR losses dominate, this results in spectral steepening.

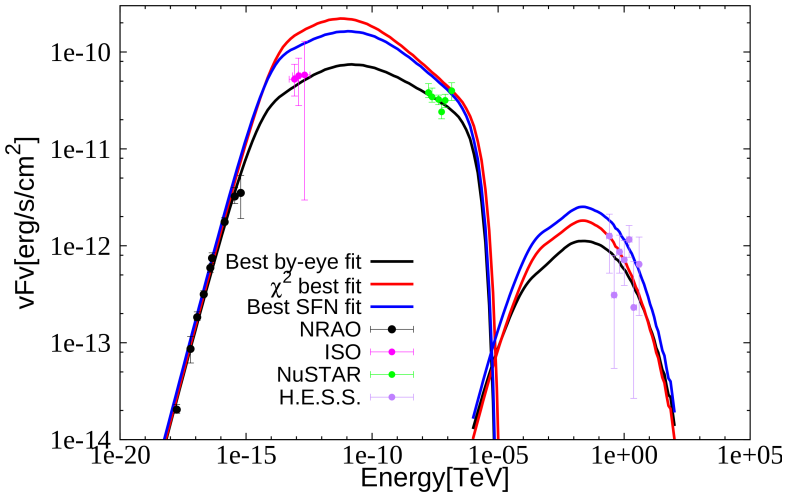

FIGURE 6.5: Broadband SED for PWN G21.5−0.9. The radio data are from NRAO observations (Salter et al., 1989), infrared data from the *Infrared Space Observatory* (Gallant and Tuffs, 1998), X-rays from *NuSTAR* observations by Nynka et al. (2014) and the TeV data from H.E.S.S. (Djannati-Ataï et al., 2008).

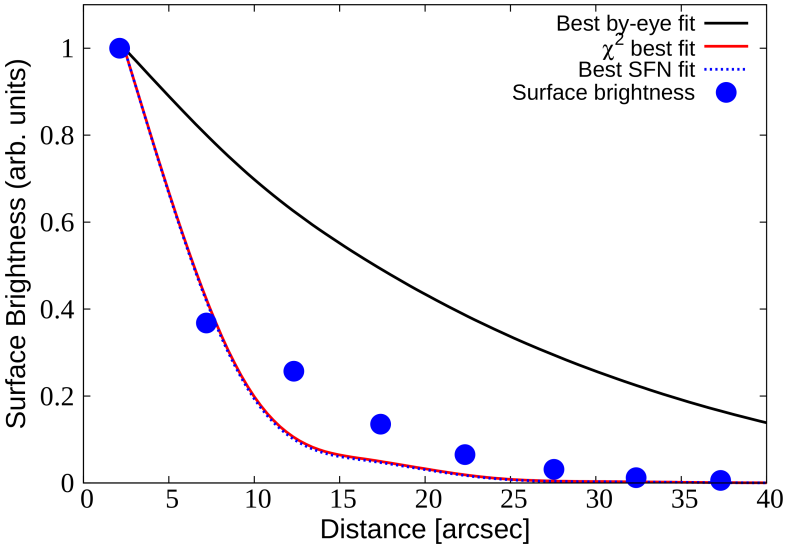

FIGURE 6.6: SB profile for PWN G21.5−0.9 with data points from Matheson and Safi-Harb (2005) and the lines indicating the model best fits.

all three observables concurrently. Our inferred parameters are not too different from those of Porth et al. (2016) and Lu et al. (2017c).

6.2.3 PWN G0.9+0.1

PWN G0.9+0.1 is a well-known composite SNR (Helfand and Becker, 1987), as indicated by its characteristic radio morphology: it exhibits a flat-spectrum radio core ($\sim 2'$ across) corresponding to the PWN, and also clear, steeper shell components ($\sim 8'$ diameter shell). This bright, extended source near the Galactic Centre has since become a well-known SNR, with an estimated age of a few thousand years (Aharonian et al., 2005)

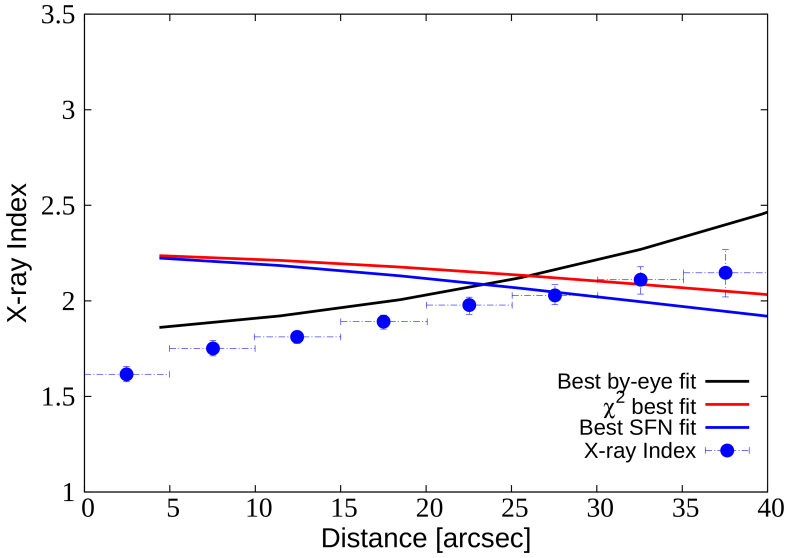

FIGURE 6.7: X-ray index profile for PWN G21.5−0.9 with data points from Matheson and Safi-Harb (2005) and the lines indicating the model best fits.

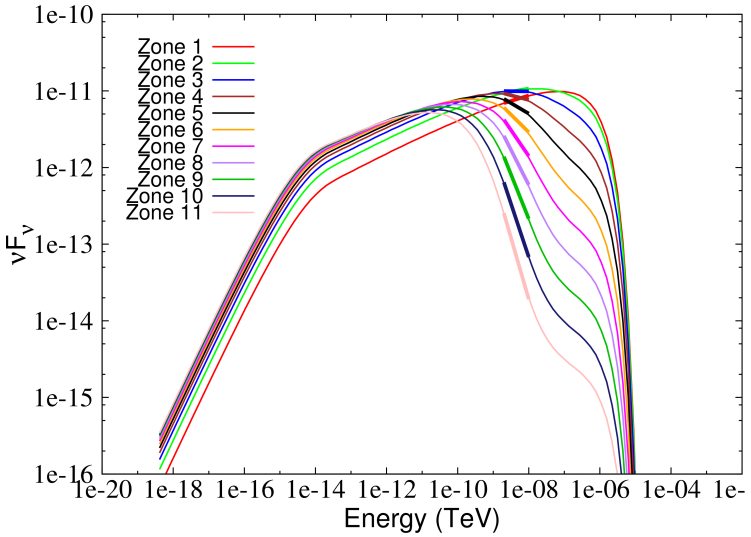

FIGURE 6.8: SR spectrum for PWN G21.5−0.9 for the first 11 LOS integration zones, with the spectral index in the X-ray energy band (2 − 10 keV) indicated by the thick lines for the by-eye best fit.

with a lower bound of 1100 yr (Dubner et al., 2008) and a typical distance of 8.5 kpc. During X-ray observations of the Galactic Centre, Sidoli et al. (2004) serendipitously observed SNR G0.9+0.1 using the *XMM*-Newton telescope. Sidoli et al. (2004) fit an absorbed power-law spectrum that yielded a photon index of $\Gamma_X \sim 1.9$ and an energy flux of $F = 4.8 \times 10^{-12}$ erg cm^{-2} s^{-1} in the 2−10 keV energy band. This translates to a luminosity of $L_X \sim 5 \times 10^{34}$ erg s^{-1} for a distance of 10 kpc. Aharonian et al. (2005) obtained a power-law fit to the observed γ-ray spectrum with a photon index of $2.29 \pm 0.14_{stat}$ and an integral photon flux of $(5.5 \pm 0.8_{stat}) \times 10^{-12}$ cm^{-2} s^{-1} above 200 GeV. Subsequently, the radio pulsar PSR J1747−2809 was discovered in

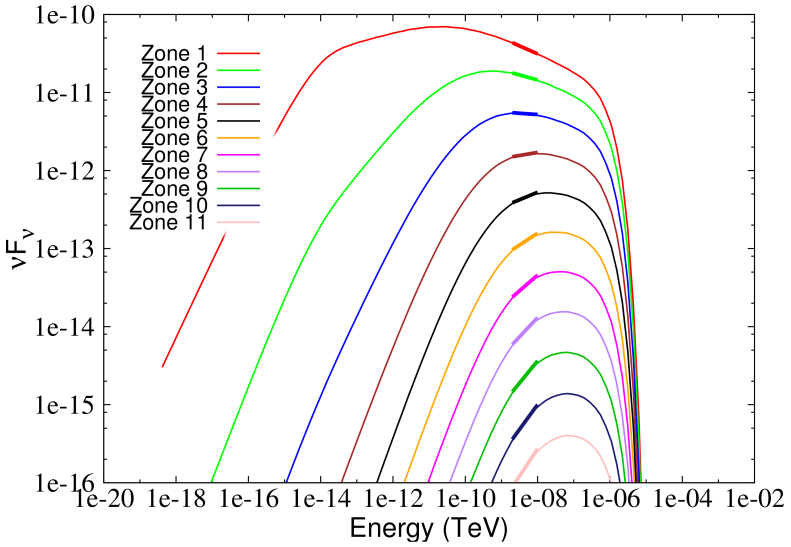

FIGURE 6.9: SR spectrum for PWN G21.5−0.9 for the first 11 LOS integration zones with the spectral index in the X-ray energy band (2 − 10 keV) indicated by the thick lines for the SFN best fit.

Fixed parameters			
Period (P) (s)			0.06186
Time derivative of period ($\dot{P}$) (s s^{-1})			2.0×10^{-13}
Spin-down luminosity ($L_{\rm age}$) (erg/s)			3.4×10^{37}
Braking index (n)			3
Distance to the source (kpc)			4.7
Index of the injected spectrum (α_1)			1.0
Index of the injected spectrum (α_2)			2.5
Break energy ($\gamma_{\rm b}$)			1.1×10^{5}
Conversion efficiency (η)			0.01
Magnetic field time dependence ($\beta_{\rm B}$)			−1.0
Soft-photon components:		T (K)	u (eV/cm^3)
CMB		2.76	0.23
Infrared		35.0	3.4
Optical		3500.0	5.0
	By-eye	χ^2	χ^2_Φ
Fitted parameters			
Radial parameter of the magnetic field	0.0	0.0	0.0
Present-day magnetic field (μG)	72.7	104	74.4
Bulk flow normalisation (10^{10} cm s^{-1})	0.81	7.0×10^{-6}	1.3×10^{-5}
Age (kyr)	1.121	0.980	1.589
Diffusion coefficient normalisation (κ_0)	4.3	14.0	74.0
χ^2/ν	117212/38 (3085)	1265/38 (33.2)	1306/38 (34.4)
χ^2_Φ	−64.2	0.59	0.60

TABLE 6.2: Best-fit parameters for PWN G21.5−0.9.

PWN G0.9+0.1 with a period $P = 52.2$ ms and $\dot{P} = 1.56 \times 10^{-13}$s s^{-1} (Camilo et al., 2009).

Figures 6.10 to 6.12 show the results for PWN G0.9+0.1. The by-eye method was able to find a good fit to the SED and a reasonable fit to the X-ray index profile, but was unable to reproduce the SB profile, since (as in the previous case) the preferred bulk flow of the particles is large (driven by the X-ray photon index profile), resulting in a larger source. This led to rather poor goodness-of-fit values according to the χ^2 and χ^2_Φ test statistics. The χ^2 and SFN methods were able to find reasonable fits to the SED and a comparatively better fit to the SB profile. Their goodness-of-fit values are relatively

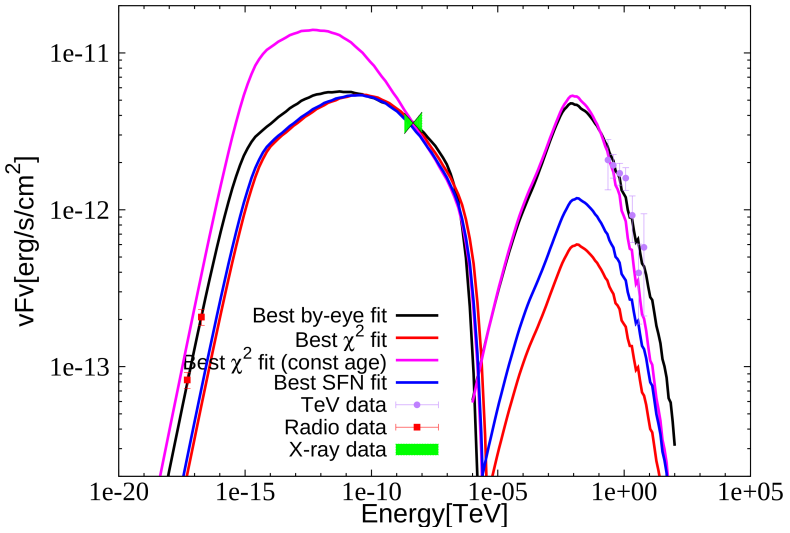

FIGURE 6.10: Broadband SED for PWN G0.9+0.1, with radio data from Dubner et al. (2008), X-ray data from Porquet et al. (2003) and the TeV data from H.E.S.S. (Aharonian et al., 2005).

close, with each method preferring slightly different parameters. However, these fits preferred a younger age for the PWN, resulting in fewer particles in the system and thus a worse fit to the high-energy tail of the IC component of the SED. From the model of Torres et al. (2014), the preferred age of the system is a couple of thousand years. We thus decided to fix the age to 3 078 yr, which is the age preferred by the by-eye method. This also agrees better with the pulsar age of 5 600 yr. We then redid the χ^2 test, leaving the present-day magnetic field, the bulk flow of particles and the diffusion normalisation as free parameters. The result is indicated by the magenta line in figures 6.10 to 6.12 and the best-fit values are shown in brackets in Table 6.3. In this case, we found a good fit to the SED as well as to the SB profile, and the trend in the X-ray index was more accurately represented, characterised by a reduced χ^2 value of 19.6 and a χ^2_Φ value of 0.73. In summary, the code was not able to find a simultaneous good fit to all three data subsets. PWN G0.9+0.1 has been modelled by Venter and de Jager (2007) and Torres et al. (2014). Venter and de Jager (2007) found similar spectral results with the exception that their modelled age was 6.5 kyr, which is twice the age predicted by Torres et al. (2014) and by our by-eye method. The predicted present-day magnetic field varies slightly between the three modelling attempts with our predictions being the largest and Venter and de Jager (2007) being the smallest, but all the predictions are in the order of tens of μG.

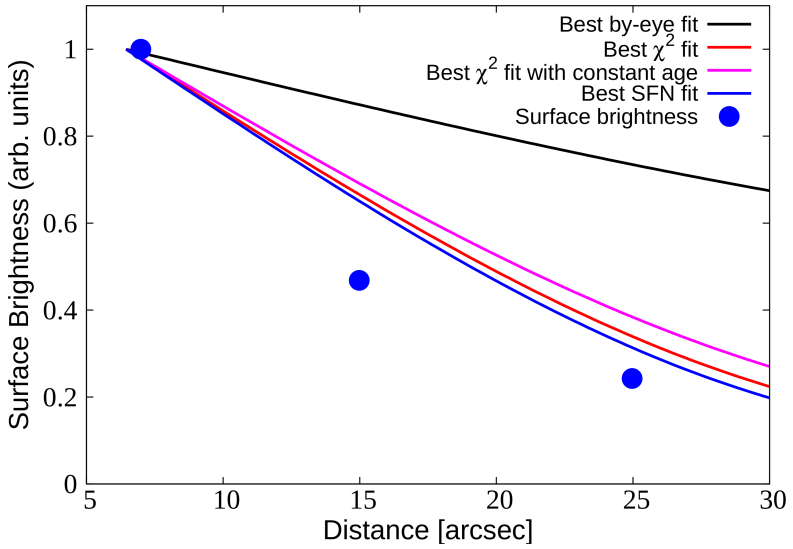

FIGURE 6.11: SB profile for PWN G0.9+0.1 with data points from Holler et al. (2012a) and the lines indicating the model best fits.

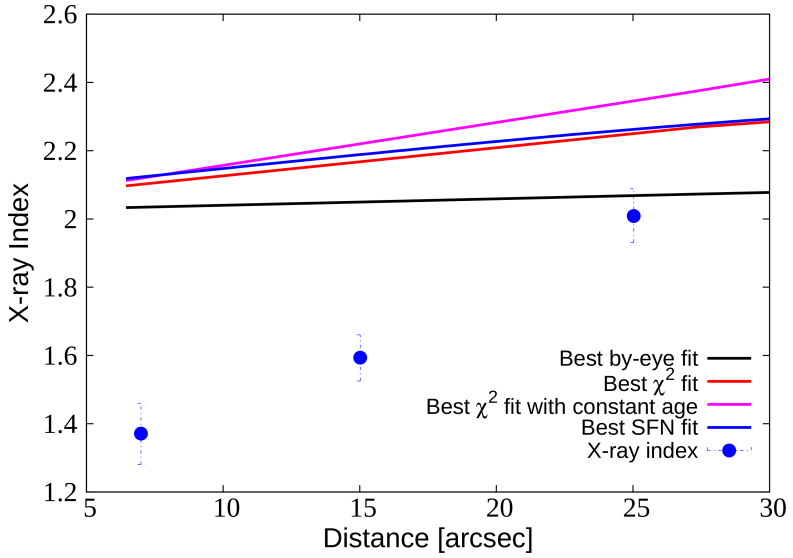

FIGURE 6.12: X-ray photon index profile for PWN G0.9+0.1 with data points from Holler et al. (2012a) and the lines indicating the model best fits.

6.3 Characterising the Non-colocation of the Various Best-fit Solutions

We find that our different search methods yield different, i.e., non-unique best-fit parameters. This is because: (1) the statistical metric (or by-eye intuition) used to assess the goodness of fit in each case, differs; (2) the methods use different ways to combine the different data sets in order to find a compromise solution that concurrently fit all data.

Fixed parameters			
Period (P) (s)			0.0522
Time derivative of period ($\dot{P}$) (s s^{-1})			1.56×10^{-13}
Spin-down luminosity ($L_{\rm age}$) (erg/s)			4.3×10^{37}
Braking index (n)			3
Distance to the source (kpc)			8.5
Index of the injected spectrum (α_1)			1.4
Index of the injected spectrum (α_2)			2.7
Break energy ($\gamma_{\rm b}$)			1.0×10^{5}
Conversion efficiency (η)			0.01
Magnetic field time dependence ($\beta_{\rm B}$)			-1.0
Soft-photon components:		T (K)	u (eV/cm^3)
CMB		2.76	0.23
Infrared		30.0	2.5
Optical		3000.0	25.0
	By-eye	χ^2	χ^2_Φ
Fitted parameters			
Radial parameter of the magnetic field	0.0	0.0	0.0
Present-day magnetic field (μG)	15.0	37.7 (25.1)	26.8
Bulk flow normalisation (10^{10} cm s^{-1})	0.27	9.5×10^{-2} (5.2×10^{-2})	4.5×10^{-2}
Age (kyr)	3.078	0.611 (3.078)	1.085
Diffusion coefficient normalisation (κ_0)	2.2	0.92 (0.11)	0.35
χ^2/ν	900/32	570/32	762/32
	(28.1)	(17.8)	(23.8)
χ^2_Φ	0.24	0.75	0.76

TABLE 6.3: Best-fit parameters for PWN G0.9+0.1.

Ideally, all methods would find the same answer, and no compromise would have been needed when fitting multiple data sets. Also, the value of χ^2_Φ would have been unity for both the single sets and the average value. However, since the optimal solutions differ between methods, it would be good to quantify this discrepancy. Using parameter errors may indicate whether the contours found by different methods overlap; however, these primarily reflect observational errors and may not be the best characterisation of this kind of model degeneracy.

A more relevant proxy of "non-colocation" of the respective best-fit parameters chosen by each method may be to quantify the amount of compromise in goodness of fit that occurs when fitting a single data set vs. concurrently fitting all three sets.

	$B_{\rm age}$ (μG)	Age (yr)	V_0 (10^{10} cm s^{-1})	κ_0	χ^2_Φ (SED)	χ^2_Φ ($\Gamma_{\rm X}$)	χ^2_Φ (SB)	χ^2_Φ (Avg.)
PWN 3C 58								
Global	39.1	1588.9	1.02	74.0	0.99	0.92	0.92	0.94
SED	50.4	743.0	1.58	4.2	**0.99**	0.91	0.61	0.84
$\Gamma_{\rm X}$	81.9	2134.0	0.71	13.9	0.53	**0.94**	0.45	0.64
SB	43.6	2114.0	0.22	104.7	0.1	0.88	**0.93**	0.64
By-eye	65.7	1121.0	1.8	81	0.99	0.94	0.72	0.88

TABLE 6.4: Best-fit parameters found when fitting all data sets concurrently (first row for each source) vs. only fitting one data set at a time (subsequent rows) for PWN 3C 58, with the relevant χ^2_Φ values indicated in boldface and the implied values for the other sets also shown. The average χ^2_Φ value is given in the final column.

Table 6.4 indicates the χ^2_Φ values for four different scenarios, for each modelled source. The first scenario (labelled "Global") is for fitting all three data sets concurrently, and is shown in the first row. The next three scenarios are when a single data set is fit without regarding any other set; the relevant χ^2_Φ value is shown in boldface for the individual data sets and is labelled "χ^2_Φ (SED)", "χ^2_Φ ($\Gamma_{\rm X}$)" and "χ^2_Φ (SB)", respectively. Also indicated are the implied values of χ^2_Φ for the other data sets, since we do have a model

prediction for these data even if they were not explicitly fitted. Lastly, the average value for χ^2_Φ is shown in the final column.

From the table, one can see that the global fit yields the best average χ^2_Φ value, and all other fits involving only a single data set have lower average values, indicating an optimal compromise in the first case. Second, when only a single data set is used for a particular fit, the single-set value of χ^2_Φ may be high, but the corresponding fits for the other sets are not good. So, in the first source for example, the non-colocation of the respective single-set best fit parameters leads to a compromise concurrent fit, with $\chi^2_\Phi = 0.94$ for this global fit. We thus move away from the optimal single-set fits with values of 0.99, 0.94 and 0.93 and obtain a global compromise solution with values of 0.99, 0.92 and 0.92. This represents a slight loss in goodness of fit of $\Delta\chi^2_\Phi = 0.01$ with respect to the ideal single-set fits, for the last two data sets. In the ideal case, the global fit would thus have had an average value of $\chi^2_\Phi = 0.95$ (average of bold table entries) instead of the 0.94 we now obtain, indicating only a slight compromise for the global fit, but still obtaining the highest average value of χ^2_Φ compared to the other rows in the table.

The χ^2_Φ values for the by-eye fit are usually not good, and underscores that a by-eye method uses a different intuitive metric that may not be regarded as statistically optimal; instead, it may yield model solutions that can be used as a basis for comparison with the fits yielded by the statistical methods. In addition, we found that when we perform the exercise described above for the other two sources, the single-set fits have problems converging, and the values for χ^2_Φ are quite bad for the other bands. This indicates that we need the compromise fit to have any hope of a reasonable fit to all data sets. Future model refinement should help to minimise the effect of non-colocation of single-band best-fit parameters.

6.4 Summary

In this Chapter I have introduced the methods used to find best fits of the model outputs to the available data. A new scaled-flux-normalised test statistic was introduced to improve the possibility of finding concurrent best fits to the heterogeneous data sets that are available for the three sources. We found reasonable model fits. These fits are, however, degenerate in nature and we discussed this in the last part of the Chapter by including a section about the non-colocation of our model best-fit parameters. A more detailed discussion of these best fits can be found in Chapter 7.

Chapter 7

Conclusion

The next couple of decades are going to be some of the most exiting years in modern astrophysics. This is due to the development of a new generation of telescopes that are bigger and more sensitive than all current ones. This makes "now" the best time to develop new and improve current, modelling strategies for several different astrophysical phenomena. With this idea in mind we envisioned the improvement of a previous emission code that modelled PWNe. This vision has become a reality and is encapsulated in this thesis. In this concluding Chapter I will reiterate the problems and void in the current modelling landscape and then summarise the advances that this study has made to try and answer some of the still unknown questions by starting to fill the void left behind by other studies.

As mentioned above, new telescopes, e.g., CTA, AMEGO, IXPE and SKA will be facilities that will produce a large increase in the quality of data from PWNe by having the ability to observe these objects at an enhanced angular resolution, as well as greater flux sensitivity. Current PWN modelling attempts can be summed up in three main categories ranging from MHD, emission and hybrid models. MHD and hybrid models have the ability to model the morphology of PWNe in great detail and will benefit greatly from the new generation of telescopes. Most emission codes, on the other hand, are 0D codes that only yield information regarding the spatially-averaged radiation spectra of PWNe. These types of models will not benefit from the newly developed telescopes and this is where we identified the void in the modelling landscape.

7.1 Contributions of this Study

The main contribution of this study is the successful development and implementation of a spatio-temporal leptonic emission code for PWNe. A brief summary of the main

points of development and implementation will be discussed next with more detailed conclusions in Section 7.2.

The code was developed in the following manner:

- The code of Venter and de Jager (2007) that modelled the transport of particles by assuming a parametric form of the B-field and that did not take into account the effects of adiabatic energy losses, was used as a basis. The particle transport was also improved on by using a Fokker-Planck type transport equation to model the motion of the particles in the PWN. This allowed us to not only model the radiation spectra from PWNe but also presented the opportunity for this model to yield information regarding morphological aspects of PWNe.
- Our new code was calibrated with previous results found by Venter and de Jager (2007) as well as Torres et al. (2014) to test the validity of the results produced. This was executed by comparing predicted SEDs for specific sources modelled by the other authors, and we found that our model reproduced their results well. A detailed parameter study was also done to investigate the model's behaviour across parameter space.
- Three young PWNe, PWN 3C 58, PWN G21.5−0.9 and PWN G0.9+0.1 were chosen to be modelled due to the availability of spectral and spatial data from these sources. The SED, SB profile and X-ray photon index for these sources were modelled and we found reasonable concurrent fits to these data. This was made possible by implementing a scaled-flux normalised χ^2 test statistic to find the best possible fits to these sources.

7.2 Detailed Conclusion

7.2.1 The Model

To model a PWN we needed to know how particles act when they are in an environment consisting of electromagnetic and soft-photon fields. To this end, we implemented a simplified form of the well-known Fokker-Planck transport equation and assumed boundary conditions for the system. The following is a list of the assumptions made in our code:

- The source is spherically symmetric with several spatial bins. Some inner radius was assumed to be the inner boundary where particles are injected with a spectrum in the form of a broken power law.

- The injected particles are then allowed to traverse the PWN by implementing convection and diffusion.
- The particles are allowed to escape the system at the outer boundary.
- The particles lose energy though radiative losses as well as adiabatic losses due to the expansion of the PWN.
- These particles radiate their energy through two main processes: SR and IC scattering are the two main radiation mechanisms incorporated in the model with SSC and bremsstrahlung assumed to have a negligible effect (as shown by others).

These assumptions allowed us to model not only the observed radiation spectra, but also spatial observables for PWNe. The particle spectrum is known at different radii from the centre and this allowed us to calculate the radiation spectra for different radii by incorporating a line-of-sight calculation. This enabled us to predict the SB profile and spectral index as a function of distance from the centre for any energy range. In this study we used the 2.0−10.0 keV X-ray energy band due to the availability of data.

7.2.2 Discussion of Source Fits

PWN 3C 58, PWN G21.5−0.9 and PWN G0.9+0.1 were chosen as case studies due to the availability of spectral and spatial data, as well as the fact that they are young PWNe. Our model found reasonable concurrent fits to the spectral and spatial observables, but each source posed its own challenges. We found that a spatially constant magnetic field was preferred, leading to a velocity profile that scales as $V(r) \sim 1/r$. This explains the overall success of the 0D models that assume a spatially constant magnetic field; e.g., Gelfand et al. (2009). Our code was also able to predict spectral steepening with increasing radius due to cooling via SR losses.

We followed various approaches to obtain best fits to the available data, finding that not all methods gave similar best fits. They did, however, shed light on the problems that arise when fitting heterogeneous data, indicating that the constraining power of the data on the models under scrutiny is also subject to the fitting methods one chooses to use. A by-eye fitting method proved useful, but is limited by the size of the parameter space one needs to explore. The χ^2 test statistic yielded reasonable results, but in this framework data with small relative errors dominate other data sets, practically eliminating the effect of the latter when minimising the χ^2 value. The SFN test statistic proved advantageous when dealing with heterogeneous data sets. However, we could not clearly prefer one of these methods over the others. In particular, non-location of best-fit

parameters preferred by each separate data set laid bare some model degeneracies, since in the ideal case parameter fits on the various individual data sets should yield consistent results when performing concurrent fitting of all sets involved. This may point not only to the power of each search method, but perhaps to a revision that is needed in the model, since any fitting method would "fail" to find adequate solutions if such solutions do not exist in the model's solution space in the first place. Since the parameter space for these types of models are complicated and large, it would be worthwhile to explore it in more detail as this would help gauge the uniqueness of best-fit solutions as well as degeneracies that exist between some parameters.

Our initial hope was that inclusion of spatial data would reduce the errors on the fitting parameters within a framework of concurrent fitting of spatial and spectral data. However, given the issues mentioned above, as well as the fact that all fits are formally not acceptable according to the χ^2 method, we envision that by using, e.g., an MCMC ensemble sampler for a fine spatial and energy resolution, one may obtain a better understanding of the parameter space properties and improved estimates of errors on best-fit parameters. This should also help address the question of whether spatial data may actually help to reduce uncertainties in these parameters.

Our best-fit parameters (notably magnetic fields, bulk flow normalisations, and diffusion coefficients) resemble those found by Porth et al. (2016) and Lu et al. (2017c), although relatively wide ranges are allowed for several of these. On the one hand, this indicates some consistency in the independent approaches but on the other hand also some degeneracy in the sense that the currently available data do not yet have the discriminatory power to distinguish between models that make quite different assumptions about the PWN environment. We developed our code to have as few free parameters as possible, thus assuming very basic profiles for, e.g., the magnetic field and the bulk particle motion. Model degeneracy will have to be broken by future observations, including polarisation properties that may better constrain the magnetic field topology.

As alluded to above, a second type of degeneracy was uncovered while fitting the spectral and spatial data of G21.5−0.9 and G0.9+0.1. We could fit two out of three data subsets, but not all three subsets in two of the three PWNe we considered. This probably points to some physics that we are missing in the current model. One avenue would be to refine the parametrisation of our model magnetic field and bulk flows, or to connect them in a different way to enable us to allow more freedom in the model to fit both the SB and the X-ray index profiles, in addition to the SED. We could also reassess our choice of free parameters and attempt to more closely incorporate MHD results in our model calculations.

7.3 Future Recommendations

The model developed shows the validity and possibilities of this type code. It is, as mentioned, not perfect and there is room for improvement. The following is a list of recommendations for future studies:

- The code currently models the PWN as a spherically symmetric system (1D). PWNe are, however, not spherically symmetric systems as can be clearly seen from X-ray observations. There are examples that point to the fact that PWNe typically exhibit torus-and-jet-like structures. The first recommendation therefore is to model the PWNe in more spatial dimensions (2D or 3D) to incorporate these spatial features into the model. On the other hand, incorporating more dimensions imply more free parameters in the model that need to be constrained by data.
- This model is only able to fit young sources that are still in the free-expansion phase. This significantly reduces the number of possible sources that can be modelled. A big improvement to this model would be to add the ability to model the reverberation phase of the PWN's evolution. This has been done for 0D models, see e.g., Martín et al. (2016), Torres and Lin (2018), Torres et al. (2019), where they consider the pressure produced by the particles and magnetic field inside the PWN. This could be implemented in this 1D model and allows us to model more sources.
- Some older PWNe are offset from the pulsar, revealing a bullet shape (bow-shock nebulae, see e.g., Bucciantini 2014). This is either due to an inhomogeneity in the interstellar medium (ISM) in which the PWN expands causing an asymmetric reverse shock and thus an offset PWN, or to the pulsar receiving some kick velocity at birth, thus moving away from the PWN centre. The radiation peaks at the pulsar position where energetic particles are freshly injected, thus emphasising the bullet shape. These effects could be added to model this subclass of PWNe.
- A population study can also be conducted to investigate the currently known trends, e.g., the X-ray luminosity that correlates with the pulsar spin-down luminosity and its anti-correlation with the characteristic age of the pulsar. Other unknown trends can also be probed, e.g., an investigation could be done into whether there is a correlation between the TeV surface brightness of the PWN and the spin-down luminosity of the pulsar (Abdalla et al., 2018b), as well as the surface brightness versus age.

Continued improvement both in the PWN model and in fitting methods will help us make the best use of forthcoming morphological data, especially in the VHE waveband.

Adding different types of data using one consistent modelling framework as well as rigorous statistical methods would also increase the constraining power thereof.

Appendix A

Mathematical Details

In this Appendix, I collect the mathematical results that were not included in the main part of the thesis to improve the readability of the main text. They are, however, added here to clarify some of the less obvious steps.

A.1 The Fokker-Planck type Transport Equation

A.1.1 General Transport Equation

The general transport equation in terms of momentum is given by (Moraal, 2013)

$$\frac{\partial f}{\partial t} = -\nabla \cdot \mathbf{S} + \frac{1}{p^2}\frac{\partial}{\partial p}\left(p^2 \langle \dot{p} \rangle_{\mathrm{tot}} f\right) + Q(\mathbf{r}, p, t) \tag{A.1}$$

with

$$\begin{aligned} \nabla \cdot \mathbf{S} &= \nabla \cdot (\mathbf{V} f - \underline{\mathbf{K}} \nabla f) \\ &= \nabla \cdot (\mathbf{V} f) - \nabla \cdot (\underline{\mathbf{K}} \nabla f) \\ &= \mathbf{V} \cdot (\nabla f) + f(\nabla \cdot \mathbf{V}) - \nabla \cdot (\underline{\mathbf{K}} \nabla f) \end{aligned} \tag{A.2}$$

where the symbols have been defined in Chapter 3. By substituting Eq. (A.2) into Eq. (A.1), and using the total energy loss rate as

$$\langle \dot{p} \rangle_{\mathrm{tot}} = \dot{p}_{\mathrm{rad}} + \dot{p}_{\mathrm{ad}}, \tag{A.3}$$

where $\dot{p}_{\rm rad}$ is the energy loss rate due to radiation, and $\dot{p}_{\rm ad} = \frac{1}{3}(\nabla \cdot \mathbf{V})p$ the adiabatic energy rate of change (usually a loss rate during the expansion phase), we find

$$\begin{aligned}
\frac{\partial f}{\partial t} &= -\left[\mathbf{V}\cdot(\nabla f) + f(\nabla\cdot\mathbf{V}) - \nabla\cdot(\underline{\mathbf{K}}\nabla f)\right] + \frac{1}{p^2}\frac{\partial}{\partial p}\left(p^3\frac{1}{3}(\nabla\cdot\mathbf{V})f\right) + \frac{1}{p^2}\frac{\partial}{\partial p}\left(p^2\left\langle\dot{p}\right\rangle_{\rm rad} f\right) + Q(\mathbf{r},p,t)\\
&= -\mathbf{V}\cdot(\nabla f) - f(\nabla\cdot\mathbf{V}) + \nabla\cdot(\underline{\mathbf{K}}\nabla f) + \frac{1}{p^2}\left(\frac{1}{3}(\nabla\cdot\mathbf{V})\left[3p^2 f + p^3\frac{\partial f}{\partial p}\right]\right) + \frac{1}{p^2}\frac{\partial}{\partial p}\left(p^2\left\langle\dot{p}\right\rangle_{\rm rad} f\right) + Q(\mathbf{r},p,t)\\
&= -\mathbf{V}\cdot(\nabla f) - f(\nabla\cdot\mathbf{V}) + \nabla\cdot(\underline{\mathbf{K}}\nabla f) + f(\nabla\cdot\mathbf{V}) + \left(p\frac{\partial f}{\partial p}\right)\left(\frac{1}{3}(\nabla\cdot\mathbf{V})\right) + \frac{1}{p^2}\frac{\partial}{\partial p}\left(p^2\left\langle\dot{p}\right\rangle_{\rm rad} f\right) + Q(\mathbf{r},p,t)\\
&= -\mathbf{V}\cdot(\nabla f) + \nabla\cdot(\underline{\mathbf{K}}\nabla f) + \frac{1}{3}(\nabla\cdot\mathbf{V})\frac{\partial f}{\partial \ln p} + \frac{1}{p^2}\frac{\partial}{\partial p}\left(p^2\left\langle\dot{p}\right\rangle_{\rm rad} f\right) + Q(\mathbf{r},p,t).
\end{aligned} \tag{A.4}$$

Note the cancellation of the $f(\nabla\cdot\mathbf{V})$ terms. Eq. (A.4) corresponds to Eq. (18) of Moraal (2013). Furthermore, by using $U_p(\mathbf{r},p,t) = 4\pi p^2 f(\mathbf{r},p,t)$ also given in Moraal (2013), and $\underline{\mathbf{K}} = \kappa(p)$, we can rewrite Eq. (A.4) as follows:

$$\begin{aligned}
\frac{\partial f}{\partial t} &= -\mathbf{V}\cdot(\nabla f) + \nabla\cdot(\underline{\mathbf{K}}\nabla f) + \frac{1}{3}(\nabla\cdot\mathbf{V})\frac{\partial f}{\partial \ln p} + \frac{1}{p^2}\frac{\partial}{\partial p}\left(p^2\left\langle\dot{p}\right\rangle_{\rm rad} f\right) + Q(\mathbf{r},p,t)\\
\frac{1}{4\pi p^2}\frac{\partial U_p}{\partial t} &= -\frac{1}{4\pi p^2}\mathbf{V}\cdot(\nabla U_p) + \frac{1}{4\pi p^2}(\kappa\nabla^2 U_p) + \frac{1}{3}(\nabla\cdot\mathbf{V})\frac{1}{4\pi p^2}\left(\frac{\partial U_p}{\partial \ln p} - 2U_p\right) +\\
&\qquad \frac{1}{p^2}\frac{\partial}{\partial p}\left(\left\langle\dot{p}\right\rangle_{\rm rad}\left[\frac{U_p}{4\pi}\right]\right) + Q(\mathbf{r},p,t)\\
\frac{\partial U_p}{\partial t} &= -\mathbf{V}\cdot(\nabla U_p) + (\kappa\nabla^2 U_p) + \frac{1}{3}(\nabla\cdot\mathbf{V})\left(\frac{\partial U_p}{\partial \ln p} - 2U_p\right) + \frac{\partial}{\partial p}\left(\left\langle\dot{p}\right\rangle_{\rm rad} U_p\right) + Q'(\mathbf{r},p,t)
\end{aligned} \tag{A.5}$$

by using $\partial f/\partial \ln p = p\left(1/(4\pi p^2)\partial U_p/\partial p - 2/(4\pi p^3)U_p\right)$, and setting $Q'(\mathbf{r},p,t) = 4\pi p^2 Q(\mathbf{r},p,t)$.

A.1.2 Writing the Transport Equation in terms of Energy

In this section I will rewrite the transport equation in terms of energy by using the relation $E^2 = p^2c^2 + E_0^2$ (I will use the symbol E instead of $E_{\rm e}$ for the particle energy). In this part the source term $Q'(\mathbf{r},p,t)$ will be neglected and added later. Thus we start with Eq. (A.5)

$$\frac{\partial U_p}{\partial t} = -\mathbf{V}\cdot(\nabla U_p) + (\kappa\nabla^2 U_p) + \frac{1}{3}(\nabla\cdot\mathbf{V})\left(\frac{\partial U_p}{\partial \ln p} - 2U_p\right) + \frac{\partial}{\partial p}\left(\left\langle\dot{p}\right\rangle_{\rm rad} U_p\right) \tag{A.6}$$

and use the following:

$$\begin{aligned}
p &= \sqrt{\frac{(E^2 - E_0^2)}{c^2}}\\
\therefore \frac{dp}{dE} &= \frac{1}{2}\left(\frac{(E^2 - E_0^2)}{c^2}\right)^{-\frac{1}{2}}\frac{2E}{c^2}\\
&= \frac{E}{pc^2}.
\end{aligned} \tag{A.7}$$

But

$$U_p dp = U_E dE, \tag{A.8}$$

with U_E the number of particles per unit volume and energy. Therefore:

$$\begin{aligned} U_p &= U_E \frac{\sqrt{(E^2 - E_0^2)/c^2}}{E} c^2 \\ &= c U_E \frac{\sqrt{(E^2 - E_0^2)}}{E}. \end{aligned} \tag{A.9}$$

In Eq. (A.6) we have to calculate $\partial U_p / \partial \ln p$ and I will first show how this is done.

$$\begin{aligned} \frac{\partial U_p}{\partial \ln p} &= \frac{\partial U_p}{\partial \ln E} \frac{\partial \ln E}{\partial \ln p} \\ &= \frac{\partial U_p}{\partial \ln E} \frac{p}{E} \frac{dE}{dp} \\ &= \frac{\partial U_p}{\partial \ln E} \left(\frac{pc}{E} \right)^2 \\ &= \frac{\partial}{\partial \ln E} \left(c U_E \frac{\sqrt{(E^2 - E_0^2)}}{E} \right) \left(\frac{pc}{E} \right)^2 \\ &= \left(\frac{p^2 c^3}{E} \right) \frac{\partial}{\partial E} \left(U_E \frac{\sqrt{(E^2 - E_0^2)}}{E} \right) \\ &= \left(\frac{p^2 c^3}{E} \right) \left[\frac{\partial U_E}{\partial E} \frac{\sqrt{(E^2 - E_0^2)}}{E} + U_E \left(\frac{1}{\sqrt{(E^2 - E_0^2)}} - \frac{\sqrt{(E^2 - E_0^2)}}{E^2} \right) \right] \\ &= \left(\frac{p^2 c^3}{E} \right) \left[\frac{\partial U_E}{\partial E} \frac{\sqrt{(E^2 - E_0^2)}}{E} + U_E \left(\frac{E^2 - (E^2 - E_0^2)}{\sqrt{(E^2 - E_0^2)} E^2} \right) \right] \\ &= \left(\frac{p^2 c^3}{E} \right) \left[\frac{\partial U_E}{\partial E} \frac{\sqrt{(E^2 - E_0^2)}}{E} + U_E \left(\frac{E_0^2}{\sqrt{(E^2 - E_0^2)} E^2} \right) \right] \\ &= c \left(\frac{p^2 c^2}{E^2} \right) \left[\frac{\partial U_E}{\partial \ln E} \frac{\sqrt{(E^2 - E_0^2)}}{E} \right] + c \left(\frac{p^2 c^2}{E^2} \right) \left[U_E \left(\frac{E_0^2}{\sqrt{(E^2 - E_0^2)} E} \right) \right]. \end{aligned} \tag{A.10}$$

We need the rest of the terms also in terms of U_E, thus

$$\begin{aligned} \frac{\partial U_p}{\partial t} &= \frac{\partial}{\partial t} \left(U_E \frac{\sqrt{(E^2 - E_0^2)/c^2}}{E} c^2 \right) \\ &= c \frac{\sqrt{(E^2 - E_0^2)}}{E} \frac{\partial U_E}{\partial t}, \end{aligned} \tag{A.11}$$

and

$$\begin{aligned}\mathbf{V}\cdot(\nabla U_p) &= \mathbf{V}\cdot\left(\nabla cU_E\frac{\sqrt{(E^2-E_0^2)}}{E}\right)\\ &= c\mathbf{V}\cdot\left(\nabla U_E\frac{\sqrt{(E^2-E_0^2)}}{E}\right),\end{aligned} \tag{A.12}$$

and

$$\begin{aligned}\kappa\nabla^2 U_p &= \left(\kappa\nabla^2 cU_E\frac{\sqrt{(E^2-E_0^2)}}{E}\right)\\ &= c\left(\kappa\nabla^2 U_E\frac{\sqrt{(E^2-E_0^2)}}{E}\right),\end{aligned} \tag{A.13}$$

and

$$\begin{aligned}\frac{\partial}{\partial p}\left(\langle\dot{p}\rangle_{\rm rad}U_p\right) &= \frac{\partial}{\partial E}\left(\left[\frac{\partial p}{\partial E}\frac{\partial E}{\partial t}\right]U_E\frac{\partial E}{\partial p}\right)\frac{\partial E}{\partial p}\\ &= \frac{\partial}{\partial E}(\dot{E}_{\rm rad}U_E)\frac{pc^2}{E}.\end{aligned} \tag{A.14}$$

We now have all the terms for U_p in terms of U_E, and thus Eq. (A.6) becomes

$$\begin{aligned}c\frac{\sqrt{(E^2-E_0^2)}}{E}\frac{\partial U_E}{\partial t} =& -c\mathbf{V}\cdot\left(\nabla U_E\frac{\sqrt{(E^2-E_0^2)}}{E}\right)\\ &+c\left(\kappa\nabla^2 U_E\frac{\sqrt{(E^2-E_0^2)}}{E}\right)\\ &+\frac{1}{3}(\nabla\cdot\mathbf{V})\left\{c\left(\frac{p^2c^2}{E^2}\right)\left[\frac{\partial U_E}{\partial\ln E}\frac{\sqrt{(E^2-E_0^2)}}{E}\right]+\right.\\ &\left.c\left(\frac{p^2c^2}{E^2}\right)\left[U_E\left(\frac{E_0^2}{\sqrt{(E^2-E_0^2)}E}\right)\right]-2cU_E\frac{\sqrt{(E^2-E_0^2)}}{E}\right\}\\ &+\frac{\partial}{\partial E}(\dot{E}_{\rm rad}U_E)\frac{pc^2}{E}.\end{aligned} \tag{A.15}$$

It is possible to simplify Eq. (A.15) when considering relativistic particles (e.g., $E_{\rm e}\sim 10^{11}-10^{14}$ erg, $\gamma\sim 10^5-10^8$). We can then assume that the $E\gg E_0$, so that the particle energy $E\simeq pc$, therefore $\sqrt{(E^2-E_0^2)}/E\simeq 1$, $\gamma^{-1}\simeq 0$ and Eq. (A.15) reduces

to

$$\begin{aligned} c\frac{\partial U_E}{\partial t} &= -c\mathbf{V}\cdot(\nabla U_E) \\ &\quad + c\kappa\nabla^2 U_E \\ &\quad + \frac{1}{3}(\nabla\cdot\mathbf{V})\left(c\left[\frac{\partial U_E}{\partial \ln E}\right] + c\left[U_E\left(\frac{1}{\gamma^2}\right)\right] - 2cU_E\right) \\ &\quad + c\frac{\partial}{\partial E}(\dot{E}_{\rm rad}U_E). \end{aligned} \tag{A.16}$$

We finally arrive at (reinserting Q in terms of E now)

$$\frac{\partial U_E}{\partial t} = -\mathbf{V}\cdot(\nabla U_E) + \kappa\nabla^2 U_E + \frac{1}{3}(\nabla\cdot\mathbf{V})\left(\left[\frac{\partial U_E}{\partial \ln E}\right] - 2U_E\right) + \frac{\partial}{\partial E}(\dot{E}_{\rm rad}U_E) + Q(\mathbf{r}, E, t). \tag{A.17}$$

For the rest of the thesis, we use the symbol $N_{\rm e}$ to indicate U_E with the units $\mathrm{cm}^{-3}\mathrm{erg}^{-1}$.

A.2 Logarithmic Bins

In Section 4.2 the geometry of the model is discussed and the fact that some bin sizes are increased logarithmically is mentioned. This is in contrast to the linear case where the bins are all the same size. The way this is handled is shown here by looking at the lepton energies. If E_i are the discretised energies, then

$$E_i = E_{\rm min}e^{i\delta}, i = 0..M-1 \tag{A.18}$$

and

$$E_{\rm max} = E_{\rm min}e^{(M-1)\delta}, \tag{A.19}$$

with $E_{\rm min}$ and $E_{\rm max}$ the minimum and maximum lepton energies respectively, δ a step value for the lepton energies, and M the total number of bins allocated to the lepton energy vector. Equation (A.19) is used to calculate the size of δ by noting that

$$e^{(M-1)\delta} = \frac{E_{\rm max}}{E_{\rm min}} \tag{A.20}$$

thus

$$\delta = \frac{1}{M-1}\ln\left(\frac{E_{\rm max}}{E_{\rm min}}\right). \tag{A.21}$$

The bin widths are not constant, but can be calculated as follows,

$$\begin{aligned}(\triangle E)_i &= E_{i+1} - E_i \\ &= E_{\min} e^{(i+1)\delta} - E_{\min} e^{i\delta} \\ &= E_{\min}\left[e^{i\delta}\left(e^{\delta} - 1\right)\right].\end{aligned} \tag{A.22}$$

In our case the value for δ will always be much smaller than one, $\delta \ll 1$, and thus by using a Taylor expansion we can write $e^{\delta} \approx 1 + \delta$. Thus

$$\begin{aligned}(\triangle E)_i &\approx E_{\min}\left[e^{i\delta}\left(1 + \delta - 1\right)\right] \\ &= E_{\min} e^{i\delta}\delta \\ &= \delta E_i.\end{aligned} \tag{A.23}$$

A.3 $L(t)$ and $L_0(\tau_0)$

We derive expressions for $L(t)$ and $L_0(\tau_0)$ to show that $\tau_0 = \tau_c - t_{age}$. This derivation appeared in Van Rensburg et al. (2018). We make two assumptions: the first is that the B-field of the pulsar does not decay over short time scales, i.e., $\dot{P}P^{n-2} = \dot{P}_0 P_0^{n-2}$ (e.g., Venter and de Jager, 2007) and the second is a braking law of the form $\dot{\Omega} = k\Omega^n$ with k smaller than 0 (e.g., Pacini and Salvati, 1973, Rees and Gunn, 1974, Gaensler and Slane, 2006).

An expression for the spin-down luminosity $L(t)$ of the pulsar can be constructed by using the second assumption and the following definition $L(t) = I\Omega\dot{\Omega}$, thus $L(t) = kI\Omega^{n+1}$. We can integrate $\dot{\Omega}$ to find

$$\int_{\Omega_0}^{\Omega} \Omega^{-n} d\Omega = \int_0^t k dt, \tag{A.24}$$

thus

$$\frac{1}{1-n}\left(\Omega^{1-n} - \Omega_0^{1-n}\right) = kt \tag{A.25}$$

leaving us with

$$\Omega = \left(\frac{1}{(1-n)kt + \Omega_0^{1-n}}\right)^{\frac{1}{n-1}}. \tag{A.26}$$

Now we can obtain $L(t)$ by replacing the Ω with Eq. (A.26). Thus

$$L(t) = kI\left(\frac{1}{(1-n)kt + \Omega_0^{1-n}}\right)^{\frac{n+1}{n-1}}. \tag{A.27}$$

We set $\beta = (n+1)/(n-1)$ and do some manipulation to find

$$L(t) = kI\Omega_0^{n+1}\left(1 + \frac{(1-n)kt}{\Omega_0^{1-n}}\right)^{-\beta}. \tag{A.28}$$

We know from the definition of $L(t)$ that $L_0(t) = kI\Omega_0^{n+1}$ (assuming a constant values for I and k) and also that $(1-n)k/\Omega_0^{1-n} = (1-n)\dot{\Omega}_0/\Omega_0 = 1/\tau_0$ and thus

$$L(t) = \frac{L_0}{\left(1 + \frac{t}{\tau_0}\right)^{\beta}}. \tag{A.29}$$

In this first part we have shown how the spin-down luminosity is derived from the second assumption. When substituting $t = t_{\rm age}$ and $L_{\rm age} = L(t_{\rm age}) = 4\pi^2 I\dot{P}/P^3$, we find a first expression for L_0:

$$L_0 = L_{\rm age}\left(1 + \frac{t_{\rm age}}{\tau_0}\right)^{\beta}. \tag{A.30}$$

We will now obtain another expression for $L_0(\tau_0)$ using the first assumption $\dot{P}P^{n-2} = \dot{P}_0 P_0^{n-2} = K$, with K a constant. We rewrite this assumption as:

$$P_0 = \left(\frac{K}{\dot{P}_0}\right)^{\frac{1}{n-2}}. \tag{A.31}$$

Since $L_0 = 4\pi^2 I\dot{P}_0/P_0^3$

$$L_0 = \frac{4\pi^2 I\dot{P}_0}{\left(\frac{K}{\dot{P}_0}\right)^{3/(n-2)}}. \tag{A.32}$$

Following some manipulations, we find

$$L_0 = \frac{4\pi^2 I}{K^{3/(n-2)}} \cdot \dot{P}_0^{\frac{n+1}{n-2}}. \tag{A.33}$$

We can also find $\dot{P}_0$ as a function of τ_0 by using the definition for the birth characteristic age of the pulsar given by $\tau_0 = P_0/(n-1)\dot{P}_0$. Thus we have

$$\tau_0 = \frac{(K/\dot{P}_0)^{1/(n-2)}}{(n-1)\dot{P}_0}, \tag{A.34}$$

and once again we solve for $\dot{P}_0$, leaving us with

$$\dot{P}_0 = \left(\frac{K^{1/(n-2)}}{(n-1)\tau_0}\right)^{\frac{n-2}{n-1}}. \tag{A.35}$$

We can now substitute Eq. (A.35) into Eq (A.33) to find L_0 as a function of τ_0. We are thus left with

$$L_0 = \left(\frac{4\pi^2 I}{K^{3/(n-2)}}\right)\left(\left[\frac{K^{1/(n-2)}}{(n-1)\tau_0}\right]^{\frac{n-2}{n-1}}\right)^{\frac{n+1}{n-2}}, \tag{A.36}$$

resulting in

$$L_0 = 4\pi^2 I K^{-2/(n-1)}\left(\frac{1}{(n-1)\tau_0}\right)^{\frac{n+1}{n-1}}. \tag{A.37}$$

By substituting the constant $K = \dot{P}P^{n-2}$ back we find

$$L_0 = 4\pi^2 I \dot{P}^{\frac{-2}{(n-1)}} P^{\frac{-2(n-2)}{(n-1)}}\left(\frac{1}{(n-1)\tau_0}\right)^{\frac{n+1}{n-1}}, \tag{A.38}$$

and by using the definition for the current spin-down luminosity $L_{\rm age} = 4\pi^2 I\dot{P}/P^3$ we find

$$L_0 = L_{\rm age}\frac{P^3}{\dot{P}}\dot{P}^{\frac{-2}{(n-1)}} P^{\frac{-2(n-2)}{(n-1)}}\left(\frac{1}{(n-1)\tau_0}\right)^{\frac{n+1}{n-1}}. \tag{A.39}$$

Upon simplification we find

$$L_0 = L_{\rm age}\left(\frac{P}{\dot{P}(n-1)\tau_0}\right)^{\frac{n+1}{n-1}}. \tag{A.40}$$

We can simplify this further by using the definition for the characteristic age of the pulsar, thus

$$L_0 = L_{\rm age}\left(\frac{\tau_c}{\tau_0}\right)^{\beta}. \tag{A.41}$$

We now have two forms for the birth spin-down luminosity of the pulsar in Eq. (A.30) and (A.41) and by setting them equal

$$\left(\frac{\tau_c}{\tau_0}\right)^{\beta} = \left(1 + \frac{t_{\rm age}}{\tau_0}\right)^{\beta} \tag{A.42}$$

we find

$$\tau_0 = \tau_{\rm c} - t_{\rm age}. \tag{A.43}$$

This equation is used in Section 4.4. Therefore, we choose $t_{\rm age}$ and n, calculate $\tau_{\rm c}$ and $L_{\rm age}$ using the measured value of P and $\dot{P}$, calculate τ_0 from Eq. (A.43) and lastly L_0 from Eq. (A.41). All parameters are now known and we can obtain $L(t)$ from Eq. (A.29).

A.4 Normalisation of the Particle Injection Spectrum

In Eq. (4.6) I showed that the particle (lepton) injection spectrum at the termination shock in the PWN is modelled by a broken power law, with Q_0 the normalisation constant. I also showed that by using the spin-down luminosity $L(t) = L_0 \left(1 + t/\tau_0\right)^{-2}$ of the pulsar, with τ_0 the characteristic spin-down timescale of the pulsar and L_0 the initial spin-down luminosity, one can write

$$\epsilon L(t) = \int_{E_{\rm min}}^{E_{\rm b}} Q E_{\rm e} dE_{\rm e} + \int_{E_{\rm b}}^{E_{\rm max}} Q E_{\rm e} dE_{\rm e}, \tag{A.44}$$

with ϵ the conversion efficiency of the time-dependent spin-down luminosity $L(t)$ to power in the particle spectrum. This equation can be used to normalise Q_0. This is done by discretising Eq. (A.44) and assuming logarithmic bins in the energy dimension. Thus

$$\epsilon L(t) = \delta \frac{Q_0}{E_{\rm b}^{\alpha_1}} \sum_{i=0}^{i=i_{\rm b}} E_i^{\alpha_1+2} + \delta \frac{Q_0}{E_{\rm b}^{\alpha_2}} \sum_{i=i_{\rm b}+1}^{i=M-1} E_i^{\alpha_2+2}, \tag{A.45}$$

where $E_{\rm b}$ is the energy where the break in the lepton spectrum occurs and i_b is the corresponding bin index for the break energy. Eq. (A.45) can now be manipulated to give

$$Q_0(t) = \frac{\epsilon L(t)}{\delta} \left(E_b^{-\alpha_1} \sum_{i=0}^{i=i_b} E_i^{\alpha_1+2} + E_b^{-\alpha_2} \sum_{i=i_b+1}^{i=M-1} E_i^{\alpha_2+2} \right)^{-1}. \tag{A.46}$$

A.5 Discretisation of the Fokker-Planck-type Transport Equation

In this Section I will show how the following Fokker-Planck-type transport equation is discretised (see Eq. [A.17]):

$$\frac{\partial N_{\rm e}}{\partial t} = -\mathbf{V} \cdot (\nabla N_{\rm e}) + \kappa \nabla^2 N_{\rm e} + \frac{1}{3} (\nabla \cdot \mathbf{V}) \left(\left[\frac{\partial N_{\rm e}}{\partial \ln E} \right] - 2 N_{\rm e} \right) + \frac{\partial}{\partial E} (\dot{E}_{\rm rad} N_{\rm e}) + Q(\mathbf{r}, E, t). \tag{A.47}$$

Before we can start with the discretisation, we first consider the term $\frac{1}{3}(\nabla\cdot\mathbf{V})\left(\left[\frac{\partial N_\mathrm{e}}{\partial \ln E}\right]-2N_\mathrm{e}\right)$ and write it in the following form:

$$\begin{aligned}
&\frac{1}{3}(\nabla\cdot\mathbf{V})\left(\left[\frac{\partial N_\mathrm{e}}{\partial \ln E}\right]-2N_\mathrm{e}\right)\\
&=\frac{1}{3}(\nabla\cdot\mathbf{V})\frac{\partial N_\mathrm{e}}{\partial \ln E}-\frac{2}{3}(\nabla\cdot\mathbf{V})N_\mathrm{e}\\
&=\frac{1}{3}(\nabla\cdot\mathbf{V})E\frac{\partial N_\mathrm{e}}{\partial E}+\frac{1}{3}(\nabla\cdot\mathbf{V})N_\mathrm{e}-(\nabla\cdot\mathbf{V})N_\mathrm{e}\\
&=\frac{\partial}{\partial E}\left(\frac{1}{3}(\nabla\cdot\mathbf{V})EN_\mathrm{e}\right)-(\nabla\cdot\mathbf{V})N_\mathrm{e}\\
&=\frac{\partial}{\partial E}\left(\dot{E}_\mathrm{ad}N_\mathrm{e}\right)-(\nabla\cdot\mathbf{V})N_\mathrm{e},
\end{aligned}\tag{A.48}$$

where $\dot{E}_\mathrm{ad}$ is the energy change due to adiabatic heating or cooling. With the adiabatic energy change now in this form, we can add it to the radiation energy losses to give us a term for the total energy change $\dot{E}_\mathrm{tot}=\dot{E}_\mathrm{rad}+\dot{E}_\mathrm{ad}$. Thus the transport equation becomes:

$$\frac{\partial N_\mathrm{e}}{\partial t}=-\mathbf{V}\cdot(\nabla N_\mathrm{e})+\kappa\nabla^2 N_\mathrm{e}+\frac{\partial}{\partial E}(\dot{E}_\mathrm{tot}N_\mathrm{e})-(\nabla\cdot\mathbf{V})N_\mathrm{e}+Q(\mathbf{r},E,t).\tag{A.49}$$

As a first approach to discretise Eq. (A.49) an Euler method was used, but it soon became clear that this method was not stable. The next step was to discretise the equation by using a DuFort-Frankel scheme. This scheme is used to solve parabolic differential equations, i.e., equations of the form

$$\frac{\partial u}{\partial t}=\eta_0\frac{\partial^2 u}{\partial x^2}\tag{A.50}$$

can be discretised as

$$\frac{u_k^{(j+1)}-u_k^{(j-1)}}{2\triangle t}=\eta_0\frac{u_{k+1}^{(j)}-(u_k^{(j-1)}+u_k^{(j+1)})+u_{k-1}^{(j)}}{\triangle x^2}.\tag{A.51}$$

This scheme is stable for small time steps, where j is the time step and k the spatial step. A visual representation of this can be seen in Figure A.1.

To discretise Eq. (A.49) we first have to do a Taylor expansion of some function $f(x)$ to find the correct way to discretise the energy loss term, $\frac{\partial}{\partial E}(\dot{E}_\mathrm{tot}N_\mathrm{e})$ due to the different logarithmic bin sizes in energy. For two different bin sizes h_1 and h_2 we have

$$\begin{aligned}
f(x+h_1)&=f(x)+h_1f'(x)+\frac{h_1^2}{2}f''(x)\\
f(x-h_2)&=f(x)-h_2f'(x)+\frac{h_2^2}{2}f''(x).
\end{aligned}\tag{A.52}$$

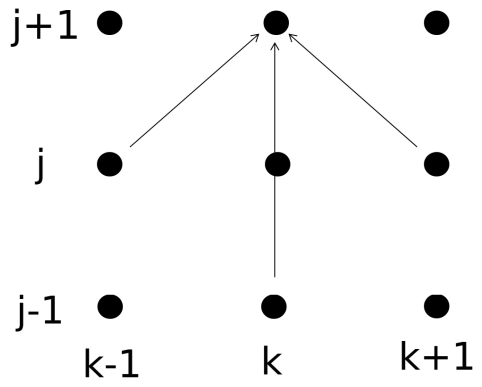

FIGURE A.1: DuFort-Frankel numerical scheme.

By multiplying by h_2^2 and h_1^2, we find

$$\begin{aligned} h_2^2 f(x+h_1) &= h_2^2 f(x) + h_2^2 h_1 f'(x) + \frac{h_2^2 h_1^2}{2} f''(x) \\ h_1^2 f(x-h_2) &= h_1^2 f(x) - h_1^2 h_2 f'(x) + \frac{h_1^2 h_2^2}{2} f''(x). \end{aligned} \tag{A.53}$$

By then subtracting the second equation from the first we find

$$\begin{aligned} h_2^2 f(x+h_1) - h_1^2 f(x-h_2) &= \left(h_2^2 - h_1^2\right) f(x) + \left(h_2^2 h_1 + h_1^2 h_2\right) f'(x) \\ \therefore f'(x) &= \frac{h_2^2 f(x+h_1) - h_1^2 f(x-h_2) + (h_1^2 - h_2^2) f(x)}{h_1 h_2 (h_2 + h_1)} \\ \therefore f'(x) &= \frac{1}{h_2 + h_1} \left[\frac{h_2}{h_1} f(x+h_1) - \frac{h_1}{h_2} f(x-h_2) + \left(\frac{h_1}{h_2} - \frac{h_2}{h_1} \right) f(x) \right]. \end{aligned} \tag{A.54}$$

For the case when $h_1 = h_2$ this reduces back to the usual expression for $f'(x)$. In using Eq. (A.54), $\frac{\partial}{\partial E}(\dot{E}_{\text{tot}} N_{\text{e}})$ becomes

$$\frac{\partial}{\partial E}(\dot{E}_{\text{tot}} N_{\text{e}}) = \frac{1}{dE_{i+1,j,k} + dE_{i,j,k}} \left[r_{\text{a}} (\dot{E}_{\text{tot}} N_{\text{e}})_{i+1,j,k} - \frac{1}{r_{\text{a}}} (\dot{E}_{\text{tot}} N_{\text{e}})_{i-1,j,k} + \left(\frac{1}{r_{\text{a}}} - r_{\text{a}} \right) (\dot{E}_{\text{tot}} N_{\text{e}})_{i,j,k} \right] \tag{A.55}$$

where $r_{\text{a}} = h_2/h_1 = dE_{i+1}/dE_i$, $dE_{i,j,k}$ is the energy bin size and i, j, k are the indices for energy, time, and space respectively. For simplicity, I am going to rename the energy term as $\frac{\partial}{\partial E}(\dot{E}_{\text{tot}} N_{\text{e}}) = X$, as the discretisation for this term in Eq. (A.47) is done for now and will be finalised in Eq. (A.63).

Next we consider the diffusion coefficient κ. We assume that it is not spatially dependent and therefore by assuming spherical symmetry we can rewrite $\kappa\nabla^2 N_\mathrm{e}$) as

$$\begin{aligned}\kappa\nabla^2 N_\mathrm{e} &= \kappa\frac{1}{r^2}\frac{\partial}{\partial r}\left(r^2\frac{\partial N_\mathrm{e}}{\partial r}\right)\\ &= \frac{2\kappa}{r}\frac{\partial N_\mathrm{e}}{\partial r} + \kappa\frac{\partial^2 N_\mathrm{e}}{\partial r^2}.\end{aligned} \tag{A.56}$$

The transport equation that has to be discretised, by adding the injection Q back, is thus

$$\frac{\partial N_\mathrm{e}}{\partial t} = Q + X + \frac{2\kappa}{r}\frac{\partial N_\mathrm{e}}{\partial r} + \kappa\frac{\partial^2 N_\mathrm{e}}{\partial r^2} - \mathbf{V}\cdot(\nabla N_\mathrm{e}) - (\nabla\cdot\mathbf{V})N_\mathrm{e}. \tag{A.57}$$

It can now be fully discretised by using the DuFort-Frankel scheme as given in Eq. (A.51).

$$\begin{aligned}\frac{(N_\mathrm{e})_{i,j+1,k} - (N_\mathrm{e})_{i,j-1,k}}{2\triangle t} &= Q_{i,j,1} + X\\ &+ \frac{2\kappa}{r}\frac{(N_\mathrm{e})_{i,j,k+1} - (N_\mathrm{e})_{i,j,k-1}}{2\triangle r}\\ &+ \kappa\frac{(N_\mathrm{e})_{i,j,k+1} - \left[(N_\mathrm{e})_{i,j-1,k} + (N_\mathrm{e})_{i,j+1,k}\right] + (N_\mathrm{e})_{i,j,k-1}}{\triangle r^2}\\ &- \frac{V_{i,j,k}}{2\triangle r}\left((N_\mathrm{e})_{i,j,k+1} - (N_\mathrm{e})_{i,j,k-1}\right)\\ &- (\nabla\cdot\mathbf{V})_{i,j,k}(N_\mathrm{e})_{i,j,k}.\end{aligned} \tag{A.58}$$

Note that the injection term $Q_{i,j,1}$ is only non-zero in the first spatial zone, since it is considered a boundary condition as discussed in Section 4.9. The term $(\nabla\cdot\mathbf{V})_{i,j,k}$ is calculated analytically as

$$(\nabla\cdot\mathbf{V})_{i,j,k} = (\alpha_V + 2)\left(\frac{V_{i,j,k}}{r_k}\right) \tag{A.59}$$

by using the parametrised form of the velocity given in Eq. (4.14).

It is possible to simplify Eq. (A.58) to be more useful as shown in the next sets of equations:

$$\begin{aligned}(N_{\mathrm{e}})_{i,j+1,k} - (N_{\mathrm{e}})_{i,j-1,k} = {} & 2Q_{i,j,1}\triangle t + 2X\triangle t \\ & + \frac{2\kappa\triangle t}{r\triangle r}\left((N_{\mathrm{e}})_{i,j,k+1} - (N_{\mathrm{e}})_{i,j,k-1}\right) \\ & + \frac{2\kappa\triangle t}{\triangle r^2}\left((N_{\mathrm{e}})_{i,j,k+1} - \left[(N_{\mathrm{e}})_{i,j-1,k} + (N_{\mathrm{e}})_{i,j+1,k}\right] + (N_{\mathrm{e}})_{i,j,k-1}\right) \\ & - V_{i,j,k}\left(\frac{\triangle t}{\triangle r}\right)\left((N_{\mathrm{e}})_{i,j,k+1} - (N_{\mathrm{e}})_{i,j,k-1}\right) \\ & - 2(\nabla\cdot\mathbf{V})_{i,j,k}(N_{\mathrm{e}})_{i,j,k}\triangle t.\end{aligned} \tag{A.60}$$

By replacing $\frac{\partial}{\partial E}(\dot{E}_{\mathrm{tot}}N_{\mathrm{e}}) = X$, grouping similar terms in Eq. (A.60) and setting $\beta = \frac{2\kappa\triangle t}{(\triangle r)^2}$, $\gamma = \frac{2\kappa\triangle t}{r\triangle r}$, and $\eta = \frac{V_{i,j,k}\triangle t}{\triangle r}$ and writing $\dot{E}_{\mathrm{tot}}\triangle t = dE_{\mathrm{loss}}$, we find that

$$\begin{aligned}(1+\beta)(N_{\mathrm{e}})_{i,j+1,k} = {} & (1-\beta)(N_{\mathrm{e}})_{i,j-1,k} \\ & + (\beta+\gamma-\eta)(N_{\mathrm{e}})_{i,j,k+1} \\ & + (\beta-\gamma+\eta)(N_{\mathrm{e}})_{i,j,k-1} \\ & + \left[\frac{2\triangle t}{dE_{i+1,j,k}+dE_{i,j,k}}\right]\left[r_{\mathrm{a}}\dot{E}_{i+1,j,k}(N_{\mathrm{e}})_{i+1,j,k} - \frac{1}{r_{\mathrm{a}}}\dot{E}_{i-1,j,k}(N_{\mathrm{e}})_{i-1,j,k}\right] \\ & + \left[\frac{2\triangle t}{dE_{i+1,j,k}+dE_{i,j,k}}\right]\left[\frac{1}{r_{\mathrm{a}}} - r_{\mathrm{a}}\right]\left[\dot{E}_{i,j,k}\left(\frac{(N_{\mathrm{e}})_{i,j+1,k}+(N_{\mathrm{e}})_{i,j-1,k}}{2}\right)\right] \\ & - 2(\nabla\cdot\mathbf{V})_{i,j,k}(N_{\mathrm{e}})_{i,j,k}\triangle t \\ & + 2Q_{i,j,1}\triangle t.\end{aligned} \tag{A.61}$$

Note that the term $\left(\frac{(N_{\mathrm{e}})_{i,j+1,k}+(N_{\mathrm{e}})_{i,j-1,k}}{2}\right)$ is the average of N_{e} over two time steps. Equation (A.61) can now be finalised by setting

$$z = \left[\frac{1}{dE_{i+1,j,k}+dE_{i,j,k}}\right]\left[\frac{1}{r_{\mathrm{a}}} - r_{\mathrm{a}}\right](dE_{\mathrm{loss}})_{i,j,k} \tag{A.62}$$

and thus the final equation that can now be implemented in the code is

$$\begin{aligned}(1-z+\beta)(N_{\mathrm{e}})_{i,j+1,k} =& 2Q_{i,j,1}\triangle t \\ &+ (1+z-\beta)(N_{\mathrm{e}})_{i,j-1,k} \\ &+ (\beta+\gamma-\eta)(N_{\mathrm{e}})_{i,j,k+1} \\ &+ (\beta-\gamma+\eta)(N_{\mathrm{e}})_{i,j,k-1} \\ &- 2(\nabla\cdot\mathbf{V})_{i,j,k}\triangle t(N_{\mathrm{e}})_{i,j,k} \\ &+ \frac{2}{(dE_{i+1,j,k}+dE_{i,j,k})} \\ &\left(r_{\mathrm{a}}\left(dE_{\mathrm{loss}}\right)_{i+1,j,k}\left(N_{\mathrm{e}}\right)_{i+1,j,k} - \frac{1}{r_{\mathrm{a}}}\left(dE_{\mathrm{loss}}\right)_{i-1,j,k}\left(N_{\mathrm{e}}\right)_{i-1,j,k}\right).\end{aligned} \tag{A.63}$$

Bibliography

Abdalla, H. et al. (2018a). The H.E.S.S. Galactic Plane Survey. *A&AS*, 612:A1.

Abdalla, H. et al. (2018b). The population of TeV Pulsar Wind Nebulae in the H.E.S.S. Galactic Plane Survey. *A&AS*, 612:A2.

Abdo, A. A., Ackermann, M., Ajello, M., Atwood, W. B., Axelsson, M., Baldini, L., Ballet, J., Barbiellini, G., Baring, M. G., Bastieri, D., and et al. (2010). The First Fermi Large Area Telescope Catalog of Gamma-ray Pulsars. *ApJS*, 187:460.

Abdo, A. A., Ajello, M., Allafort, A., Baldini, L., Ballet, J., Barbiellini, G., Baring, M. G., Bastieri, D., Belfiore, A., Bellazzini, R., and et al. (2013). The Second Fermi Large Area Telescope Catalog of Gamma-Ray Pulsars. *ApJS*, 208:17.

Abramowski, A. et al. (2012a). Identification of HESS J1303-631 as a Pulsar Wind Nebula through γ-ray, X-ray, and Radio Observations. *A&AS*, 548:A46.

Abramowski, A. et al. (2012b). Probing the Extent of the Non-thermal Emission from the Vela X Region at TeV Energies with H.E.S.S. *A&AS*, 548:A38.

Acero, F. (2017). Pulsar Wind Nebulae Viewed Through the Gamma-Ray Eye. In Torres, D. F., editor, *Modelling Pulsar Wind Nebulae*, volume 446, page 47.

Acharya, B. S. et al. (2019). *Science with the Cherenkov Telescope Array*.

Aharonian, F. et al. (2005). Very High Energy Gamma Rays from the Composite SNR G 0.9+0.1. *A&AS*, 432:L25.

Aleksić, J. et al. (2014). Discovery of TeV γ-ray Emission from the Pulsar Wind Nebula 3C 58 by MAGIC. *A&AS*, 567:L8.

Amato, E. (2003). Understanding Pulsar Wind Nebulae: Recent Progress and open Questions. *Chinese Journal of Astronomy and Astrophysics Supplement*, 3:316.

Amato, E. (2014). The Theory of Pulsar Wind Nebulae. *International Journal of Modern Physics Conference Series*, 28:60160.

Aschenbach, B. (1998). Discovery of a Young Nearby Supernova Remnant. *Nature*, 396(6707):141.

Atwood, W. B. et al. (2009). The Large Area Telescope on the Fermi Gamma-Ray Space Telescope Mission. *ApJ*, 697(2):1071.

Axford, W. I., Leer, E., and Skadron, G. (1977). The Acceleration of Cosmic Rays by Shock Waves. *International Cosmic Ray Conference*, 11:132.

Baade, W. (1942). The Crab Nebula. *ApJ*, 96:188.

Bandiera, R., Neri, R., and Cesaroni, R. (2002). The Crab Nebula at 1.3 mm. Evidence for a new Synchrotron Component. *A&AS*, 386:1044.

Begelman, M. C. and Li, Z.-Y. (1992). An Axisymmetric Magnetohydrodynamic Model for the Crab Pulsar Wind Bubble. *ApJ*, 397:187.

Belvedere, R., Rueda, J. A., and Ruffini, R. (2015). On the Magnetic Field of Pulsars with Realistic Neutron Star Configurations. *ApJ*, 799(1):23.

Bevington, P. R. (1969). *Data Reduction and Error Analysis for the Physical Sciences*.

Bezuidenhout, T., Venter, C., Seyffert, A., and Harding, A. K. (2017). Assessment of a Statistical Approach Towards Constraining Pulsar Geometry via Multiband Light Curve Fitting. In *5th Annual Conference on High Energy Astrophysics in Southern Africa*, page 18.

Bietenholz, M. F. and Bartel, N. (2008). The Expansion and Radio Spectral index of G21.5-0.9: is PSR J1833-1034 the Youngest Pulsar? *MNRAS*, 386:1411.

Blondin, J. M., Chevalier, R. A., and Frierson, D. M. (2001). Pulsar Wind Nebulae in Evolved Supernova Remnants. *ApJ*, 563:806.

Blumenthal, G. R. and Gould, R. J. (1970). Bremsstrahlung, Synchrotron Radiation, and Compton Scattering of High-Energy Electrons Traversing Dilute Gases. *Reviews of Modern Physics*, 42:237.

Bucciantini, N. (2014). Pulsar Wind Nebulae Modeling. *International Journal of Modern Physics Conference Series*, 28:60162.

Bucciantini, N. (2018). Future X-ray Polarimetry of Relativistic Accelerators: Pulsar Wind Nebulae and Supernova Remnants. *Galaxies*, 6(2):42.

Burn, B. J. (1966). On the Depolarization of Discrete Radio Sources by Faraday Dispersion. *MNRAS*, 133:67.

Camilo, F., Ransom, S. M., Gaensler, B. M., and Lorimer, D. R. (2009). Discovery of the Energetic Pulsar J1747-2809 in the Supernova Remnant G0.9+0.1. *ApJ*, 700:L34.

Camilo, F., Ransom, S. M., Gaensler, B. M., Slane, P. O., Lorimer, D. R., Reynolds, J., Manchester, R. N., and Murray, S. S. (2006). PSR J1833-1034: Discovery of the Central Young Pulsar in the Supernova Remnant G21.5-0.9. *ApJ*, 637:456.

Chalme-Calvet, R., de Naurois, M., Tavernet, J.-P., and for the H. E. S. S. Collaboration (2014). Muon Efficiency of the H.E.S.S. Telescope. *Proceedings of the Atmospheric Monitoring for High-Energy Astroparticle Detectors (AtmoHEAD) Conference, Saclay (France), June 10-12, 2013.*

Chen, F. F. (1984). *Introduction to Plasma Physics and Controlled Fusion (New York: Plenum Press).*

Chevalier, R. A. (2004). Pulsar Wind Nebulae: Theoretical Aspects and Observational Constraints. *Advances in Space Research*, 33(4):456.

Chevalier, R. A. (2005). Young Core-Collapse Supernova Remnants and Their Supernovae. *ApJ*, 619(2):839.

Cocke, W. J., Disney, M. J., and Taylor, D. J. (1969). Discovery of Optical Signals from Pulsar NP 0532. *Nature*, 221:525.

Combes, F. (2015). The Square Kilometer Array: Cosmology, Pulsars and other Physics with the SKA. *Journal of Instrumentation*, 10(9):C09001.

Comella, J. M., Craft, H. D., Lovelace, R. V. E., and Sutton, J. M. (1969). Crab Nebula Pulsar NP 0532. *Nature*, 221(5179):453.

De Jager, O. and Venter, C. (2005). Ground-based Gamma-Ray Observations of Pulsars and their Nebulae: Towards a New Order. In Degrange, B. and Fontaine, G., editors, *Towards a Network of Atmospheric Cherenkov Detectors VII (astro-ph/0511098).*

De Jager, O. C. and Djannati-Ataï, A. (2009). Implications of HESS Observations of Pulsar Wind Nebulae. In Becker, W., editor, *Astrophysics and Space Science Library*, volume 357, page 451.

De Naurois, M. (2019). The H.E.S.S. Experiment: Current Status and Future Prospects. In *36th International Cosmic Ray Conference (ICRC2019)*, volume 36 of *International Cosmic Ray Conference*, page 656.

De Naurois, M. and Mazin, D. (2015). Ground-based Detectors in Very-High-Energy Gamma-Ray Astronomy. *Comptes Rendus Physique*, 16:610–627.

De Oña-Wilhelmi, E. et al. (2013). Prospects for Observations of Pulsars and Pulsar Wind Nebulae with CTA. *Astroparticle Physics*, 43:287.

de Oña Wilhelmi, E. et al. (2017). Unveiling the magnetic structure of VHE SNRs/PWNe with XIPE, the x-ray imaging-polarimetry explorer. In *6th International Symposium on High Energy Gamma-Ray Astronomy*, volume 1792 of *American Institute of Physics Conference Series*, page 070023.

Djannati-Ataï, A., deJager, O. C., Terrier, R., Gallant, Y. A., and Hoppe, S. (2008). New Companions for the Lonely Crab? VHE Emission from Young Pulsar Wind Nebulae Revealed by H.E.S.S. *International Cosmic Ray Conference*, 2:823.

Dubner, G., Giacani, E., and Decourchelle, A. (2008). High Resolution Radio Study of the Pulsar Wind Nebula within the Supernova Remnant G0.9+0.1. *A&AS*, 487:1033.

Duncan, A. R., Stewart, R. T., Haynes, R. F., and Jones, K. L. (1995). A Deep Radio Continuum Survey of the Southern Galactic Plane at 2.4 GHz. *MNRAS*, 277(1):36.

Ferrara, E. C., Ballet, J., Cavazzuti, E., and Digel, S. (2015). The Fermi Large Area Telescope Third Gamma-ray Source Catalog. *IAU General Assembly*, 22:2255765.

Ferreira, S. E. S. and de Jager, O. C. (2008a). Supernova Remnant Evolution in Uniform and Non-uniform Media. *A&AS*, 478:17.

Ferreira, S. E. S. and de Jager, O. C. (2008b). Supernova Remnant Evolution in Uniform and Non-uniform Media. *A&AS*, 478:17–29.

Fritz, G., Henry, R. C., Meekins, J. F., Chubb, T. A., and Friedman, H. (1969). X-ray Pulsar in the Crab Nebula. *Science*, 164(3880):709.

Gaensler, B. M. and Slane, P. O. (2006). The Evolution and Structure of Pulsar Wind Nebulae. *ARA&A*, 44:17.

Gaensler, B. M., Stappers, B. W., Frail, D. A., and Johnston, S. (1998). A Search for Pulsar Wind Nebulae using Pulsar Gating. *MmSAI*, 69:813.

Gallant, Y. A. and Tuffs, R. J. (1998). Infrared Observations of Plerions with ISO. 69:963.

Gaug, M., Fegan, S., Mitchell, A., Maccarone, M. C., Mineo, T., and Okumura, A. (2019). Using Muon Rings for the Optical Throughput Calibration of the Cherenkov Telescope Array. In *36th International Cosmic Ray Conference (ICRC2019)*, volume 36 of *International Cosmic Ray Conference*, page 684.

Gelfand, J., Breton, R., Ng, C.-Y., Hessels, J., Stappers, B., Roberts, M., and Possenti, A. (2015). Pulsar Wind Nebulae in the SKA era. *Advancing Astrophysics with the Square Kilometre Array (AASKA14)*, page 46.

Gelfand, J. D. (2017). Radiative Models of Pulsar Wind Nebulae. In Torres, D. F., editor, *Modelling Pulsar Wind Nebulae*, volume 446, page 161.

Gelfand, J. D., Slane, P. O., and Zhang, W. (2009). A Dynamical Model for the Evolution of a Pulsar Wind Nebula Inside a Nonradiative Supernova Remnant. *ApJ*, 703(2):2051.

Giebels, B. et al. (2013). Status and Recent Results from H.E.S.S. 4$^{\text{th}}$ *Fermi Symp. proc., eConf C121028 (arXiv:1303.2850).*

Gold, T. (1969). Pulsars and the Mass Spectrum of Cosmic Rays. *Nature*, 223:162.

Green, D. A. (1994). The Spectral Turnover of the 'Filled-Center' Supernova Remnant 3C 58: Implications for when Acceleration Occurs. *ApJS*, 90:817.

Green, D. A. (2014). A Catalogue of 294 Galactic Supernova Remnants. *Bulletin of the Astronomical Society of India*, 42(2):47.

Grondin, M. H., Romani, R. W., Lemoine-Goumard, M., Guillemot, L., Harding, A. K., and Reposeur, T. (2013). The Vela-X Pulsar Wind Nebula Revisited with Four Years of Fermi Large Area Telescope Observations. *ApJ*, 774(2):110.

Helfand, D. J. and Becker, R. H. (1987). G0.9 + 0.1 and the Emerging Class of Composite Supernova Remnants. *ApJ*, 314:203.

Hewitt, J. W. and Lemoine-Goumard, M. (2015). Observations of Supernova Remnants and Pulsar Wind Nebulae at Gamma-ray Energies. *Comptes Rendus Physique*, 16:674.

Hillier, R. R., Jackson, W. R., Murray, A., Redfern, R. M., and Sale, R. G. (1970). Low-Energy Gamma Rays from NP 0532. *ApJ*, 162:L177.

Hinton, J. A., Funk, S., Parsons, R. D., and Ohm, S. (2011). Escape from Vela X. *ApJ*, 743:L7.

Hinton, J. A. and Starling, R. L. C. (2013). High-Energy Emission from Transients. *Philosophical Transactions of the Royal Society of London Series A*, 371:20279.

Holler, M., Schöck, F. M., Eger, P., Kießling, D., Valerius, K., and Stegmann, C. (2012a). Spatially Resolved X-ray Spectroscopy and Modeling of the Nonthermal Emission of the Pulsar Wind Nebula in G0.9+0.1. *A&AS*, 539:A24.

Holler, M., Schöck, F. M., Eger, P., Kießling, D., Valerius, K., and Stegmann, C. (2012b). Spatially Resolved X-ray Spectroscopy and Modeling of the Nonthermal Emission of the Pulsar Wind Nebula in G0.9+0.1. *A&AS*, 539:A24.

Jones, F. C. (1968). Calculated Spectrum of Inverse-Compton-Scattered Photons. *Physical Review*, 167:1159.

Kargaltsev, O., Cerutti, B., Lyubarsky, Y., and Striani, E. (2015). Pulsar-Wind Nebulae. Recent Progress in Observations and Theory. *Space Sci. Rev.*, 191:391.

Kargaltsev, O. and Pavlov, G. G. (2008). Pulsar Wind Nebulae in the Chandra Era. In Bassa, C., Wang, Z., Cumming, A., and Kaspi, V. M., editors, *40 Years of Pulsars: Millisecond Pulsars, Magnetars and More*, volume 983 of *American Institute of Physics Conference Series*, page 171.

Kargaltsev, O., Pavlov, G. G., and Durant, M. (2012). Pulsar Wind Nebulae from X-rays to VHE γ-rays. In Lewandowski, W., Maron, O., and Kijak, J., editors, *Electromagnetic Radiation from Pulsars and Magnetars*, volume 466 of *Astronomical Society of the Pacific Conference Series*, page 167.

Kennel, C. F. and Coroniti, F. V. (1984a). Confinement of the Crab Pulsar's Wind by its Supernova Remnant. *ApJ*, 283:694.

Kennel, C. F. and Coroniti, F. V. (1984b). Magnetohydrodynamic Model of Crab Nebula Radiation. *ApJ*, 283:710.

Kopp, A., Venter, C., Büsching, I., and de Jager, O. C. (2013). Multi-wavelength Modeling of Globular Clusters − The Millisecond Pulsar Scenario. *ApJ*, 779:126.

Kothes, R. (1998). A Correlation Between the Rotational Energy Loss Rate E of Pulsars and the Radio Surface Brightness SIGMA of their Synchrotron Nebulae. *MmSAI*, 69:971.

Kothes, R. (2013). Distance and Age of the Pulsar Wind Nebula 3C 58. *A&AS*, 560:A18.

Kothes, R. (2017). Radio Properties of Pulsar Wind Nebulae. In Torres, D. F., editor, *Modelling Pulsar Wind Nebulae*, volume 446, page 1.

Lagage, P. O. and Cesarsky, C. J. (1983). The Maximum Energy of Cosmic Rays Accelerated by Supernova Shocks. *A&AS*, 125:249.

Li, J., Torres, D. F., Lin, T. T., Grondin, M.-H., Kerr, M., Lemoine-Goumard, M., and de Oña Wilhelmi, E. (2018). Observing and Modeling the Gamma-Ray Emission from Pulsar/Pulsar Wind Nebula Complex PSR J0205+6449/3C 58. *ApJ*, 858:84.

Longair, M. S. (2011). *High Energy Astrophysics (Cambridge, UK: Cambridge University Press).*

Lorimer, D. R. and Kramer, M. (2005). *Handbook of Pulsar Astronomy (Cambridge, UK: Cambridge University Press).*

Lu, F.-W., Gao, Q.-G., and Zhang, L. (2017a). A Self-consistent and Spatially Dependent Model of the Multiband Emission of Pulsar Wind Nebulae. *ApJ*, 834(1):43.

Lu, F.-W., Gao, Q.-G., Zhu, B.-T., and Zhang, L. (2017b). Spatially Radiative Properties of 3C 58 and G21.5-0.9. *MNRAS*, 472(3):2926.

Lu, F.-W., Gao, Q.-G., Zhu, B.-T., and Zhang, L. (2017c). Spatially Radiative Properties of 3C 58 and G21.5-0.9. *MNRAS*, 472(3):2926.

Lu, F.-W., Gao, Q.-G., Zhu, B.-T., and Zhang, L. (2019). High Energy Spatially Radiative Properties of Vela X Pulsar Wind Nebula. *A&AS*, 624:A144.

Lyne, A. G. (2006). *Pulsar Astronomy (Cambridge, UK: Cambridge University Press)*.

Martin, J., Torres, D. F., Cillis, A., and de Oña Wilhelmi, E. (2014). Is there Room for highly Magnetized Pulsar Wind Nebulae among those Non-detected at TeV? *MNRAS*, 443(1):138.

Martín, J., Torres, D. F., and Pedaletti, G. (2016). Molecular Environment, Reverberation, and Radiation from the Pulsar Wind Nebula in CTA 1. *MNRAS*, 459(4):3868.

Martín, J., Torres, D. F., and Rea, N. (2012). Time-dependent Modelling of Pulsar Wind Nebulae: Study on the Impact of the Diffusion-loss approximations. *MNRAS*, 427:415.

Matheson, H. and Safi-Harb, S. (2005). The Plerionic Supernova Remnant G21.5-0.9: In and out. *Advances in Space Research*, 35:1099.

Mayall, N. U. and Oort, J. H. (1942). Further Data Bearing on the Identification of the Crab Nebula with the Supernova of 1054 A.D. Part II. The Astronomical Aspects. *PASP*, 54(318):95.

McEnery, J. et al. (2019). All-sky Medium Energy Gamma-ray Observatory: Exploring the Extreme Multimessenger Universe. In *BAAS*, volume 51, page 245.

McKee, C. F. (1974). X-Ray Emission from an Inward-Propagating Shock in Young Supernova Remnants. *ApJ*, 188:335.

McKee, C. F. and Truelove, J. K. (1995). Explosions in the Interstellar Medium. *Physics Reports*, 256(1):157.

Meegan, C. et al. (2009). The Fermi Gamma-ray Burst Monitor. *ApJ*, 702(1):791.

Michelson, P. F., Atwood, W. B., and Ritz, S. (2010). Fermi Gamma-ray Space Telescope: High-energy Results from the first year. *Reports on Progress in Physics*, 73(7):074901.

Minkowski, R. (1941). Spectra of Supernovae. *PASP*, 53(314):224.

Minkowski, R. (1942). The Crab Nebula. *ApJ*, 96:199.

Molla, M. C. and Lincetto, M. (2019). Core-Collapse Supernova Neutrino detection with KM3NeT. In *European Physical Journal Web of Conferences*, volume 207 of *European Physical Journal Web of Conferences*, page 05007.

Moraal, H. (2013). Cosmic-Ray Modulation Equations. *Space Sci. Rev.*, 176:299.

Murray, S. S., Slane, P. O., Seward, F. D., Ransom, S. M., and Gaensler, B. M. (2002). Discovery of X-Ray Pulsations from the Compact Central Source in the Supernova Remnant 3C 58. *ApJ*, 568:226.

Nynka, M., Hailey, C. J., Reynolds, S. P., et al. (2014). NuSTAR Study of Hard X-Ray Morphology and Spectroscopy of PWN G21.5-0.9. *ApJ*, 789:72.

O'Dell, S. L. et al. (2019). The Imaging X-Ray Polarimetry Explorer (IXPE): technical overview II. volume 11118 of *Society of Photo-Optical Instrumentation Engineers (SPIE) Conference Series*, page 111180V.

Olmi, B. and Bucciantini, N. (2019). Full-3D Relativistic MHD Simulations of Bow Shock Pulsar Wind Nebulae: Dynamics. *MNRAS*, 484(4):5755.

Ong, R. A. et al. (2019). The Cherenkov Telescope Array Science Goals and Current Status. In *European Physical Journal Web of Conferences*, volume 209 of *European Physical Journal Web of Conferences*, page 01038.

Ostriker, J. P. and Gunn, J. E. (1969). On the Nature of Pulsars. I. Theory. *ApJ*, 157:1395.

Pacini, F. and Salvati, M. (1973). On the Evolution of Supernova Remnants. Evolution of the Magnetic Field, Particles, Content, and Luminosity. *ApJ*, 186:249.

Perlmutter, S., Aldering, G., della Valle, M., et al. (1998). Discovery of a Supernova Explosion at half the age of the Universe. *Nature*, 391(6662):51.

Porquet, D., Decourchelle, A., and Warwick, R. S. (2003). XMM-Newton Spectral Analysis of the Pulsar Wind Nebula within the Composite SNR G0.9+0.1. *A&AS*, 401:197.

Porth, O., Komissarov, S. S., and Keppens, R. (2013). Solution to the Sigma Problem of Pulsar Wind Nebulae. *MNRAS*, 431:L48–L52.

Porth, O., Komissarov, S. S., and Keppens, R. (2014). Three-dimensional Magnetohydrodynamic Simulations of the Crab Nebula. *MNRAS*, 438(1):278.

Porth, O., Vorster, M. J., Lyutikov, M., and Engelbrecht, N. E. (2016). Diffusion in Pulsar Wind Nebulae: an Investigation using Magnetohydrodynamic and Particle Transport Models. *MNRAS*, 460:4135.

Rees, M. J. and Gunn, J. E. (1974). The Origin of the Magnetic Field and Relativistic Particles in the Crab Nebula. *MNRAS*, 167:1.

Reynolds, S. P. (2016). Magnetic fields in Supernova Remnants and Pulsar-Wind Nebulae: Deductions from X-ray Observations. In *Supernova Remnants: An Odyssey in Space after Stellar Death*, page 61.

Reynolds, S. P. and Chevalier, R. A. (1984). Evolution of Pulsar-Driven Supernova Remnants. *ApJ*, 278:630.

Reynolds, S. P., Gaensler, B. M., and Bocchino, F. (2012). Magnetic Fields in Supernova Remnants and Pulsar-Wind Nebulae. *Space Sci. Rev.*, 166(1-4):231.

Richards, D. W. and Comella, J. M. (1969). The Period of Pulsar NP 0532. *Nature*, 222:551.

Roberts, D. A., Goss, W. M., Kalberla, P. M. W., Herbstmeier, U., and Schwarz, U. J. (1993). High Resolution HI Observations of 3C58. *A&AS*, 274:427.

Roberts, M. S. E., Lyutikov, M., Gaensler, B. M., Brogan, C. L., Tam, C. R., and Romani, R. W. (2005). Ain't no Crab, PWN Got a Brand New Bag: Correlated Radio and X-ray Structures in Pulsar Wind Nebulae. In Sjouwerman, L. O. and Dyer, K. K., editors, *X-Ray and Radio Connections*, page #5.06.

Rybicki, G. B. and Lightman, A. P. (1979). *Radiative Processes in Astrophysics (New York: Wiley-Interscience)*.

Salter, C. J., Reynolds, S. P., Hogg, D. E., Payne, J. M., and Rhodes, P. J. (1989). 84 Gigahertz Observations of five Crab-like Supernova Remnants. *ApJ*, 338:171.

Schaefer, B. E. and Pagnotta, A. (2012). An Absence of Ex-companion Stars in the Type Ia Supernova Remnant SNR 0509-67.5. *Nature*, 481:164.

Schartel, N., Jansen, F., and Ward, M. J. (2017). XMM-Newton: Status and Scientific Perspective. *Astronomische Nachrichten*, 338(354):354.

Schöck, F. M., Büsching, I., de Jager, O. C., Eger, P., and Vorster, M. J. (2010). Spatially Resolved XMM-Newton Analysis and a Model of the Nonthermal Emission of MSH 15-52. *A&AS*, 515:A109.

Schutte, W. D. and Swanepoel, J. W. H. (2016). SOPIE: an R package for the Non-parametric Estimation of the Off-pulse Interval of a Pulsar Light Curve. *MNRAS*, 461(1):627.

Sefako, R. R. and de Jager, O. C. (2003). Constraints on Pulsar Magnetospheric and Wind Parameters for the Compact Nebulae of Vela and PSR B1706-44. *ApJ*, 593:1013.

Sidoli, L., Bocchino, F., Mereghetti, S., and Bandiera, R. (2004). XMM-Newton Observation of the Composite SNR G0.9+0.1 and the Discovery of a New Transient Source. *MmSAI*, 75:507.

Slane, P. (2017). *Pulsar Wind Nebulae*, page 2159.

Slane, P., Helfand, D. J., Reynolds, S. P., Gaensler, B. M., Lemiere, A., and Wang, Z. (2008). The Infrared Detection of the Pulsar Wind Nebula in the Galactic Supernova Remnant 3C 58. *ApJ*, 676:L33.

Slane, P., Helfand, D. J., van der Swaluw, E., and Murray, S. S. (2004). New Constraints on the Structure and Evolution of the Pulsar Wind Nebula 3C 58. *ApJ*, 616:403.

Spitkovsky, A. (2008). Particle Acceleration in Relativistic Collisionless Shocks: Fermi Process at Last? *ApJ*, 682:L5.

Stephenson, F. R. and Green, D. A. (2002). Historical Supernovae and Their Remnants. *Historical supernovae and their remnants, by F. Richard Stephenson and David A. Green. International series in astronomy and astrophysics, vol. 5. Oxford: Clarendon Press, 2002, ISBN 0198507666*, 5.

Summerlin, E. J. and Baring, M. G. (2012). Diffusive Acceleration of Particles at Oblique, Relativistic, Magnetohydrodynamic Shocks. *ApJ*, 745:63.

Tammann, G. A., Loeffler, W., and Schroeder, A. (1994). The Galactic Supernova Rate. *ApJS*, 92:487.

Tanaka, S. J. and Takahara, F. (2011). Study of Four Young TeV Pulsar Wind Nebulae with a Spectral Evolution Model. *ApJ*, 741:40.

Tanaka, S. J. and Takahara, F. (2013). Properties of Young Pulsar Wind Nebulae: TeV Detectability and Pulsar Properties. *MNRAS*, 429:2945.

Teegarden, B. J. and Sturner, S. J. (1999). INTEGRAL Observations of Gamma-Ray Bursts. In *AAS/High Energy Astrophysics Division #4*, AAS/High Energy Astrophysics Division, page 17.01.

Temim, T., Gehrz, R. D., Woodward, C. E., et al. (2006). Spitzer Space Telescope Infrared Imaging and Spectroscopy of the Crab Nebula. *AJ*, 132(4):1610.

Temim, T. and Slane, P. (2017). Optical and Infrared Observations of Pulsar Wind Nebulae. In Torres, D. F., editor, *Modelling Pulsar Wind Nebulae*, volume 446 of *Astrophysics and Space Science Library*, page 29.

Tian, W. W. and Leahy, D. A. (2008). The Distances of Supernova Remnants Kes 69 and G21.5-0.9 from HI and ^{13}CO Spectra. *MNRAS*, 391:L54.

Tibaldo, L., Zanin, R., Faggioli, G., Ballet, J., Grondin, M. H., Hinton, J. A., and Lemoine-Goumard, M. (2018). Disentangling Multiple High-Energy Emission Components in the Vela X Pulsar Wind Nebula with the Fermi Large Area Telescope. *A&AS*, 617:A78.

Torii, K., Slane, P. O., Kinugasa, K., Hashimotodani, K., and Tsunemi, H. (2000). ASCA Observations of the Crab-Like Supernova Remnant 3C 58. *PASJ*, 52:875.

Torres, D. F., Cillis, A., Martín, J., and de Oña Wilhelmi, E. (2014). Time-dependent Modeling of TeV-detected, Young Pulsar Wind Nebulae. *Journal of High Energy Astrophysics*, 1:31.

Torres, D. F., Cillis, A. N., and Martín Rodriguez, J. (2013). An Energy-conserving, Particle-dominated, Time-dependent Model of 3C 58 and Its Observability at High Energies. *ApJ*, 763(1):L4.

Torres, D. F. and Lin, T. (2018). Discovery and Characterization of Superefficiency in Pulsar Wind Nebulae. *ApJ*, 864(1):L2.

Torres, D. F., Lin, T., and Coti Zelati, F. (2019). Towards Observing Reverberating and Superefficient Pulsar Wind Nebulae. *MNRAS*, 486(1):1019.

Tziamtzis, A., Lundqvist, P., and Djupvik, A. A. (2009). The Crab Pulsar and its Pulsar-Wind Nebula in the Optical and Infrared. *A&AS*, 508(1):221.

Van der Swaluw, E., Achterberg, A., Gallant, Y. A., and Tóth, G. (2001). Pulsar Wind Nebulae in Supernova Remnants. Spherically Symmetric Hydrodynamical Simulations. *A&AS*, 380:309.

Van der Swaluw, E., Downes, T. P., and Keegan, R. (2004). An Evolutionary Model for Pulsar-Driven Supernova Remnants. A Hydrodynamical Model. *A&AS*, 420:937.

Van der Swaluw, E. and Wu, Y. (2001). Inferring Initial Spin Periods for Neutron Stars in Composite Remnants. *ApJ*, 555:L49.

Van Rensburg, C., Kruger, P. P., and Venter, C. (2014). Spectral Modelling of a H.E.S.S.-Detected Pulsar Wind Nebula. In Engelbrecht, C. and Karataglidis, S., editors, *Proceedings of SAIP2014, the 59th Annual Conference of the South African Institute of Physics (arXiv:1504.05043)*, page 377.

Van Rensburg, C., Kruger, P. P., and Venter, C. (2015). Spectral modelling of a H.E.S.S.-detected Pulsar Wind Nebula. *M.Sc. Thesis, North-West University (Unpublished)*, page arXiv:1504.05043.

Van Rensburg, C., Krüger, P. P., and Venter, C. (2018). Spatially-Dependent Modelling of Pulsar Wind Nebula G0.9+0.1. *MNRAS*, 477:3853.

Van Rensburg, C. and Venter, C. (2019). Simultaneous Fitting of the Spectral Energy Density, Energy-dependent Size, and X-ray Spectral Index vs. Radius of The Young Pulsar Wind Nebula PWN G0.9+0.1. *arXiv e-prints*, page arXiv:1905.07222.

Venter, C. and de Jager, O. C. (2007). Constraints on the Parameters of the Unseen Pulsar in the PWN G0.9+0.1 from Radio, X-Ray, and VHE Gamma-Ray Observations. In Becker, W. and Huang, H. H., editors, *WE-Heraeus Seminar on Neutron Stars and Pulsars 40 years after the Discovery*, page 40.

Vink, J. (2012). Supernova Remnants: The X-ray Perspective. *A&AR*, 20:49.

Vlahakis, N. (2004). Ideal Magnetohydrodynamic Solution to the σ Problem in Crab-like Pulsar Winds and General Asymptotic Analysis of Magnetized Outflows. *ApJ*, 600(1):324.

Völk, H. J. and Bernlöhr, K. (2009). Imaging Very High Energy Gamma-ray Telescopes. *Experimental Astronomy*, 25:173.

Vorster, M. J. and Moraal, H. (2014). The Effect of Drift on the Evolution of the Electron/Positron Spectra in an Axisymmetric Pulsar Wind Nebula. *ApJ*, 788:132.

Vorster, M. J., Tibolla, O., Ferreira, S. E. S., and Kaufmann, S. (2013). Time-dependent Modeling of Pulsar Wind Nebulae. *ApJ*, 773(2):139.

Weiland, J. L., Odegard, N., Hill, R. S., et al. (2011). Seven-year Wilkinson Microwave Anisotropy Probe (WMAP) Observations: Planets and Celestial Calibration Sources. *ApJS*, 192:19.

Weiler, K. W. and Panagia, N. (1978). Are Crab-type Supernova Remnants (Plerions) Short-lived? *A&AS*, 70:419.

Weiler, K. W. and Seielstad, G. A. (1971). Synthesis of the Polarization Properties of 3C 10 and 3C 58 at 1420 and 2880 MHz. *ApJ*, 163:455.

Weisskopf, M. C., Cohen, G. G., Kestenbaum, H. L., Long, K. S., Novick, R., and Wolff, R. S. (1976). Measurement of the X-ray polarization of the Crab nebula. 208:L125–L128.

Woosley, S. and Janka, T. (2005). The Physics of Core-Collapse Supernovae. *Nature Physics*, 1:147.

Zampieri, L. (2017). *Light Curves of Type II Supernovae*, page 737.

Zhang, L., Chen, S. B., and Fang, J. (2008). Nonthermal Radiation from Pulsar Wind Nebulae. *ApJ*, 676:1210.

Zhao, P. (2018). The Stability of Chandra Telescope Pointing and Spacial Resolution. In *American Astronomical Society Meeting Abstracts #231*, volume 231 of *American Astronomical Society Meeting Abstracts*, page 447.09.

Zheng, Y. (2011). Stochastic Acceleration of Relativistic Particles in a Turbulent Magnetic Field. *International Cosmic Ray Conference*, 8:177.

Zhu, B.-T., Zhang, L., and Fang, J. (2018). Multiband Nonthermal Radiative Properties of Pulsar Wind Nebulae. *A&AS*, 609:A110.